



Politecnico di Milano

School of Industrial and Information Engineering
Master Degree in Engineering Physics

MASTER OF SCIENCE THESIS WORK

**Lattice dynamics and phonon anomalies
in Cerium compounds**

The particular case of CeBi and CeSb

Candidate:

Edoardo Mariani

Matricola 850488

Thesis advisor:

Prof. Giacomo Claudio Ghiringhelli

Research supervisors:

Dr. Luigi Paolasini

Dr. Alexei Bosak

Academic Year 2016/2017



The whole work presented in these pages was carried out at the European Synchrotron Radiation Facility, in Grenoble, under the supervision of prof. Luigi Paolasini.

"Science is the belief in the ignorance of experts"
Richard P. Feynman

Abstract

IN this thesis a study on lattice dynamics of Cerium Bismuth and phonon anomalies of Cerium Antimony by means of Inelastic X-ray Scattering (IXS) and Thermal Diffuse Scattering (TDS) is presented. The measurements were performed in the beamline ID28 at the European Synchrotron Radiation Facility in Grenoble, France. This analysis is only a part of a bigger study of crystal properties regarding all Cerium compounds: CeP, CeAs, CeSb, CeBi, in order to understand the main differences and the features of these structures. The study of lattice dynamics allows to obtain information about the collective excitations, or phonons, in a periodic lattice. A phonon can be describe as a quasiparticle, representing an excited state of the mode of vibration of the crystal. From the phonon dispersion curves it is possible to access to various material properties, such as sound velocities, elastic constants, phonon-phonon interactions, electron-phonon interactions and dynamical instabilities. A specific feature of these compounds is their unusual magnetic properties at low temperature. In particular CeSb exhibits one of the most complex magnetic phase diagrams with more than fourteen different phases. The main typical properties are: a very small crystal electric field splitting (CEF), a very large magnetic anisotropy, unusual spectra of magnetic excitations and a large sensitivity of these properties to an applied magnetic field. This is why a lot of scientists are interested in study them. The origin if this behavior is the presence of the $4f$ level close to the Fermi energy E_f , which is a general characteristic of the anomalous rare earth systems. These anomalies arise from a periodical stacking of ferromagnetic and paramagnetic atomic planes; in the first one Ce^{3+} ions are in Γ_8 state, while in the second they are in Γ_7 state. This difference is due to the single $4f$ -electron occupation: the crystal field effect split the state $\mathbf{J} = 5/2$ into a doublet, Γ_7 , and a quartet, Γ_8 , with the Γ_7 as the ground state. But, as already said, the splitting in energy is very small, $\approx 37K$ for CeSb, and so it is easy to change the ground state configuration. Theory predict this kind of behavior with the $p - f$ mixing model: a periodic modulation of the f orbital of cerium ion, due to the interaction with a p orbital of the antimony. This effect determine a variation in energy of the states, with the Γ_8 that becomes the new ground state. So the situation is to have two different cerium atoms in different atomic planes and this cause the observed anomalies. The aim of the first part of this work is to obtain a description of lattice dynamics of CeBi

at room temperature, acquiring dispersion curves in different polarization directions. This is the first step in order to understand the properties of the compound. Using IXS it is possible to obtain direct dispersion relation measurements and, thanks to the particular setup chosen, we can select longitudinal or transverse, optical or acoustic modes. The main difference in the final data is the fact that the curves of CeBi are at low energy with respect to the same of CeSb. This because bismuth, which is just next to lead in the periodic table, is a heavier atom than antimony and also for this reason in the inelastic scan the different excitations are very close together and this is a problem for a correct fitting. As a consequence in the dispersion curves there is a bad agreement between experimental points and theoretical data.

The second part of the thesis deals with the analysis of the phonon anomalies in CeSb using TDS. This is probably the most powerful technique which give us diffuse scattering maps, that covers a big region of the reciprocal space. Unfortunately, due to some problems in the technical instrumentation, we were forced to move to an IXS acquisition in order to have better resolution. The experimental results shows clearly a presence of satellite peaks at 14 K associated to the charge modulation. But, it is possible to observe something new, that no one find in the past: there is a systematic cancellation of the third order satellite only in particular \mathbf{Q} positions, and another small satellite that appear just next to the first one. Starting from this we also develop a model, based on the fact that there are three different magnetic interaction from different magnetic planes that causes three different static displacements which affect the trigonometric structure factor, and the predicted result agree with the experiment.

Sommario

L lavoro presentato in questa tesi riguarda lo studio della dinamica reticolare del Cerio Bismuto e di anomalie strutturali nel Cerio Antimonio utilizzando due tecniche sperimentali: l'Inelastic X-ray Scattering (IXS) e il Thermal Diffuse Scattering (TDS). Tutta l'attività si è svolta nella beamline ID28 presso l'European Synchrotron Radiation Facility a Grenoble, Francia. Questa analisi è stata solo una piccola parte di un lavoro molto più lungo e complicato, ovvero quello di studiare le proprietà cristallografiche dei composti binari che il cerio forma con gli elementi del V gruppo: CeP, CeAs, CeSb, CeBi, in modo da conoscere, comprendere e confrontare le principali proprietà di questi composti.

Lo studio della dinamica reticolare è molto importante perché permette di ottenere informazioni sulle eccitazioni collettive della struttura periodica, cioè sui fononi. Un fonone può essere descritto quantisticamente come una quasi particella che rappresenta uno stato eccitato di un modo di vibrazione del cristallo. Il principale risultato ottenibile da un esperimento di Inelastic X-ray Scattering è l'acquisizione delle curve di dispersione del campione in esame. Da esse è possibile determinare diverse proprietà del materiale come le velocità del suono, costanti elastiche, interazioni fonone-fonone, elettrone-fonone e instabilità dinamiche.

Una caratteristica che contraddistingue questi composti sono sicuramente le loro particolari proprietà magnetiche a bassa temperatura. Il cerio antimonio, soprattutto, è caratterizzato da uno dei più complessi diagrammi di fase magnetica osservabili in composti binari, con più di quattordici fasi diverse. Altre proprietà caratteristiche sono: una separazione dei livelli degeneri dovuta all'effetto del campo cristallino molto piccola, una forte anisotropia magnetica, un particolare spettro delle eccitazioni magnetiche e una dipendenza di tutte queste proprietà al campo magnetico applicato. L'origine di questo comportamento è dovuta alla presenza del livello $4f$ molto vicino al livello di energia di Fermi, E_f , caratteristica generale di tutti i composti di terre rare che presentano anomalie. Queste sono le motivazioni che hanno spinto numerosi scienziati nello studio di questi composti. Esistono diverse teorie per descrivere queste anomalie ma tutte sono in accordo con il fatto che queste siano causate da una periodica ripetizione di piani atomici ferromagnetici e paramagnetici; nei primi gli ioni di Ce^{3+} si trovano nello stato Γ_8 , mentre nei secondi in uno stato Γ_7 . La differenza tra i due è determinata dall'occupazione che ha il singolo elettrone $4f$: a causa del campo cristallino

lo stato degenerare $J = 5/2$ si divide in una coppia Γ_7 e in un quartetto Γ_8 , con lo stato Γ_7 come livello fondamentale. Ma, come già detto, lo splitting in energia è molto piccolo, circa 37K nel CeSb, quindi è molto facile invertire i due stati modificando quello fondamentale. E' bene specificare che un atomo di cerio in stato Γ_8 è caratterizzato da un elevato valore di momento magnetico, circa $2 \mu_B$, mentre un cerio in stato Γ_7 è uno ione pressoché paramagnetico. Il modello $p - f$ mixing permette di spiegare il motivo di queste modulazioni ammettendo che l'orbitale f possa interagire con l'orbitale p dell'antimonio causando una modulazione periodica della densità di carica. Questo determina una variazione nell'energia degli stati con il Γ_8 che diventa il nuovo stato fondamentale.

Lo scopo principale della prima parte del lavoro è quello di determinare le proprietà reticolari del CeBi a temperatura ambiente, acquisendo curve di dispersione nelle varie direzioni di polarizzazione. Questo può essere un primo passo per caratterizzare il composto. Utilizzando l'IXS è possibile ottenere misure dirette a precisi valori di momento Q e, grazie ad opportuni setup sperimentali siamo in grado di analizzare separatamente modi longitudinali e trasversali, ottici e acustici. Uno sguardo ai risultati ottenuti permette di evidenziare alcune differenze sostanziali tra i due composti: in generale le curve del CeBi sono ad energie più basse rispetto alle stesse del CeSb. Ciò è dovuto principalmente al fatto che l'atomo di bismuto, che sulla tavola periodica si trova proprio accanto al piombo, è nettamente più pesante di quello di antimonio. Questo fatto rende anche gli scan acquisiti molto più difficili da analizzare perché i picchi presenti risultano molto più vicini, ed è quindi anche una spiegazione del perché complessivamente l'accordo tra i dati sperimentali e quelli teorici per il CeBi risulta essere peggiore.

La seconda parte invece è dedicata allo studio delle anomalie nel CeSb utilizzando il TDS. Questa tecnica probabilmente è la migliore per questo tipo di analisi perché è in grado di fornire mappe di scattering che coprono una regione molto ampia dello spazio reciproco. Sfortunatamente, a causa di problemi alla strumentazione che andavano a limitare la regione accessibile dello spazio reciproco, nelle immagini ottenute non vi è nessuna traccia di anomalie e per questo è stato necessario eseguire un nuovo esperimento utilizzando la tecnica IXS. I risultati ottenuti mostrano chiaramente la presenza di picchi a 14 K associati a una modulazione di carica. Ma, oltre a questi picchi principali, già trattati in altre pubblicazioni, è stata osservata una simultanea cancellazione del picco corrispondente alla terza armonica solo in particolari posizioni dello spazio reciproco, e un nuovo satellite è comparso molto vicino al picco associato alla prima armonica. Infine, partendo da queste osservazioni è stato pensato e proposto un modello basato su 3 differenti magnetostrizioni tra i vari piani magnetici che causano una variazione della distanza di legame. Ciò determina una modifica del fattore di struttura e quindi una possibile spiegazione dell'assenza di alcuni picchi.

Contents

Abstract	II
Sommario	IV
List of Figures	VIII
List of Tables	IX
1 Experimental Facility	1
1.1 Synchrotron Facilities	1
1.2 ESRF Synchrotron	2
1.3 Beamline ID28	5
1.3.1 High Resolution Monochromator (HRM)	7
1.3.2 Spherical Analyzers	8
1.3.3 Side Station Setup	9
2 Experimental Techniques	11
2.1 Introduction to X-ray scattering	11
2.2 The Debye-Waller factor and Thermal Diffuse Scattering (TDS)	12
2.2.1 Properties of Debye-Waller factor	14
2.3 Inelastic X-ray scattering (IXS)	15
2.3.1 The Scattering cross-section	18
3 Cerium Antimony and Cerium Bismuth	21
3.1 Crystallographic properties	21
3.2 Electronic properties	25
3.3 CeSb magnetic phase diagram	26
3.4 CeBi magnetic phase diagram	28

Contents

4	Phonon measurement on Cerium Bismuth	31
4.1	IXS setup	31
4.2	Dispersion curves of CeBi	32
4.3	The Force-Constant Matrix	39
4.4	Born - von Karman theory	41
4.4.1	Equations of motion	41
4.5	Lattice vibrations of solids with <i>fcc</i> crystal structure	43
4.5.1	Application on the CeSb and CeBi case	46
4.6	The <i>ab-initio</i> approach to phonons	47
5	Phonon anomalies in Cerium Antimony	51
5.1	Diffuse Scattering Experiment	51
5.2	IXS Experiment	53
5.3	A proposed model for the observed anomalies	58
6	Conclusions	63
A	Elastic waves in Cubic crystals	65
A.1	Wave in the [100] Direction	66
A.2	Wave in the [110] Direction	66
	Acknowledgements	69
	Bibliography	71

List of Figures

1.1	Plot of the brilliance evolution in the last century and in the future years. It is possible to distinguish the first, second and third generation of synchrotron	2
1.2	Schematic 3D representation of the European Synchrotron Radiation Facility.	3
1.3	Representation of a section of the storage ring. It is possible to see the Bending Magnet and the undulators.	4
1.4	Bending Magnet, up, and Insertion Device, down, at the ESRF.	5
1.5	Schematic layout of beamline ID28 at ESRF.	6
1.6	Photograph of the Main station setup. It is clearly visible the 7 m spectrometer arm where the analyzers are mounted.	7
1.7	Photograph of one of the nine analyzers used in the IXS spectrometer.	8
1.8	Schematic layout of the side station at ID28.	9
1.9	Diffraction geometry for a diffuse scattering experiment.	10
2.1	Representation of the elementary excitations studied with the inelastic X-ray scattering technique.	12
3.1	Graphical representation of the NaCl-like crystal structure of the CeX compounds.	22
3.2	Section of the reciprocal lattice in the plane defined by directions $\langle 100 \rangle$ and $\langle 011 \rangle$	25
3.3	Schematic representation of the p-f mixing described by Kasuya's group. First there is a splitting due to the crystal field interaction in octahedral symmetry, than the hybridization between p hole orbitals and 4f electron cause a shift in energy.	26
3.4	Magnetic phase diagram of CeSb. Picture taken from ref. [18]	27
3.5	Specific heat of CeSb in different temperatures at zero applied field. Picture taken from ref. [14]	28
3.6	Magnetic phase diagram of CeSb at low temperature with no magnetic field and a schematic representation of magnetic structures. Picture taken from ref. [41]	28

List of Figures

3.7	Magnetic phase diagram of Cerium Bismuth. Picture taken from ref. [14]	29
4.1	Photograph of the sample mounted on the goniometer head in the final geometry.	33
4.2	Representation of the scattering plane in the IXS experiment. Green, red and blue lines are associated to three different polarization directions, in this case for an acoustic mode	34
4.3	Representation of the second crystal orientation. Colored lined are associated to the paths followed in the reciprocal space	34
4.4	First Brillouin zone for the <i>fcc</i> lattice	35
4.5	Examples of scans acquired for the $\langle 100 \rangle$ direction. In particular it's possible to observe the longitudinal and transverse acoustic phonons for different fixed \mathbf{Q} .	36
4.6	Up: <i>ab</i> initio results of phonon dispersion curves of CeSb. Different modes are labelled with different types of lines. Dots, filled and empty, are the experimental data. Down: <i>ab</i> initio calculations for CeBi also together with the experimental points.	37
4.7	<i>fcc</i> structure	44
4.8	Rock-salt structure	46
5.1	Diffuse Scattering acquisition at different temperature: A) 12K B) 13K	52
5.2	Diffuse Scattering acquisition at different temperature: C) 14.5K D) 16K	53
5.3	Setup for the low temperature measurement of CeSb. The displax is mounted on the adth arm of the spectrometer.	54
5.4	Scan of the satellite peaks observed along the $(4+H, 0, 0)$ direction at 14 K.	55
5.5	HKL scan along the (100) direction from $(3, 0, 0)$ up to $(7.15, 0, 0)$. It is clearly visible the systematic cancellation of the third order satellite.	56
5.6	Schematic representation and definitions of interlayer distances in the model. Open and filled circles represent Ce-ion layers of the Γ_7 state and those of the Γ_8 -like state, respectively. Picture taken from ref. [41]	57
5.7	Inelastic scan at 14 K. It is clearly visible a peak at $\approx 4meV$ corresponding to a new phonon mode	58
5.8	Representation of the average position of the 7 different atomic planes in the $\frac{4}{7}$ phase of the CeSb	59
5.9	Another representation of the $\frac{4}{7}$ phase of CeSb that explains the symmetry properties of the magnetic structure	59
A.1	Effective elastic constants for the three modes of elastic waves in the principal propagation directions in cubic crystals. The two transverse modes are degenerate for propagations in the $[100]$ and $[111]$ directions.	67

List of Tables

3.1	Table with important parameters of cerium compounds: lattice constant at room temperature, Néel temperature, crystal field splitting and total magnetic moment.	22
4.1	Table with the value of the elastic constants of CeBi evaluated from the simulations and from the calculations.	38
4.2	Table with the value of the elastic constants of CeSb evaluated from the simulations and from the calculations.	39
4.3	General force-constant matrices for the twelve nearest neighbours in the f.c.c. structure	44
4.4	General force-constant matrices for the six nearest-neighbours in the rock-salt structure	47
5.1	Table with the predicted and observed values of the Bragg and satellite peaks in CeSb	61

CHAPTER 1

Experimental Facility

The first part of this work is dedicated to a briefly but necessary introduction to the physical principles behind the generation of synchrotron radiation, focusing on the European Synchrotron Radiation Facility (ESRF). In the beginning there is a general analysis of the main synchrotron in the world and a description of how the radiation is produced at the ESRF. Then there is a presentation of the ID28, the inelastic X-ray scattering beam line where all these experiments were carried out.

1.1 Synchrotron Facilities

The history of the synchrotrons starts in 1947 at General Electric where a research group in New York discovered the synchrotron radiation. This is the name given to the radiation that is generated by charged particles travelling at relativistic speed when they are forced to curve their trajectory, using a magnetic field, see [1] for more details. Just after this discovery, all the scientific community understood that this electromagnetic radiation is a very powerful instrument in order to analyze the matter. The first generation of synchrotron was built starting from the 50's, and in 1956 the first experiment was carried out by Tomboulion and Hartman in Cornell University (Ithaca, United States). An important feature of these first generation of facilities is that they are 'parasitic' structure, because the accelerators were built not for x-ray generation, but operated primarily for high-energy or nuclear physics.

The trend starts to change after the construction of DESY synchrotron in Hamburg (Germany) in 1968, and Synchrotron Radiation Source (SRS) at the Daresbury Laboratory (United Kingdom). This opens the way for the second generation sources like NSLS (Upton, United States), KEK (Tsukuba, Japan), BESSY (Berlin, Germany) and LURE (Paris, France) which are the most famous. These facilities have the characteristic to be a stand alone structure with a stor-

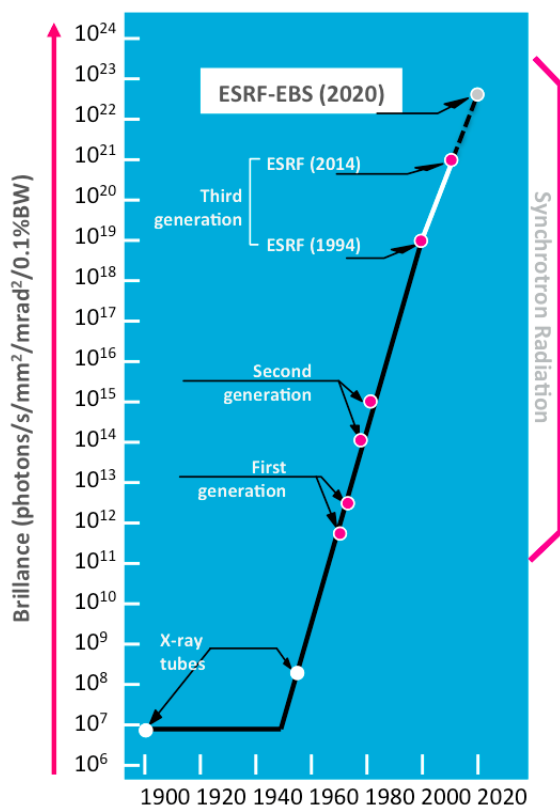


Figure 1.1: Plot of the brilliance evolution in the last century and in the future years. It is possible to distinguish the first, second and third generation of synchrotron

age ring, that is mandatory for high-energy measurement.

The evolution culminated with the third generation of synchrotron. The ESRF, first operate in 1994, is one of the most important of this generation, together with the APS (Argonne, United States) and Spring-8 (Hyogo prefecture, Japan). The main features of this last generation are the very big dimension of the storage ring (850 to 1440 meters of circumferences) and many order of magnitude higher in brilliance and coherence with respect to the early lab sources.

1.2 ESRF Synchrotron

Let's focus now on the ESRF synchrotron and explain how it works and how radiation is produced. The electrons are produced by an electron gun and immediately accelerated by a DC electric field up to 90 keV then up to 140 MeV by the linear accelerator (LINAC). The second stage is their injection in the 300 m long booster ring, where they are finally accelerated to reach the energy of 6 GeV. In the final stage, the electrons are now ready to produce light and they enter in the storage ring, a 884 m-long circular tube, and they circulate at a frequency of 355 kHz. Figure 1.2 shows a 3D representation of the structure. Electrons, as known, interact a lot with the particles in the atmosphere so, to allow them to circulate, the ring is maintain in ultra high vacuum (UHV) level, up to 10^{-11} mbar. In this way their

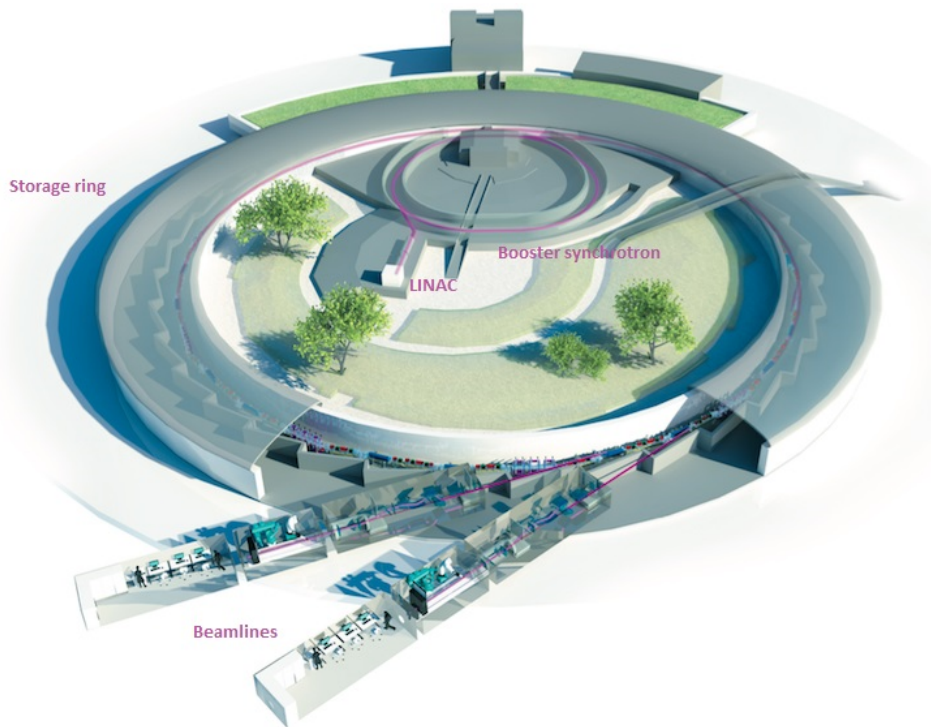


Figure 1.2: Schematic 3D representation of the European Synchrotron Radiation Facility.

lifetime is about 60 h during which they can emit radiation. Inside the storage ring, electrons must keep their energy, this is done by conductive metal structures (cavities) which reshape the modes of oscillation of the electromagnetic field in order to have a component parallel to the electrons motion. The oscillation frequency of these cavities is controlled by a radio frequency system (RF) that is set to 3 GHz (35 MW power) for the booster ring and at 352 MHz (9 MW power) for the storage ring. The RF control also determines the *filling mode* of the ring. In fact the storage ring is never completely filled, electrons are grouped in packages, the *bunches*, which may contain a different number of them depending on the filling mode. Obviously, the maximum number of bunches in the ring is equal to the length of the ring divided by the RF frequency. In the other modes of operation less bunches are present, but each bunch has high current, resulting in an increased power of each bunch.

The electrons, moving inside the ring, provide the radiation to the beamlines when they are forced to curve their trajectory. There are two types of electromagnetic radiation sources in the synchrotron: *bending magnets* (BMs) and *insertion devices* (IDs). Bending magnets are placed in particular positions in the storage ring, where the path of the electrons must be deflected. Electrons pass through the magnet and they emit x-rays tangentially to the plane of the beam. The final radiation produced by the BMs covered a wide and continuous spectrum. The IDs, on the other hand, are placed in the straight section between BMs. These magnetic structures, made up of a complex array of small magnets, force the electrons to follow an undulating, or wavy, trajectory. The radiation emitted at each consecutive band overlaps and interferes with that from the other bands. This generates a much more focused, or brilliant, beam of radiation with respect to the one produced by a single magnet. Also, the photons

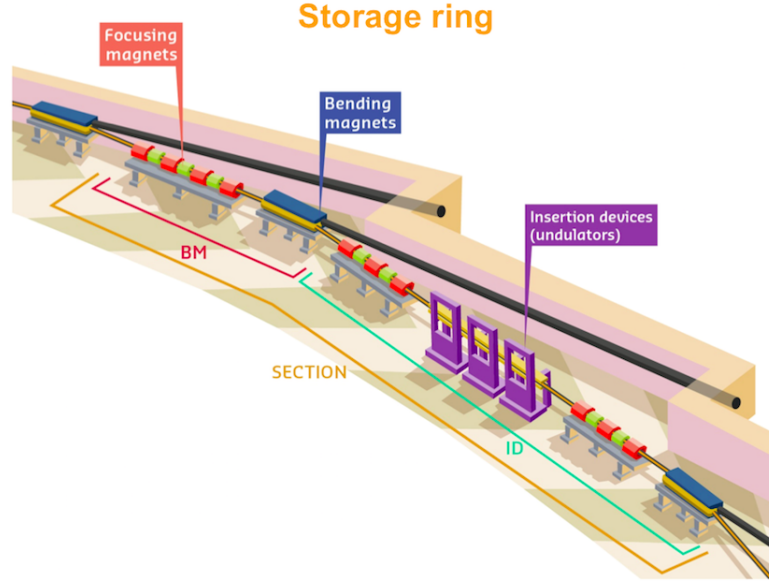


Figure 1.3: Representation of a section of the storage ring. It is possible to see the Bending Magnet and the undulators.

emitted are concentrated at certain energies (called fundamental and harmonics). The gap between the rows of magnets can be changed to fine-tune the wavelength of the X-ray in the beam. An important parameter useful to describe the electron motion inside an ID is the deflection parameter K , which is given by:

$$K = \frac{eB_0\lambda_u}{2\pi mc} = 0.0934\lambda_u[cm]B_0[T] \quad (1.1)$$

It's possible to have two types of ID depending on the K parameter: If K is $\gg 20$ we have a *wiggler*, if $K \ll 1$ we have an *undulator*. For an undulator we have that a given electron at one oscillation is in phase with the radiation of the following oscillations because the angular deflection lies within the nominal $1/\lambda$ emitted radiation cone of the SR. The final radiation is expressed in the so-called undulator equation:

$$\lambda[nm] = \frac{1.306\lambda_u[cm](1 + \frac{K^2}{2} + \gamma^2\theta^2)}{E_e^2[GeV]} \quad (1.2)$$

where E_e is the energy of the electron and $\gamma^2\theta^2$ are the off-axis wavelength variations. In addition to the fundamental, the effect of the transverse oscillations introduces higher harmonics in the total radiation. The even harmonics radiate off-axis, and they have less intensity than in-axis odd harmonics. It is important to note that K parameter appears in Equation 1.2, which means that the fundamental wavelength can be shifted varying the magnetic field of the undulator. In the end, to summarize, the important characteristics of the undulator are:

- The high flux of x-rays coming out, due to the phase oscillation, resulting in high brilliance.
- Intrinsic angular divergence of the x-ray beam, smaller compared to the BMs.

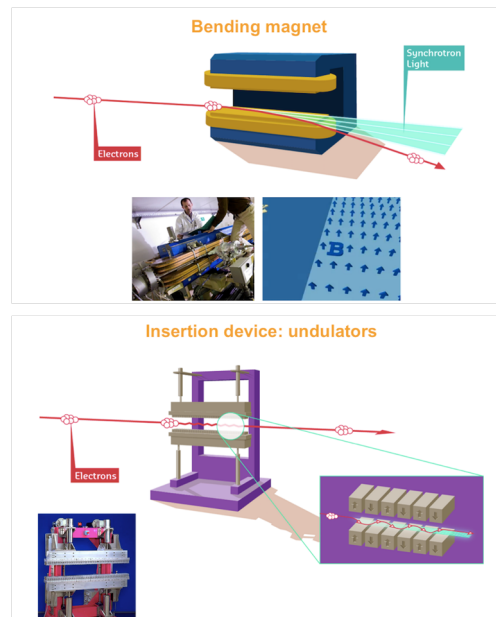


Figure 1.4: *Bending Magnet, up, and Insertion Device, down, at the ESRF.*

- A fully tunable source of x-rays over an extended spectral range, included all the odd harmonics.
- Linear polarization of the radiation.

1.3 Beamline ID28

ID28 is a beamline where the inelastic x-ray scattering and diffuse scattering techniques are used in combination, it is dedicated to the study of phonon dispersion in condensed matter at total momentum transfer, \mathbf{Q} , and energy transfer, E , characteristic of collective atoms motions. It operates in the hard X-ray regime and choosing the proper geometry of the monochromator is possible to obtain six different incident energies of 13.840, 15.817, 17.794, 21.747, 23.725 and 25.704 keV, which corresponds to a Si (nnn) reflections ($n= 7, 8, 9, 11, 12, 13$).

In general, the physics information that can be obtained in ID28 can be divided in three different categories:

1. determination of phonon dispersion in crystalline materials;
2. study of high frequencies collective dynamics in disordered systems (quantum liquids, glass formers);
3. determination of dispersion relations under extreme conditions: pressure up to 100 GPa and temperature range from 2 to 1000 K can be achieved.

Thanks to phonon dispersion it is possible to access various material properties, like elastic constants, phonon-phonon interaction, electron-phonon coupling and dynamical properties

Chapter 1. Experimental Facility

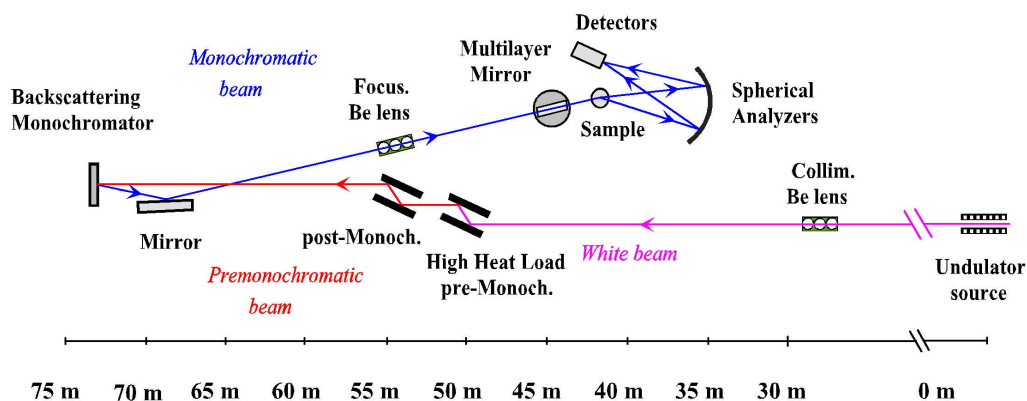


Figure 1.5: Schematic layout of beamline ID28 at ESRF.

of the lattice.

The instrumentation of ID28 is based on two stations: the Main station, for IXS measurements, and the new Side station, with a instrumentation for Diffuse Scattering analysis. The Main station is based on a three-axis spectrometer, previously developed for inelastic neutron scattering and then modify for this type of analysis[2][3]. In the first axis the energy of the incident X-rays from the undulators is selected. Then the monochromatic beam hit the sample, whose position, orientation and scattering angle are selected, this is the second axis. After choosing the scattering angle, the third axis is the crystal analyzer, which specifies the scattered photon energy to be detected.

This is only a brief introduction of the real path that the beam has to follow after it is emitted by the undulator. In the first step, before reaching the main monochromator, X-rays, coming from the ring with a bandwidth of $\frac{\Delta E}{E} = 10^{-2}$ and an integrated power of $\approx 200W$, pass through a pre and post-monochromator stage that improve the resolution up to $\frac{\Delta E}{E} = 10^{-5}$ almost. They consist of a Si(111) and Si(400) reflection from a single crystal, kept in vacuum. The goal of this stage is not only to increase the resolution but also to reduce the heat load on the main monochromator, that can damage the silicon single crystal. The beam reach so the main monochromator, it operates in backscattering geometry at the Bragg angle of 89.98° . It is composed by a silicon crystal, and here it is possible to select the (nnn) reflection, as previously described. After this the energy resolution is $\frac{\Delta E}{E} = 10^{-8}$, which is enough for the high precise measurement requested.

The resolution needed now is achieved, so after the backscattering monochromator we have the focusing stage of the beam. Both horizontal and vertical focusing can be obtained using the platinum coated toroidal mirror, placed just after the monochromator, at 25m from the sample position. This configuration allows to obtain a beam size of $270 \times 70 \mu m^2$ in the horizontal and vertical direction. If it is necessary to obtain a small spot size on the sample, the cylindrical mirror configuration is used for the vertical focusing together with a multilayer mirror at in order to obtain a spot size of $14 \times 60 \mu m^2$.

After hitting the sample, the photons are scattered and collected by an array of nine spherical analyzers, which are located at the end of the 7 m spectrometer arm. This setup is useful in



Figure 1.6: Photograph of the Main station setup. It is clearly visible the 7 m spectrometer arm where the analyzers are mounted.

order to speed up and parallelize the data collection. In particular there is a linear array in the horizontal scattering plane, very useful for *disordered materials* because each analyzer adds either a new momentum transfer (for those in the scattering plane) or additional data at a nearly equivalent momentum transfers (for those out of plane). Each crystal Bragg-reflect the radiation into one of the nine detector, with an active area of $3 \times 8 \text{ mm}^2$, the detectors have a very low dark noise level of 1 count in 30 minutes. In order to collect the radiation in a correct way, the analyzer crystals have a spherical surface whose radius is equal to the sample-analyzer distance. This is known as Rowland condition, and guarantee the best focusing action for this kind of setup.

1.3.1 High Resolution Monochromator (HRM)

As already said, the scattering geometry defines the momentum and energy transfer from the scattering process. In order to perform an IXS experiment, the only possibility to obtain an energy scan with a backscattering monochromator is to change the Si crystal plane spacing, d , using thermal expansion, see Graeff and Materlik [4]. The relation between the energy and lattice parameter is $\frac{\Delta E}{E} = \frac{\Delta d}{d} = \alpha \Delta T$, with $\alpha = 2.6 \times 10^{-6} \text{ K}^{-1}$ the thermal expansion coefficient of silicon at room temperature. Thus, with $\sim \text{mK}$ stability and few degree of scan ranges, one can effectively scan the interesting region of energy transfer for the backscattered monochromator. Another issue regards the geometry of the monochromator. In fact, the re-

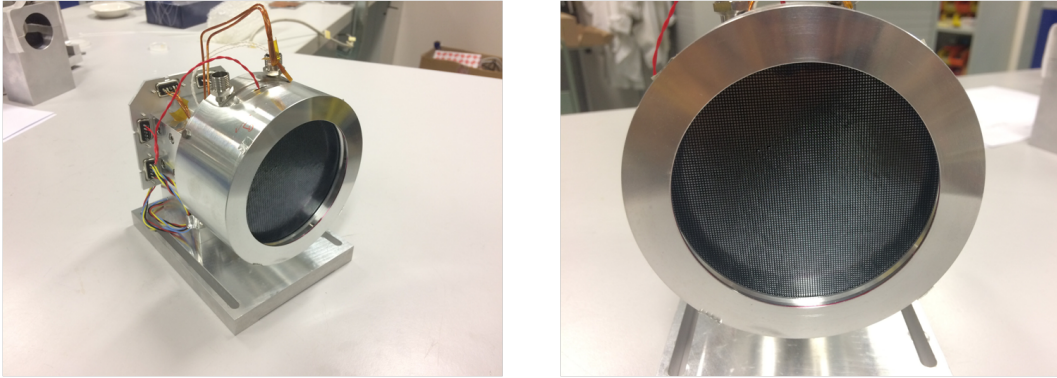


Figure 1.7: Photograph of one of the nine analyzers used in the IXS spectrometer.

flected beam lies nearly on top of the incident beam. This means that additional optics must be used to separate the two beams to allow enough space at the sample position. This is done in ID28 by the using focusing mirror and long travel distance.

There are other few important practical details about the backscattering setup: a backscattering monochromator must be thermally isolated on top of stages that allow one to carefully control the angle and temperature. Some cares in design is needed both to allow reliable temperature control and to minimize the angular drift of the crystal when the temperature is changed.

1.3.2 Spherical Analyzers

The analyzers are the heart of the IXS beamline and the most difficult optic to fabricate. The goal of the analyzer is essentially the same as the high resolution monochromator: select a very narrow bandwidth of radiation, but, on the contrary, the analyzer see an highly divergent beam from the sample, [5][6]. In general, one of this two options can be considered for the shape of the analyzer: either a figured analyzer where the shape is chosen so that the Bragg angle does not vary significantly over the desired angular acceptance, or one can collimate the divergent beam from the sample. In ID28 the first option is chosen: bending a crystal introduces strain so that is not an option, and the universal solution has been to bond many crystallites to a curved substrate. In our particular case each analyzer consist of a spherical substrate on which approximately 12000 perfect silicon crystals ($0.6 \times 0.6 \text{ mm}^2$ surface and 3 mm thick) are attached.

Consideration on Bragg's law leads to define a geometric contribution for the analyzer resolution that scales as

$$\left(\frac{\Delta E}{E}\right) = \frac{cd}{2R^2} \quad (1.3)$$

where $d/2R$ is the deviation from the exact backscattering and c/R is the divergence accepted by a single crystal. Thus, from the point of view of minimizing this contribution to the energy resolution it is clearly desirable to have R large, and the transverse crystallite size c and the detector offset d , both small. The R^2 dependence of this term strongly favors large arm radii, however the practical issues of space in the experimental floor, as well as expense, tend to push for smaller radii, with the operating spectrometer having arm radii varying from $R = 6$

Side Station Diffractometer

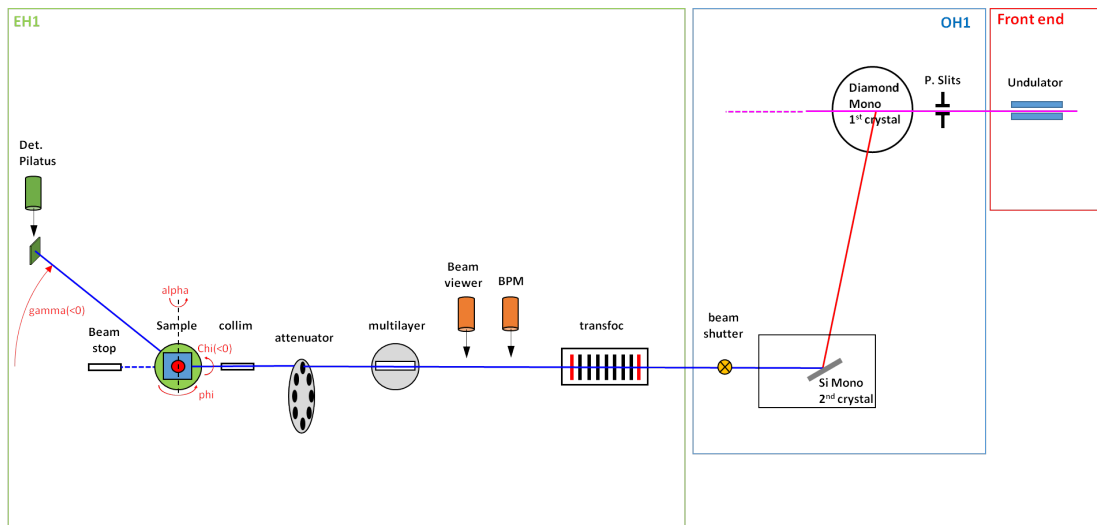


Figure 1.8: Schematic layout of the side station at ID28.

to 10 m, pixel size of $c \sim 1$ mm and detector offsets, $d \sim$ few mm.

1.3.3 Side Station Setup

The experimental geometry of a diffuse scattering experiment is identical to x-ray diffraction. Monochromatic X-rays are scattered from the sample, in general in transmission geometry, and the scattered intensity distribution is recorded by an area detector. One of the main problems is the fact that here the signal is very weak, so it is necessary to have a reduction of the background intensity and read-out noise of the detector. Also air scattering is a problem, but this can be minimized by using a collimator in front of the sample and a beamstop behind it, which also protect the area detector from the direct beam. As it is possible to see from Figure 1.8 the beam that coming from the undulator is first splitted by a diamond single crystal in the optics hutch: 10% of the beam is deviated and is available for the Side station, 90% is dedicated to the main station. After this first split there is another reflection on a silicon single crystal in order to reach the desired resolution, than all the elements of the focusing stage are present. The sample is mounted on a goniometer and the direct beam is blocked by a beamstop. The intensity is collected by a pixel detector with practically no dark noise.

The choice of a suitable detector is essential for the analysis of the TDS intensity distribution. Silicon pixel detector systems are now the best option available for TDS studies below 20 keV. In this station a PILATUS detector, [7], is mounted. Such detectors can be operated in single photon counting mode, each pixel is read out individually. They possess no dark current and no read-out noise and the energy resolution for this type of detector is 500 eV.

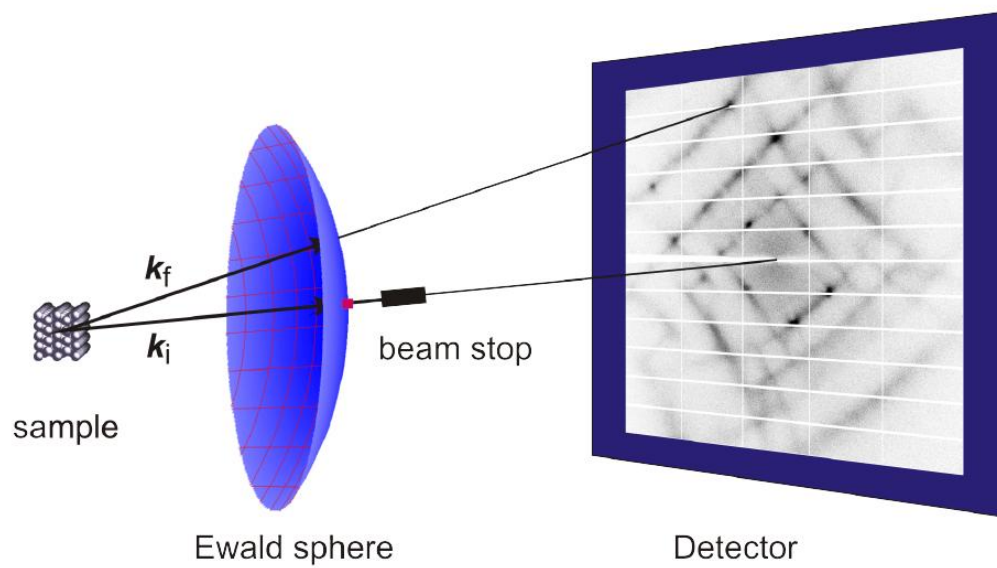


Figure 1.9: *Diffraction geometry for a diffuse scattering experiment.*

CHAPTER 2

Experimental Techniques

In this section a theoretical introduction on the techniques that uses X-rays scattering is presented. First there is an introduction on the basic concepts of the scattering and the scattering theory, then the discussion moves to a real situation: scattering from a crystal sample where atoms are not frozen at the lattice sites, but they perform vibrations. The result is the presence of a diffuse component which is superimposed to the Bragg scattering. The the second part of the chapter is focused on the IXS scattered intensity: using the expression obtained from the Born-von Karman theory, it is possible to arrive to a separation of the different contributions. At the end a description of the scattering cross-section is presented.

2.1 Introduction to X-ray scattering

Inelastic X-ray Scattering is a X-ray spectroscopy technique, in which photons are scattered by the matter. It is a photon-in photon-out process and one of the most important aspects is the possibility of changing the energy range of the interaction in order to study different excitations. Starting from the low energy excitations, like phonons and magnons (10-100 meV), then the electron excitation and plasmons (1-10 eV), up to the core electron excitation ($\simeq 1$ keV). In this thesis, as already said, we want to study phonons properties of the compounds, so we are interested in energy exchange in the order of meV. The initial energy of the beam, after the Si (9 9 9) reflection, is 17.793 keV, the resulting relative energy resolution needed is $\frac{\Delta E}{E} = 10^{-8}$. This is one of the main reason that makes these experiments so challenging, and require a synchrotron radiation and not a conventional X-ray tube.

Before the creation of the synchrotron facilities, in the 1990's, the only way to perform these type of experiments was with the Inelastic Neutron Scattering (INS) in nuclear reactors. Neutrons are quite good for lattice dynamics studies, but they also have some limitations that

Chapter 2. Experimental Techniques

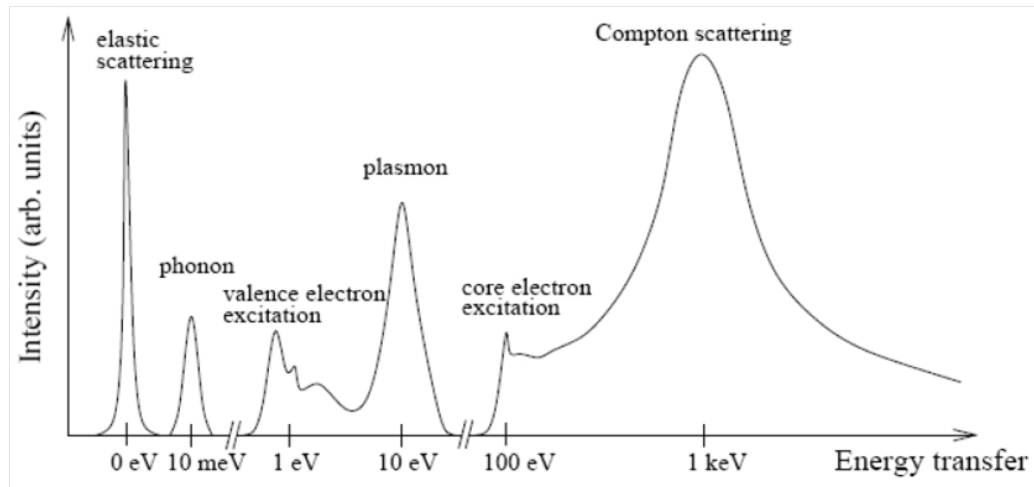


Figure 2.1: Representation of the elementary excitations studied with the inelastic X-ray scattering technique.

makes X-ray a better probe:

- X-rays have a large incoherent cross-section with respect to neutrons;
- X-rays experiments can be performed on samples of very small size. INS experiments in fact typically require sample's volumes of several mm^3 , while IXS measurements can be successful on samples of very small size, until 10^{-5}mm^3 . This consenting to study materials only available in very small quantities, or very dangerous (like radioactive materials).

In order to study this scattering process there are two main assumptions:

1. In the Thompson scattering the electrons are considered at rest and they don't interact with anything when they interact with X-rays,
2. The diffraction volume is assume to be small and the scattering weak, the sample induces a small perturbation in the incoming beam.

This situation is also known as the *kinematical approximation*, which is in contrast with the *dynamical scattering theory*. In the kinematic diffraction the incident wave is reflected only one time by a given plane, neglecting the multiple diffraction of the same wave due to different planes. This approximation is not valid in the case of perfect crystals, where the dynamical scattering theory takes into account the multiple scattering effect, and corrects for refraction, shape and width of the peaks, extinction and interference effects.

2.2 The Debye-Weller factor and Thermal Diffuse Scattering (TDS)

In the derivation of the Von Laue law, for the Bragg scattering, the lattices considered have all one fundamental feature: they are assumed to be perfectly rigid. In reality atoms are not frozen in fixed positions, they vibrate around equilibrium positions. Here a discussion

2.2. The Debye-Weller factor and Thermal Diffuse Scattering (TDS)

about the effect of these vibrations on the scattered intensity is presented, using the formalism proposed by Als-Nielsen & McMorrow (2011) [8] and Willis & Pryor (1975) [9]. Let's take into account the fact that the vibrations are due to two distinct causes: the first is purely quantum mechanical in origin and arise from the uncertainty principle: they are temperature independent and occur even at zero of temperature. The other one are finite temperature displacements fo atoms which are thermally excited in the crystal, increasing the amplitude of vibrations.

To determine the intensity of X-rays scattered by the crystal we have to assume that the electrons follow instantaneously the displacement of the nuclei, this is the well known '*adiabatic approximation*'. So, in this approximation, the scattering is given by taking the total electron distribution as the superposition of the distribution of the individual atoms. If the electron distribution of each atom is the same as for the isolated atom, the scattered intensity is the average value of the amplitude of scattering multiplied by its complex conjugate

$$\mathbf{I}(\mathbf{Q}) = \langle \mathbf{F}(\mathbf{Q})\mathbf{F}^*(\mathbf{Q}) \rangle \quad (2.1)$$

where

$$\mathbf{F} = \sum_n f(\mathbf{Q})e^{i\mathbf{Q}\cdot\mathbf{R}_n}$$

is the structure factor for a simple crystal structure in which there is one atom located in each lattice point. The effect of vibrations is take into account by writing the instantaneous position of an atom as $\mathbf{R}_n + \mathbf{u}_n$ where \mathbf{R}_n is the time averaged mean position and \mathbf{u}_n is the displacement. Of course, by definition, $\langle \mathbf{u}_n \rangle = 0$.

The intensity becomes

$$\mathbf{I}(\mathbf{Q}) = \sum_m \sum_n f(\mathbf{Q})f^*(\mathbf{Q})e^{i\mathbf{Q}\cdot(\mathbf{R}_m - \mathbf{R}_n)} \langle e^{i\mathbf{Q}\cdot(\mathbf{u}_m - \mathbf{u}_n)} \rangle \quad (2.2)$$

This expression can be further simplified using the *Baker-Hausdorff* theorem, which states that if x is described by a Gaussian distribution then

$$\langle e^{ix} \rangle = e^{-\frac{1}{2}\langle x^2 \rangle}$$

So the temporal average becomes

$$\langle e^{i\mathbf{Q}\cdot(\mathbf{u}_{Qm} - \mathbf{u}_{Qn})} \rangle = e^{-\frac{1}{2}Q^2\langle u_{Qm}^2 \rangle} e^{-\frac{1}{2}Q^2\langle u_{Qn}^2 \rangle} e^{Q^2\langle u_{Qm}u_{Qn} \rangle}$$

where u_{Qn} is the component of the displacement in the direction of the wave vector transfer \mathbf{Q} for the n^{th} atom. Due to translational symmetry $\langle u_{Qm}^2 \rangle = \langle u_{Qn}^2 \rangle$ and it is possible to write the term as e^{-M} . The last term in the above expression for the temporal average is

$$e^{Q^2\langle u_{Qm}u_{Qn} \rangle} = 1 + \{e^{Q^2\langle u_{Qm}u_{Qn} \rangle} - 1\}$$

We obtain the final expression for the scattered intensity which is separated in two terms:

$$\begin{aligned} \mathbf{I}(\mathbf{Q}) &= \sum_m \sum_n f(\mathbf{Q})e^{-M} e^{i\mathbf{Q}\cdot\mathbf{R}_m} f^*(\mathbf{Q})e^{-M} e^{-i\mathbf{Q}\cdot\mathbf{R}_n} \\ &+ \sum_m \sum_n f(\mathbf{Q})e^{-M} e^{i\mathbf{Q}\cdot\mathbf{R}_m} f^*(\mathbf{Q})e^{-M} e^{-i\mathbf{Q}\cdot\mathbf{R}_n} \{e^{Q^2\langle u_{Qm}u_{Qn} \rangle} - 1\} \end{aligned} \quad (2.3)$$

Chapter 2. Experimental Techniques

The first term is the usual elastic scattering from a lattice except that the atomic form factor is replaced by

$$f^{atom} = f(\mathbf{Q})e^{-M}$$

where the exponential term is known as the *Debye-Waller factor*. This shows that the elastic Bragg scattering is reduced in intensity by atomic vibrations, but its width is not increased. The second term, instead, has a different character: it has an intensity that actually increases as the mean-squared value displacement increase, and a width which is determined by the correlation between the displacements of different atoms. It is relevant the fact that these correlations are important only over short distances, so the sum extends only over few lattice sites and the scattering has an appreciable width. For these reasons this contribution is known as *thermal diffuse scattering* (TDS).

When an experiment is carried on in the TDS it is necessary to consider the background intensity which sometimes is subtracted from the data. Or also, TDS can be study on its own, as it provides information on the low-energy elastic wave in the lattice. In these experiments the TDS is mapped out over a large volume of the reciprocal space.

The separation of the total scattered intensity into a sharp Bragg and diffuse component in the presence of thermal vibrations is useful whenever there are random atomic displacements, static or dynamic, from the lattice sites. An example of static distortions are the lattice defects, largely studied using diffuse scattering.

2.2.1 Properties of Debye-Waller factor

In the general case of a crystal with several different types of atoms in the unit cell, the structure factor becomes

$$\mathbf{F}^{u.c.} = \sum_j f_j(\mathbf{Q})e^{-M_j} e^{i\mathbf{Q}\cdot\mathbf{r}_j}$$

where the Debye-Waller factor for the j -atom in the unit cell is given by

$$M_j = \frac{1}{2}Q^2 \langle u_{Qj}^2 \rangle = \frac{1}{2} \left(\frac{4\pi}{\lambda} \right)^2 \sin^2\theta \langle u_{Qj}^2 \rangle = B_T^j \left(\frac{\sin\theta}{\lambda} \right)^2$$

for the specific j^{th} atom, and $B_T^j = 8\pi^2 \langle u_{Qj}^2 \rangle$. In general, B_T^j is an ellipsoid which represents the 3D-vibrations of the single j -atom around the equilibrium position. The simplest situation is when the atom vibrates isotropically, then $\langle u^2 \rangle = \langle u_x^2 \rangle = \langle u_y^2 \rangle = \langle u_z^2 \rangle = 3\langle u_Q^2 \rangle$, and

$$B_{isotropic} = \frac{8\pi^2}{3} \langle u^2 \rangle$$

so in this case the general ellipsoid become a sphere.

In general, every atom of a compound have a different value for the Debye-Waller factor, for the simple reason that the lighter atoms will generally vibrate more than heavier ones. Also the Debye-Waller factor is not isotropic in general, as the bonding will also restrict the vibrations along certain directions. For example, it usually costs less energy to change the bond angle than the bond length, so the vibrations of atoms located at the end of bonds will have a larger amplitude perpendicular to the bond than along it.

2.3 Inelastic X-ray scattering (IXS)

The main result of the previous section is the fact that the intensity scattered by a crystal, where the atomic vibrations are allowed, is the sum of the Bragg intensity and the TDS. What we want to do now is to study the TDS expression more in detail, in order to understand all the different contribution, in particular the first-order which is related to the IXS scattered intensity. The first step is to restart from equation 2.1 and from the definition of the structure factor. Then we have to substitute the expression for the instantaneous displacement, $\mathbf{u}(\kappa l)$, which is the result of the Born-von Karman theory.

Remember that the atoms have the equilibrium positions at $\mathbf{r}(\kappa l)$,

$$\mathbf{r}(\kappa l) = \mathbf{r}(\kappa) + \mathbf{r}(l) \quad (2.4)$$

where $\mathbf{r}(l)$ is the position of the l^{th} lattice point with respect to the origin. The instantaneous displacement $\mathbf{u}(\kappa l)$ is given by the equation:

$$\mathbf{u}(\kappa l) = (Nm(\kappa))^{-\frac{1}{2}} \sum_{j\mathbf{q}} \left(\frac{E_j(\mathbf{q})}{\omega_j^2(\mathbf{q})} \right)^{\frac{1}{2}} \mathbf{e}(\kappa|j\mathbf{q}) e^{i(\mathbf{q}\cdot\mathbf{r}(\kappa l) - \omega_j(\mathbf{q})t)} \quad (2.5)$$

Where the summation is extended on all the $3nN$ modes ($j\mathbf{q}$), where n is the number of atoms in the cell and N in the number of the cells in the crystal. The index j labels one branch of the phonon relations, and the wave vector \mathbf{q} runs over the N uniformly distributed vectors in the Brillouin zone. The structure factor in this notation is written as

$$F(\mathbf{Q}) = \sum_{\kappa l} f_{\kappa}(\mathbf{Q}) \exp[i\mathbf{Q} \cdot (\mathbf{r}(\kappa l) + \mathbf{u}(\kappa l))] \quad (2.6)$$

The isolated atom form factor f_{κ} is independent of the unit cell, but is a function of the scattering vector \mathbf{Q} , given by

$$\mathbf{Q} = \mathbf{k}' - \mathbf{k} \quad (2.7)$$

where \mathbf{k} and \mathbf{k}' are the incident and scattered wave vectors of the X-rays respectively. Let's rewrite the Equation 2.1 using the expression for \mathbf{u}

$$I(\mathbf{Q}) = \sum_{\kappa l} \sum_{\kappa' l'} f_{\kappa}(\mathbf{Q}) f_{\kappa'}(\mathbf{Q}) \exp[i\mathbf{Q} \cdot (\mathbf{r}(\kappa l) - \mathbf{r}(\kappa' l'))] \langle \exp[i\mathbf{Q} \cdot (\mathbf{u}(\kappa l) - \mathbf{u}(\kappa' l'))] \rangle \quad (2.8)$$

where the time average on the second exponential represent the effect of the thermal motion on the scattered intensity. Thanks to the *Baker-Hausdorff theorem*

$$\langle e^{ix} \rangle = e^{-\frac{1}{2}\langle x^2 \rangle} \quad (2.9)$$

it is possible to rewrite the averaged quantity, which is the so called *Debye-Waller factor*

$$\exp\left[-\frac{1}{2}\langle |\mathbf{Q} \cdot (\mathbf{u}(\kappa l) - \mathbf{u}(\kappa' l'))|^2 \rangle\right] \quad (2.10)$$

Now substitute the expression of \mathbf{u} in the Equation 2.8, remember that the phases of the modes are independent of each other, so the contribution of the cross product disappears. The exponential term is now composed by four different terms:

$$(Nm(\kappa))^{-1} \sum_{j\mathbf{q}} |\mathbf{Q} \cdot \mathbf{e}(\kappa|j\mathbf{q})|^2 \frac{E_j(\mathbf{q})}{\omega_j^2(\mathbf{q})}$$

Chapter 2. Experimental Techniques

$$\begin{aligned}
& -N^{-1}(m(\kappa)m(\kappa'))^{-\frac{1}{2}} \sum_{j\mathbf{q}} (\mathbf{Q} \cdot \mathbf{e}(\kappa|j\mathbf{q})) (\mathbf{Q} \cdot \mathbf{e}^*(\kappa'|j\mathbf{q})) \frac{E_j(\mathbf{q})}{\omega_j^2(\mathbf{q})} e^{i\mathbf{q} \cdot (\mathbf{r}(\kappa l) - \mathbf{r}(\kappa' l'))} \\
& -N^{-1}(m(\kappa)m(\kappa'))^{-\frac{1}{2}} \sum_{j\mathbf{q}} (\mathbf{Q} \cdot \mathbf{e}^*(\kappa|j\mathbf{q})) (\mathbf{Q} \cdot \mathbf{e}(\kappa'|j\mathbf{q})) \frac{E_j(\mathbf{q})}{\omega_j^2(\mathbf{q})} e^{i\mathbf{q} \cdot (\mathbf{r}(\kappa l) - \mathbf{r}(\kappa' l'))} \\
& (Nm(\kappa))^{-1} \sum_{j\mathbf{q}} |\mathbf{Q} \cdot \mathbf{e}(\kappa'|j\mathbf{q})|^2 \frac{E_j(\mathbf{q})}{\omega_j^2(\mathbf{q})}
\end{aligned}$$

Define now the *Debye-Waller factor*

$$M_\kappa(\mathbf{Q}) = \frac{1}{2Nm(\kappa)} \sum_{j\mathbf{q}} |\mathbf{Q} \cdot \mathbf{e}(\kappa|j\mathbf{q})|^2 \frac{E_j(\mathbf{q})}{\omega_j^2(\mathbf{q})} \quad (2.11)$$

so the initial exponential became the product of three different terms: the first two are e^{-M_κ} which represents the intensity reduction of the Bragg scattering, the last term is an exponential containing the scalar products $(\mathbf{Q} \cdot \mathbf{e}(\kappa|j\mathbf{q}))(\mathbf{Q} \cdot \mathbf{e}^*(\kappa'|j\mathbf{q}))$ and $(\mathbf{Q} \cdot \mathbf{e}^*(\kappa|j\mathbf{q}))(\mathbf{Q} \cdot \mathbf{e}(\kappa'|j\mathbf{q}))$ which are associated to the correlations between the displacements of different atoms.

In order to obtain all the different components of the scattering, it is possible to expand this last exponential term $\exp\{\dots\}$ in series:

$$\exp\{\dots\} = 1 + \{\dots\} + \frac{1}{2!}\{\dots\}^2 + \dots \quad (2.12)$$

and, substituting this expansion in the original equation for the scattering intensity, the total intensity is a series of different contributions:

$$I(\mathbf{Q}) = I_0 + I_1 + I_2 + \dots \quad (2.13)$$

where

$$\begin{aligned}
I_0 &= \sum_{\kappa l} \sum_{\kappa' l'} f_\kappa(\mathbf{Q}) e^{-M_\kappa} f_{\kappa'}(\mathbf{Q}) e^{-M_{\kappa'}} e^{i\mathbf{Q} \cdot (\mathbf{r}(\kappa l) - \mathbf{r}(\kappa' l'))} \\
I_1 &= \sum_{\kappa l} \sum_{\kappa' l'} f_\kappa(\mathbf{Q}) e^{-M_\kappa} f_{\kappa'}(\mathbf{Q}) e^{-M_{\kappa'}} \frac{1}{2N} (m(\kappa)m(\kappa'))^{-1/2} \\
& \times \sum_{j\mathbf{q}} \frac{E_j(\mathbf{q})}{\omega_j^2(\mathbf{q})} (\mathbf{Q} \cdot \mathbf{e}(\kappa|j\mathbf{q})) (\mathbf{Q} \cdot \mathbf{e}^*(\kappa'|j\mathbf{q})) e^{i(\mathbf{Q}+\mathbf{q}) \cdot (\mathbf{r}(\kappa l) - \mathbf{r}(\kappa' l'))}
\end{aligned} \quad (2.14)$$

For now let's focus on the first term, I_0 , which can be written as

$$\left| \sum_{\kappa l} f_\kappa(\mathbf{Q}) \exp(-W_\kappa(\mathbf{Q})) \exp[i\mathbf{Q} \cdot \mathbf{r}(\kappa l)] \right|^2 \quad (2.15)$$

and we can separate the sum in two parts, one relative to the lattice and the other to the basis contained into the primitive unit cell:

$$I_0 = \left| \sum_{\kappa} f_\kappa(\mathbf{Q}) \exp(W_\kappa) \exp(i\mathbf{Q} \cdot \mathbf{r}(\kappa)) \right|^2 \left| \sum_l \exp(i\mathbf{Q} \cdot \mathbf{r}(l)) \right|^2 \quad (2.16)$$

2.3. Inelastic X-ray scattering (IXS)

The second term is a sum of phase factors that is non vanishing only when the exponential is multiple integer of 2π , so

$$\left| \sum_l \exp(i\mathbf{Q} \cdot \mathbf{r}(l)) \right|^2 = \frac{(2\pi)^3 N}{v_a} \sum_{\mathbf{G}} \delta(\mathbf{Q} - \mathbf{G}) \quad (2.17)$$

where \mathbf{G} is the vector to any discrete point of the reciprocal lattice and v_a is the volume of the direct unit cell. This expression is the so-called *Laue interference function*, which describes the intensity scattered from a set of identical scatters located at the lattice points $\mathbf{r}(l)$. It represents the general result that the Laue interference function is zero at all points in reciprocal space except for those where the Bragg scattering condition is satisfied

$$\mathbf{Q} = \mathbf{G} \quad (2.18)$$

So, in the end the expression for I_0 is:

$$I_0 = \frac{(2\pi)^3}{v_a} N \sum_{\mathbf{H}} |F(\mathbf{Q})|^2 \delta(\mathbf{Q} - \mathbf{G}) \quad (2.19)$$

with

$$F(\mathbf{H}) = \sum_{\kappa} f_{\kappa}(\mathbf{G}) e^{-M_{\kappa}} e^{i\mathbf{G} \cdot \mathbf{r}(\kappa)} \quad (2.20)$$

Now the next term in the intensity expression for I is I_1 . Proceeding in the same way and separate the summations over κ and l , the result is

$$I_1 = \frac{1}{N} \frac{E_j(\mathbf{q})}{\omega_j^2(\mathbf{q})} \left| \sum_{\kappa} m(\kappa)^{-\frac{1}{2}} f_{\kappa}(\mathbf{Q}) e^{-M_{\kappa}} \mathbf{Q} \cdot \mathbf{e}(\kappa|\mathbf{j}\mathbf{q}) e^{i(\mathbf{Q}-\mathbf{q}) \cdot \mathbf{r}(\kappa)} \right|^2 \left| \sum_l e^{i(\mathbf{Q}-\mathbf{q}) \cdot \mathbf{r}(l)} \right|^2 \quad (2.21)$$

From equation 2.17, replacing \mathbf{Q} with $\mathbf{Q} - \mathbf{q}$ the expression can be rewritten as

$$\left| \sum_l e^{i(\mathbf{Q}-\mathbf{q}) \cdot \mathbf{r}(l)} \right|^2 = \frac{(2\pi)^3 N}{v_a} \sum_{\mathbf{G}} \delta(\mathbf{Q} - \mathbf{q} - \mathbf{G}) \quad (2.22)$$

So the intensity I_1 vanishes unless \mathbf{Q} satisfies the relation

$$\mathbf{Q} = \mathbf{G} + \mathbf{q} \quad (2.23)$$

The $3n$ modes sharing the same wave vector \mathbf{q} produce scattering at the points of the reciprocal space defined by the condition 2.23. This is the first-order, or one-phonon, scattering, and gives the scattering intensity of IXS.

The summation over κ in the expression

$$\sum_{\kappa} m(\kappa)^{-\frac{1}{2}} f_{\kappa} e^{-M_{\kappa}} \mathbf{Q} \cdot \mathbf{e}(\kappa|\mathbf{i}\mathbf{q}) e^{i\mathbf{Q} \cdot \mathbf{r}(\kappa)}$$

plays the same role in the first-order scattering as the structure factor \mathbf{F} in the Bragg scattering, it is called the *structure factor for the first-order scattering*.

Chapter 2. Experimental Techniques

2.3.1 The Scattering cross-section

Phonons correspond to waves travelling through the crystal and are characterized by a propagation vector \mathbf{q} and a polarization vector $\mathbf{e}(\mathbf{q})$. The physical quantity that can be experimentally measured is the double-differential cross section: $\frac{d^2\sigma}{d\Omega dE_f}$, and it is proportional to the number of incident photons scattered into the solid angle $d\Omega$ within the energy range E_f and $E_f + dE_f$. For scattering of an x-ray from an initial state given by photon momentum \mathbf{k} , and polarization \mathbf{e} , to a final state given by \mathbf{k}' , \mathbf{e}' the cross-section is written as:

$$\frac{d^2\sigma}{d\Omega dE}(\mathbf{Q}, \omega) = \frac{k'}{k} \frac{2\pi^3}{2v_a} \sum_j \sum_{\mathbf{G}} \frac{1}{\omega^2} F^2(\mathbf{q}, \mathbf{Q}) \langle n_q^j + \frac{1}{2} \pm \frac{1}{2} \rangle [\delta(\hbar\omega \mp \hbar\omega_j) \delta(\mathbf{Q} \mp \mathbf{q} - \mathbf{G})] \quad (2.24)$$

Thanks to the validity of the adiabatic approximation, it is possible to separate the general problem into an electronic and a nuclear part. The contribution to the total scattering coming from the valence electrons close to the Fermi level is small compared to the contribution coming from the core electrons. Thus, it is possible to assume that the electronic part of the total wave function is not changed by the scattering process, and the difference between initial and final state is due to excitations of the ion system.

So, the double differential cross-section can be separated in two parts

$$\frac{d^2\sigma}{d\Omega dE_f} = \left(\frac{d\sigma}{d\Omega} \right)_{Th} \cdot S(\mathbf{Q}, E) \quad (2.25)$$

where the first term is the Thomson scattering cross-section

$$\left(\frac{d\sigma}{d\Omega} \right)_{Th} = r_0^2 (\mathbf{e}_f \cdot \mathbf{e}_i)^2 \left(\frac{k_f}{k_i} \right) \quad (2.26)$$

which describes the coupling between the electromagnetic field of the incoming photons and the electrons of the system. For this type of interaction this term is very small because r_0^2 is of the order of 10^{-25}cm^2 and also because the energy transfer is very small compared to the initial energy of the beam. The second term, $S(\mathbf{Q}, E)$ is the scattering function: it describes the sample properties in the absence of the perturbing probe and it gives information about the dynamics of the system from an inelastic scattering experiment.

The expression of the scattering function can be again divided in two parts in the case of single phonon studies and under the adiabatic approximation

$$S(\mathbf{Q}, E) = \sum_j F(\mathbf{q}, \mathbf{Q}) G(E, T, \mathbf{Q}) \quad (2.27)$$

Here the first term is the one-phonon structure factor

$$F(\mathbf{q}, \mathbf{Q}) = \left| r_0 \sum_i f_i(\mathbf{Q}) \frac{(\mathbf{Q} \cdot \mathbf{e}_i^j(\mathbf{q}))}{\sqrt{m_i}} e^{-i\mathbf{Q} \cdot \mathbf{r}_i} e^{-M_i} \right| \quad (2.28)$$

where m_i is the mass of the i -atom, $(\mathbf{e}_i^j, \omega^j)$ the polarization and the energy of the j -phonon branch. The second term is the thermal factor

$$G(E, T, \mathbf{Q}) = \langle n_q^j + \frac{1}{2} \pm \frac{1}{2} \rangle \delta(E \mp E_j(\mathbf{Q})) \quad (2.29)$$

2.3. Inelastic X-ray scattering (IXS)

and specifies the probability of creation or annihilation of a phonon. Of course, in the above equation, the + sign is for energy loss of the X-ray beam and the - is for energy gain, and n_q^j takes into account the fact that the phonon population follows the Bose-Einstein statistics:

$$\langle n_q^j + 1 \rangle = \frac{1}{e^{\frac{\hbar\omega_j}{k_B T}} - 1} + 1 \quad \langle n_q^j \rangle = \frac{1}{e^{\frac{\hbar\omega_j}{k_B T}} - 1} \quad (2.30)$$

The scalar product of the phonon polarization and the scattering vector, $\mathbf{Q} \cdot \hat{\epsilon}_i^j(\mathbf{q}_{ph})$ allows to choose a particular mode in the experiment, normally there will be a possibility to distinguish transverse from longitudinal lattice vibrations. By choosing a transverse scattering configuration in which $\mathbf{q}_{ph} \perp \mathbf{Q}$, only the transverse phonon can be detected, because the transverse phonon polarization is nearly parallel to the scattering vector \mathbf{Q} . In the same way it is possible to choose a scattering geometry in which the transverse phonon polarization is perpendicular to the scattering vector, and we will measure only longitudinal phonons.

Typically experiments to measure the phonon dispersion relations as a function of the reduced wave vector \mathbf{q} require a relatively high resolution, on the order of 1 meV. This is achieved, starting from energy around 10-30 keV, by using a high resolution monochromator in back-scattering geometry, see Chapter 1, and exploiting the dynamical diffraction theory of perfect crystals. By investigating different Brillouin zones, it is possible to discriminate the character of the lattice vibrations.

Cerium Antimony and Cerium Bismuth

Among all cerium compounds, the mononictides CeX ($X = N, P, As, Sb, Bi$) exhibit highly unusual magnetic properties, especially the heavier mononictides $CeSb$ and $CeBi$. The origin of this behavior is the presence of the 4f level close to the Fermi energy, E_f , which is a general characteristic of anomalous rare earth systems like cerium ones. The main typical properties are a very small crystalline electric field (CEF) splitting, a very large magnetic anisotropy, a complex magnetic phase diagram, unusual spectra of magnetic excitation and a large sensitivity of these properties to an applied hydrostatic pressure. These are, briefly, the main features of these compounds and what makes them interesting and stimulate a lot of scientists in the world. In this chapter, after a crystallographic analysis of the compounds, the attention is focused on the description of the electronic properties and the magnetic phase diagrams at low temperature, analyzing all the possible superlattice structures that are present.

3.1 Crystallographic properties

The all class of cerium compounds have a very simple crystallographic structure, with two atoms per unit cell. In particular, these shows a typical rock-salt structure, which can be regarded as an *f.c.c.* lattice with a basis of two atoms. From this structure, they should be very simple systems, with only six different dispersion curves and three different elastic constant. However they have interesting low-temperature magnetic behavior, showing a wide variety of interesting effects, that were investigated a lot in the past. In this work our attention is focused on two specific compounds: Cerium Bismuth ($CeBi$) and Cerium Antimony ($CeSb$), that shows a magnetic phase diagrams that probably are ones of the most complex found among the lanthanide mononictides.

Cerium Bismuth and Cerium Antimony crystal structure is simply based on a traditional

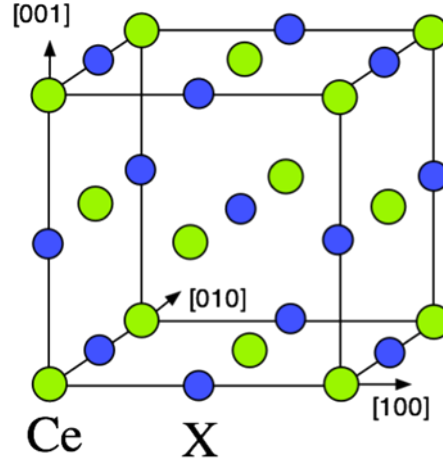


Figure 3.1: Graphical representation of the NaCl-like crystal structure of the CeX compounds.

	CeBi	CeSb	CeP	CeAs
a (Å)	6.500	6.412	5.932	6.078
T_N (K)	25.2	16.1	8.5	7.5
Δ_{CF} (K)	8 ± 3	37 ± 3	172 ± 3	159 ± 2
μ_S (μ_B)	2.10	2.06	0.85	0.85

Table 3.1: Table with important parameters of cerium compounds: lattice constant at room temperature, Néel temperature, crystal field splitting and total magnetic moment.

cubic lattice, with space group $Fm-3m$, number 225. The lattice constant are respectively:

$$\begin{aligned}
 a, b, c &= 6.500 \text{ \AA}, \\
 \alpha, \beta, \gamma &= 90^\circ \\
 a, b, c &= 6.412 \text{ \AA}, \\
 \alpha, \beta, \gamma &= 90^\circ
 \end{aligned}$$

The Wyckoff positions of the atoms in the unit cell displayed in figure are:

- 4a: (0, 0, 0) for Cerium atom;
- 4b: $(\frac{1}{2}, \frac{1}{2}, \frac{1}{2})$ for Antimony or Bismuth atoms.

An important analysis, from a crystallographic point of view, is the one that regards the structure factor \mathbf{F} which is the scattering amplitude from a crystalline material, directly related to the intensity of the Bragg peaks.

The general expression for the structure factor is

$$F^{crystal}(\mathbf{Q}) = \sum_l^{\text{All atoms}} f_l(\mathbf{Q}) e^{i\mathbf{Q} \cdot \mathbf{r}_l} \quad (3.1)$$

3.1. Crystallographic properties

where $f_l(\mathbf{Q})$ is the atomic form factor of the atom situated at position \mathbf{r}_l . It is known that a crystal structure can be seen as a convolution between a lattice and atom positions. So $\mathbf{r}_l = \mathbf{R}_n + \mathbf{r}_j$, where \mathbf{R}_n is a vector that select each conventional unit cell and \mathbf{r}_j labels the position of an atom within the unit cell. Since the scattering amplitude is nothing other than the Fourier transform of the crystal structure, it follows that this must be equal to the product of the Fourier transform of the functions describing the lattice and the basis:

$$F^{crystal}(\mathbf{Q}) = \sum_l^{\text{All atoms}} f_l(\mathbf{Q}) e^{i\mathbf{Q}\cdot\mathbf{R}_n + \mathbf{r}_j} = \sum_n^{\text{lattice}} e^{i\mathbf{Q}\cdot\mathbf{R}_n} \sum_j^{\text{unit cell}} f_j(\mathbf{Q}) e^{i\mathbf{Q}\cdot\mathbf{r}_j} \quad (3.2)$$

The first term is a sum over the lattice, while the second is over the basis of atoms and it is called *unit cell structure factor*,

$$F^{u.c.}(\mathbf{Q}) = \sum_j f_j(\mathbf{Q}) e^{i\mathbf{Q}\cdot\mathbf{r}_j} \quad (3.3)$$

Let's first consider the lattice sum, that is label as $S_N(\mathbf{Q})$. The general term is $e^{i\mathbf{Q}\cdot\mathbf{R}_N}$, which implies that the sum of all phase factors is non vanishing only when the exponential is multiple of 2π . The condition becomes:

$$\mathbf{Q} \cdot \mathbf{R}_n = 2\pi \times \text{integer}$$

This relation is satisfied only if the scattering vector \mathbf{Q} is equal to a reciprocal lattice vector \mathbf{G}_{hkl} . This is the *Laue condition* [10]:

$$\mathbf{Q}_{hkl} \cdot \mathbf{R}_n = 2\pi(hn_1 + kn_2 + ln_3)$$

In this case the phase of scattered waves add up coherently. So the consequence of this first sum is expressed by this relation: $\mathbf{Q} = \mathbf{G}$.

Now turn to the evaluation of the unit cell structure factor defined in Eq. 3.3. This factor is the one of the conventional unit cell reported in Figure 3.1, where it is possible to observe that the structure is a convolution of an *fcc* lattice with a basis formed by two atoms. So the total unit cell structure factor can be evaluated as the product of the one for the *fcc* times the one associated to the basis.

Let's start with the first one; the *fcc* lattice can be regarded as a simple cubic with a lattice spacing a , with a basis consists of four atoms at

$$\mathbf{r}_1 = 0, \quad \mathbf{r}_2 = \frac{1}{2}(\mathbf{a}_1 + \mathbf{a}_2), \quad \mathbf{r}_3 = \frac{1}{2}(\mathbf{a}_2 + \mathbf{a}_3), \quad \mathbf{r}_4 = \frac{1}{2}(\mathbf{a}_3 + \mathbf{a}_1)$$

where \mathbf{a}_1 , \mathbf{a}_2 and \mathbf{a}_3 are the basis vectors for the simple cubic lattice:

$$\mathbf{a}_1 = a\hat{x}, \quad \mathbf{a}_2 = a\hat{y}, \quad \mathbf{a}_3 = a\hat{z}$$

The choice of this cell implies that the reciprocal lattice is also a simple cubic with a lattice spacing $2\pi/a$. It is important to notice that the atoms sitting in the *fcc* lattice positions are the same, they have the same structure factor, so the unit cell structure factor is:

$$F^{fcc} = f(\mathbf{G}) \sum_j e^{i\mathbf{G}\cdot\mathbf{r}_j} = f(\mathbf{G})(1 + e^{i\pi(h+k)} + e^{i\pi(k+l)} + e^{i\pi(l+h)})$$

Chapter 3. Cerium Antimony and Cerium Bismuth

$$= f(\mathbf{G}) \times \begin{cases} 4 & \text{if } h, k, l \text{ are all even or all odd} \\ 0 & \text{otherwise} \end{cases} \quad (3.4)$$

So, for example, the (1,0,0) reflection has a vanishing structure factor: the reflection is said to be forbidden. With this analysis it is possible to notice that not all the reflection are allowed and the ones that are available have all the same intensity.

Now we have to add the fact that our crystal structure is not a normal *fcc*, but we have a basis. In particular, from International Tables for Crystallography [11], it is possible to observe that to describe this structure, the Cerium atom is in position (0,0,0) and the Antimony, or Bismuth, is in position (1/2,1/2,1/2) with respect to the canonical basis for the *fcc*: $\mathbf{a}_1, \mathbf{a}_2, \mathbf{a}_3$

$$\mathbf{a}_1 = \frac{a}{2}(\hat{y} + \hat{z}), \quad \mathbf{a}_2 = \frac{a}{2}(\hat{z} + \hat{x}), \quad \mathbf{a}_3 = \frac{a}{2}(\hat{x} + \hat{y})$$

The reciprocal space is a *bcc* with a side of $\frac{4\pi}{a}$ and the general form of a reciprocal lattice vector is

$$\mathbf{G} = h\mathbf{b}_1 + k\mathbf{b}_2 + l\mathbf{b}_3$$

where $\mathbf{b}_1, \mathbf{b}_2, \mathbf{b}_3$ are the basis vectors obtained from $\mathbf{a}_1, \mathbf{a}_2, \mathbf{a}_3$

$$\mathbf{b}_1 = \frac{4\pi}{a} \frac{1}{2}(\hat{y} + \hat{z} - \hat{x}), \quad \mathbf{b}_2 = \frac{4\pi}{a} \frac{1}{2}(\hat{z} + \hat{x} - \hat{y}), \quad \mathbf{b}_3 = \frac{4\pi}{a} \frac{1}{2}(\hat{x} + \hat{y} - \hat{z})$$

The advantage of this approach is that the structure factor can be written as the product of the structure factor of an *fcc* lattice and the two atom basis

$$F^{CeSb} = (1 + e^{i\pi(h+k)} + e^{i\pi(k+l)} + e^{i\pi(l+h)}) \times (f^{Ce}(\mathbf{G}) + f^{Sb}(\mathbf{G})e^{i2\pi(h/2+k/2+l/2)}) \quad (3.5)$$

and the same equation for CeBi with, of course, $f^{Bi}(\mathbf{G})$ instead of $f^{Sb}(\mathbf{G})$.

For the second part of the structure factor it is possible to observe that

$$\begin{aligned} F^{basis}(\mathbf{G}) &= f^{Ce}(\mathbf{G}) + f^{Sb/Bi}(\mathbf{G})e^{i\pi(h+k+l)} \\ &= \begin{cases} f^{Ce}(\mathbf{G}) + f^{Sb/Bi}(\mathbf{G}) & \text{if } h+k+l = \text{even} \\ f^{Ce}(\mathbf{G}) - f^{Sb/Bi}(\mathbf{G}) & \text{if } h+k+l = \text{odd} \end{cases} \end{aligned} \quad (3.6)$$

In conclusion, the effect of the basis is to modify the intensity of the allowed reflections, which are selected from the *fcc* structure. As an example, these are the structure factors for the (4,0,0) and (5,1,1) reflections:

$$\begin{aligned} F_{400} &= 4(f^{Ce}(4, 0, 0) + f^{Sb/Bi}(4, 0, 0)) \\ F_{511} &= 4(f^{Ce}(5, 1, 1) - f^{Sb/Bi}(5, 1, 1)) \end{aligned} \quad (3.7)$$

where, of course, $f^{Ce}(\mathbf{G}) \neq f^{Sb}(\mathbf{G}) \neq f^{Bi}(\mathbf{G})$ since they have a different electronic distribution. Furthermore what is important is that the difference in the sign in Eq. 3.7 does not affect the intensity only. This is also associated to the motion of atom for that specific reflection: for *even* reflections, the plus sign means that there is an in-phase motion of the atoms which is characteristic of an acoustic wave, and for odd reflection the stands for an out of phase motion, which define the optical modes. So this is another important tool during an IXS experiment in order to select a specific mode.

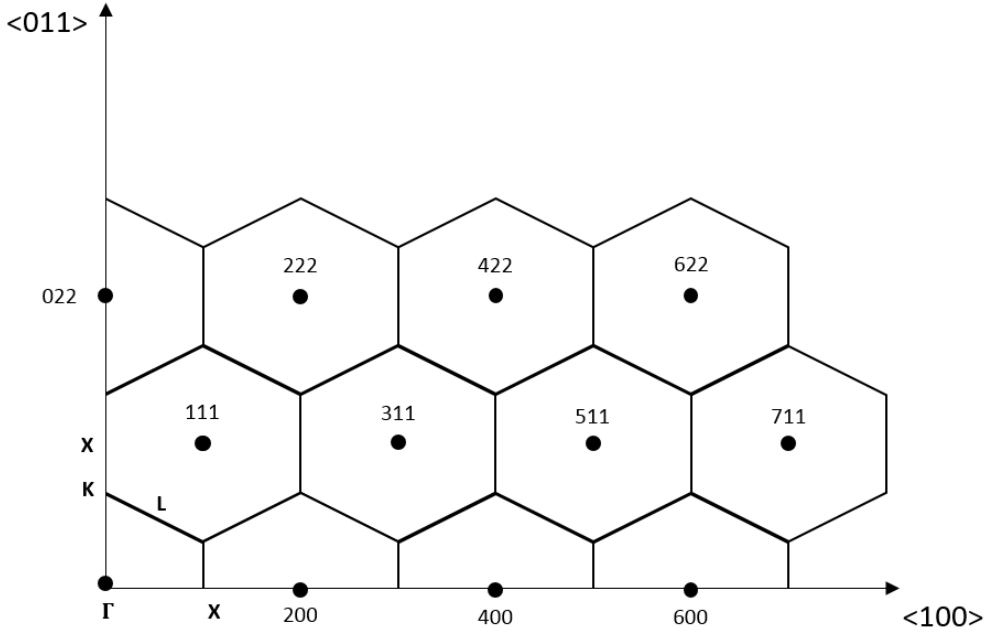


Figure 3.2: Section of the reciprocal lattice in the plane defined by directions $\langle 100 \rangle$ and $\langle 011 \rangle$

3.2 Electronic properties

It is useful to spend few words about the electronic structure of these compounds. As already said, both compounds crystallize in the rock-salt structure so that the rare-earth ion sites have octahedral symmetry. The magnetic properties originate from the single $4f$ -electron of Ce^{3+} ions with the free-ion $^2F_{5/2}$ multiples as a ground state. Due to the crystal field, the ground state multiplet is divided into a doublet Γ_7 and a quartet Γ_8 , with Γ_7 as the ground state. The excited multiplet state, $\mathbf{J} = 7/2$, lies at 280 meV ($\sim 3250\text{K}$) above and may be ignored in the discussion because of the much smaller splitting of the ground-state multiplet [12].

One of the main important features of CeBi and CeSb, with respect to the other cerium compounds, is the fact that the crystal-field splitting is much smaller, 37 and 8 K respectively [13], and the saturated magnetic moments have about the full free-ion moment value. Also the magnetic phase transition T_N is connected with a structural phase transition in a small tetragonal distortion [14] [15].

In zero magnetic field, antiferromagnetic order occurs at 25 K and 16 K for CeBi and CeSb [16]. Below Néel temperature, T_N , the magnetization in increasing magnetic field approaches stepwise the ferromagnetic saturation value with the free-ion moment of $2.14 \mu_B$ for Ce^{3+} . The main interesting and unusual feature of these structures are the so-called antiferropara- (AFP) phases. They are composed by a periodic absence of a moment on certain planes, the so called "paramagnetic planes". The moments on the other planes, ferromagnetically ordered, carry almost the free-ion value of $2.14 \mu_B$ for CeSb, and $2.10 \mu_B$ for CeBi. The long period magnetic structure in the different magnetic phases are constructed by various stacking of the paramagnetic Ce-ion (100) planes and the ferromagnetic ones whose direction is along the [100] direction. Experiments show that the magnetic moment of Ce

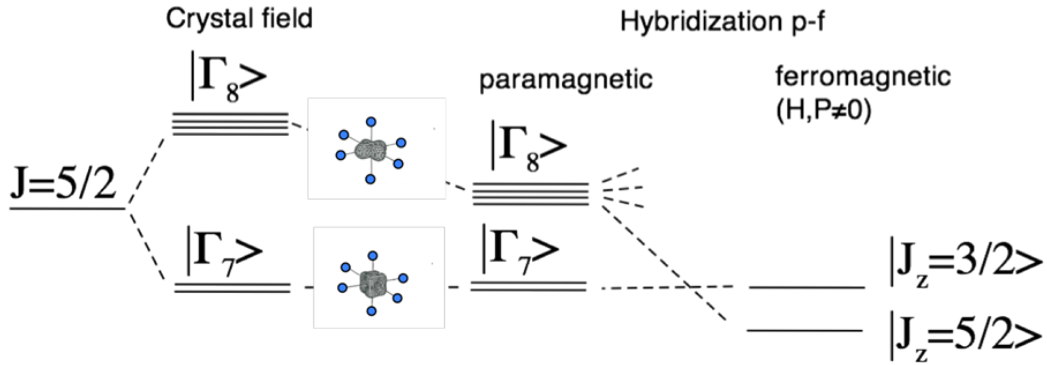


Figure 3.3: Schematic representation of the p - f mixing described by Kasuya's group. First there is a splitting due to the crystal field interaction in octahedral symmetry, then the hybridization between p hole orbitals and $4f$ electron cause a shift in energy.

ions in the ferromagnetic layers is $2\mu_B$ per Ce ion, oriented along [001] axis, and of course, the moment in the paramagnetic planes is 0 or very small. The crystal-field ground state of Ce^{3+} in the paramagnetic phase is so addressed as the Γ_7 doublet, whose magnetic moment is very small, about $0.71 \mu_B$ for CeSb. On the other hand, the excited state Γ_8 is characterized by a magnetic moment of $1.57 \mu_B$, very close to the value observed in the oriented phases. These observations led us to classify the paramagnetic planes as formed by Γ_7 ions, and oriented planes as formed by Γ_8 ions.

Added on this splitting due to the crystal field interaction there is also an hybridization between the p hole orbitals of the neighboring pnictogens and the Γ_8 state of the Ce ions, within the ferromagnetic layers. This model, the p - f mixing model [17], was developed by Kasuya's during the 20th century, and it is based on the fact that Γ_7 and Γ_8 are two completely different atoms in terms of valence and interaction with the lattice. It also predicts a mixing between p hole orbitals and Γ_8 $4f$ electrons, while the Γ_7 remain unchanged. This cause a variation in energy of the orbitals.

The ordering of two kinds of $4f$ -electron states in CeX also give rise to the crystal-lattice anomalies. The ionic size of the Γ_8 -like Ce ions is smaller than that in the Γ_7 state, because Γ_8 -like orbitals has a smaller expansion along the moment direction and a shorter interatomic distance within the ferromagnetic planes due to the mixing effect. Due to this mixing effect, Cerium atoms behave in different way, so there are three different lattice distance: d_{Γ_7} , d_{Γ_7-8} and d_{Γ_8} .

3.3 CeSb magnetic phase diagram

The magnetic phase diagram of Cerium Antimony is one of the most complex among the all class of lanthanides compounds. It consists in at least fourteen different phases, each one characterized by a particular long range magnetic ordering. in the 20th century, many neutron diffraction experiments were carried out, giving useful informations [18].

CeSb orders, with a first order transition, at $T_N \approx 16.2$ K and undergoes at least seven phase transitions, which can be seen also from the profile of the specific heat in zero field, see Figure 3.5 [19][20]. All the phases are commensurate and correspond to a specific periodic

3.3. CeSb magnetic phase diagram

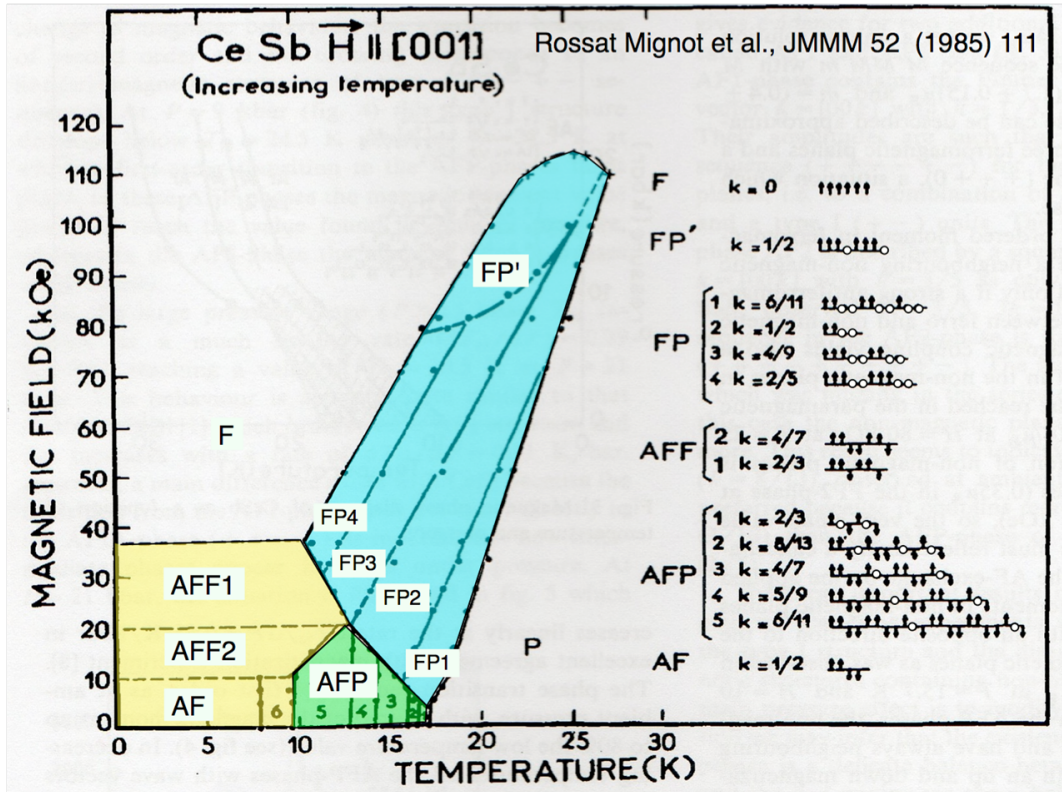


Figure 3.4: Magnetic phase diagram of CeSb. Picture taken from ref. [18]

stacking of non magnetic and ferromagnetic (001) planes with an up or down magnetization, see Figure 3.6. By decreasing the temperature the ordering becomes very long range. Below $T_0 \approx 8$ K non magnetic planes disappear and the order transforms into a nearly type IA structure.

The magnetic phase diagram, in Figure 3.4, can be divided in three regions:

1. A low temperature region, the yellow one, containing phases, called AFF-phases, which corresponds to a stacking of ferromagnetic sheets with sequences associated with the wave vector $\mathbf{q} = [00q]$ with $q = 4/7, 2/3$ and 0 . The transitions are characterized only by a change of magnetization.
2. A low field and high temperature region, the green one, which contains the so-called AFP-phases. The transitions are associated only with an entropy variations.
3. A high field and high T region, the blue one, with the so called FP-phases in which both entropy and magnetization variations occur at the phase transitions. These FP-phases correspond to a stacking of ferromagnetic layers with a moment of about $2 \mu_B$ and non magnetic layers.

This quite unique behaviour can be understood within the frame of the p-f mixing. In the paramagnetic state the Ce^{3+} ground state is probably the Γ_7 doublet, the $\Gamma_7 - \Gamma_8$ splitting is strongly reduced by the p-f mixing [21]. In the ordered states a Γ_8 state, nearly a $|5/2\rangle$ state,

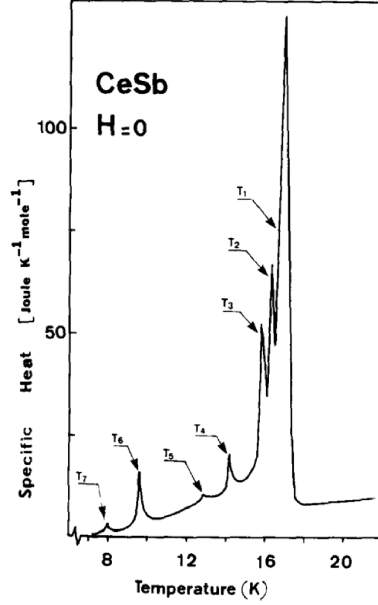


Figure 3.5: Specific heat of CeSb in different temperatures at zero applied field. Picture taken from ref. [14]

is favored by the strong p-f mixing within the (001) plane. This mixing is at the origin of the strong planar coupling and anisotropy observed both in CeSb and CeBi.

3.4 CeBi magnetic phase diagram

While the magnetic properties of CeBi are quite unusual, they are in some sense less complicated than those of CeSb [22]. CeBi orders at $T_N \approx 25.2$ K [23] with a type I structure (+ - + -) with a second order phase transition. At $T = T_N/2$ a first order transition to-

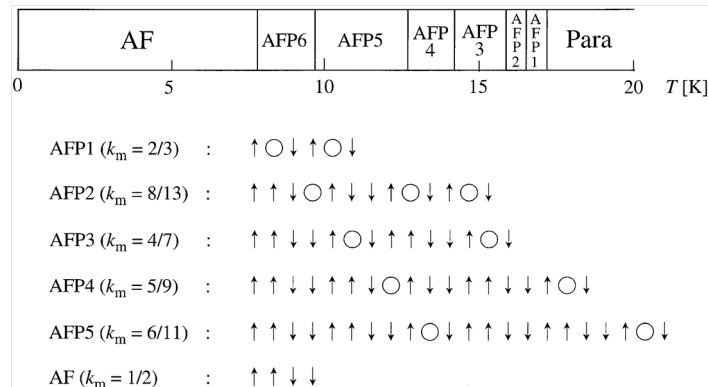


Figure 3.6: Magnetic phase diagram of CeSb at low temperature with no magnetic field and a schematic representation of magnetic structures. Picture taken from ref. [41]

3.4. CeBi magnetic phase diagram

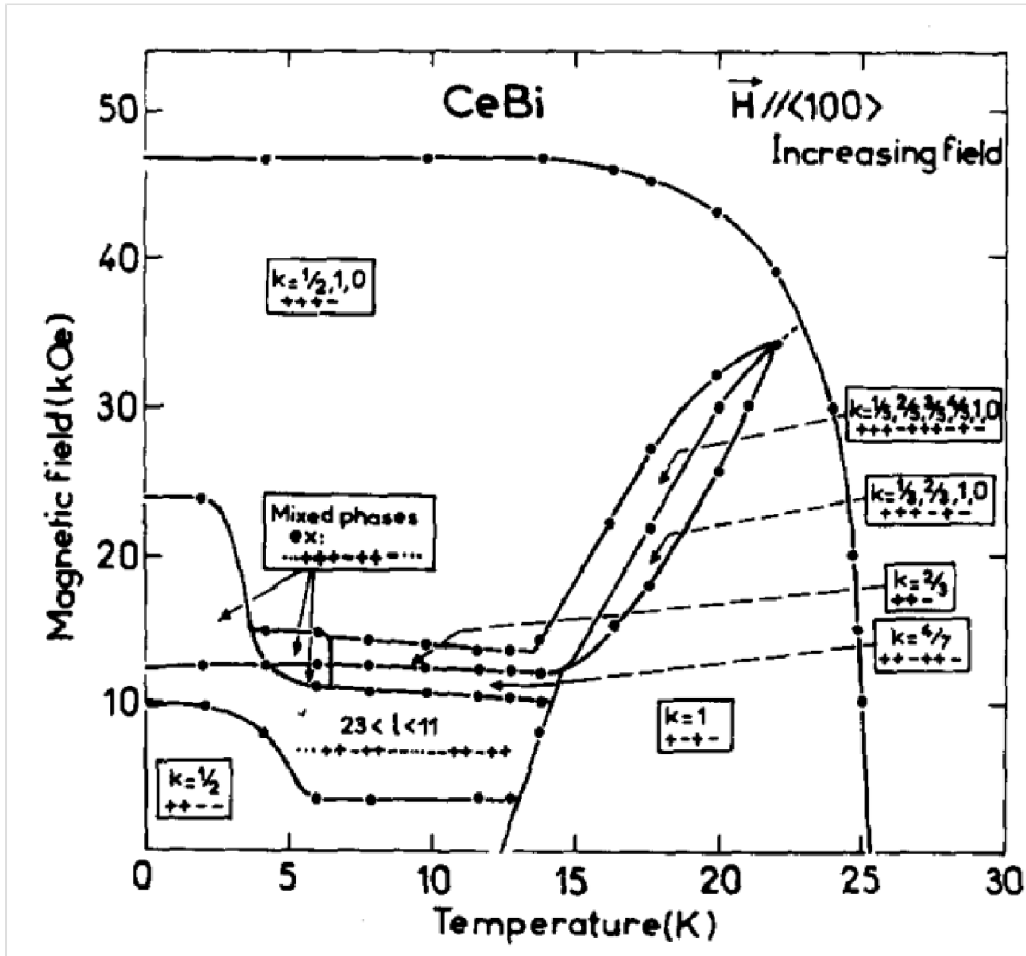


Figure 3.7: Magnetic phase diagram of Cerium Bismuth. Picture taken from ref. [14]

ward the antiferromagnetic type IA phase (+ + - -) takes place, where the ferromagnetic (001) planes are arranged with the moment parallel to the [001] direction [24] [25]. While the crystal field splitting is unusually small, the magnetic anisotropy is very large at low T, the magnetization increases in a step-like manner. Also for this compound, all the obtained informations come from neutron and X-ray diffraction experiments. In Figure 3.7 it's possible to observe three main phases: a type I (+ -), a type IA (+ + -) and a ferrimagnetic (+ + + -) phase. These are not the only ones, in fact instead of observing a direct transition between phases, there are many long range intermediate structures. For example, between the type I (+ -) and the ferri (+ + + -) phases, the following sequences + + + - : + + + - : + - and + + + - : + - are present with increasing temperature. A similar behavior occurs also at low temperature. The understanding of this phase diagram implies that the ferromagnetic interactions within the (001) planes, are one order of magnitude larger than the antiferromagnetic couplings between planes. This coupling is the one that arises from the mixing between $4f - \Gamma_8$ states with the 5p-holes of the valence band.

CHAPTER 4

Phonon measurement on Cerium Bismuth

The last two chapters are dedicated to the main experimental results related on CeBi and CeSb analysis. First of all a brief introduction on the samples and their synthesis is necessary. Both samples, CeBi and CeSb single crystal, have been made by Oscar Vogt in 1983 at the ETH in Zurich, Switzerland, using the Bridgman technique, which is one of the oldest techniques used for growing crystals. The crystal grows from the melting state: the principle of this technique is to translate pieces of the melting from the hot zone to the cold zone of the furnace to obtain a directional solidification. At first the polycrystalline material needs to be melted completely in the hot zone and be brought into contact with a "seed". This seed is a piece of single crystal and ensure a single-crystal growth along certain crystallographic orientation. Part of the seed will be re-melted after the contact with the melt, this provide a fresh interface for the crystal growth.

In particular this part deals with the analysis of the dispersion curves of Cerium Bismuth. After some details about the Inelastic X-ray scattering setup, which involved a series of operations for crystal alignment, the experiment is presented. The first part is dedicated to the measurement and study of the dispersion curves, with the extraction of some important parameters. Then the Born-von Karman theory is presented, in order to understand how theory describes lattice dynamics in the specific case of a rock-salt structure. In the end the *ab-initio* approach, which is based on the study of the electron state problem, is discussed.

4.1 IXS setup

In this work, all the Inelastic X-ray scattering measurements were performed at the beamline ID28 at the ESRF. The first thing that needs to be chosen is the energy of the incoming beam; for these experiments Si (9 9 9) reflection order of the backscattering monochromator was

Chapter 4. Phonon measurement on Cerium Bismuth

used, this provide an incoming energy $E_i = 17.794 \text{ keV}$ ($\lambda_i = 0.6869 \text{ \AA}$) with an energy resolution $\Delta E_i = 3.0 \text{ meV}$. In our configuration the multilayer setup has been installed: this is a focusing system situated in the experimental hutch, used in order to obtain a focusing of the horizontal and vertical directions of the beam. The beam size reached is $30 \times 60 \mu\text{m}$.

As already said, the machine is equipped with nine different analyzers, but for *crystalline materials* using an array is more complicated and it is generally possible to put only one analyzer *precisely* at a specific \mathbf{Q} point. In our measurement, only analyzer number 2 is the one aligned with the 2θ angle, for the momentum transfer of interest.

For this experiment we considered the typical phonon energies of CeBi and we decided to measure with an energy scan range of $\pm 20 \text{ meV}$, corresponding to a temperature scan of the monochromator of $T_0 \pm 0.225 \text{ K}$. For the data acquisition the area of each scan was covered with 60 points and a counting time of 40 seconds per point.

4.2 Dispersion curves of CeBi

During the first run the main goal is to measure CeBi sample with the IXS technique in order to obtain information on the dispersion curves, and then to compare the data with theoretical calculations.

Before starting with the real measurement, we had to prepare the experiment, which basically concerns the sample alignment. The CeBi crystal was mounted on the goniometer head, in order to be able to set up the desired configuration. Then, in order to avoid changing in the sample position during rotation, the sample should be placed in the center of rotation of the diffractometer, in this way its is impossible for the sample to precess with respect to the incident X-ray beam. Next step is to try to understand how the crystal is oriented, or in which direction the crystal planes are. To get this we used a CCD camera placed, only for this operation, just after the sample. Thanks to this camera, we can scan the reciprocal space, looking for diffraction spots. In fact, we need to know the position of two reflections in order to construct the \mathbf{UB} matrix [26]. The orientation matrix, \mathbf{UB} , describes the sample orientation with respect to the diffractometers angles. Given \mathbf{UB} , it is possible to calculate the diffractometers angles ($2\theta, \theta, \chi, \phi$) necessary to rotate the sample in order to scatter for the interested \mathbf{Q} point, indexed by (H, K, L), into the diffraction position. The matrix \mathbf{B} transform the given (H, K, L) into an orthonormal coordinate system fixed in the crystal. The matrix \mathbf{U} is the rotation matrix that rotates the crystal's reference frame into the spectrometer's.

The first step in constructing an appropriate orientation matrix is to know the sample crystal lattice parameters $a, b, c, \alpha, \beta, \gamma$. The second step is to specify the sets of values of the diffractometer angles ($2\theta, \theta, \chi, \phi$) where you find the Bragg peak and define which Bragg reflection should be. Doing this for two points in the software, it will evaluate the total matrix and it will be able to rotate the diffractometer and the sample at the correct values for every \mathbf{Q} point.

For our analysis we select a particular crystal orientation, see Figure 4.2, where the scattering plane in formed by $\langle 100 \rangle$ and $\langle 011 \rangle$ directions. This choice is useful because, with only one sample orientation it is possible to perform scans in all the three polarization directions. Unfortunately it is not possible to obtain all the dispersion curves with only one orientation; in this case with the first setup it is impossible to measure TA and TO in the $\langle 100 \rangle$ direction and LA and LO in the $\langle 011 \rangle$ direction. So we set a second crystal orientation with

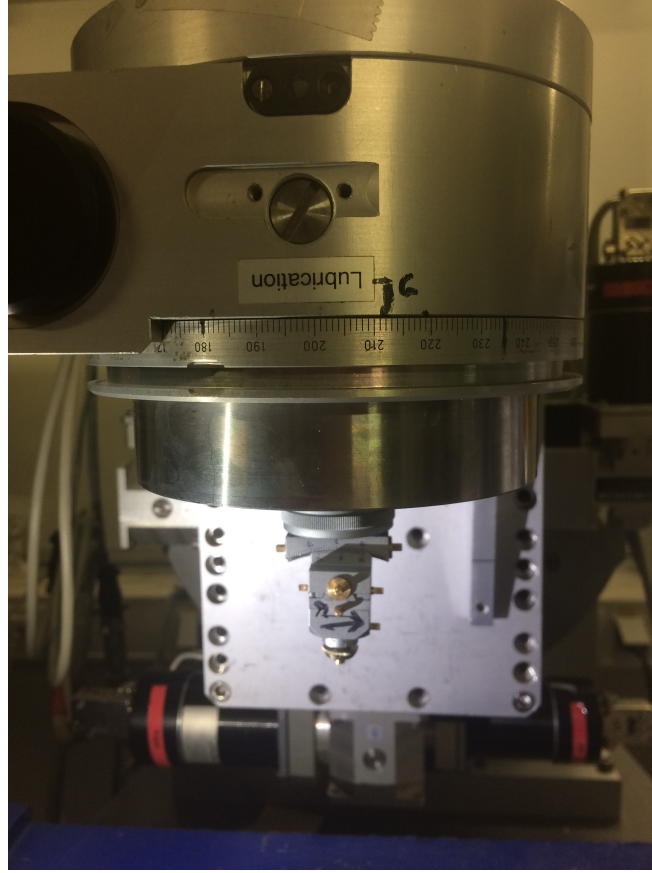


Figure 4.1: Photograph of the sample mounted on the goniometer head in the final geometry.

the scattering plane defined by $\langle 100 \rangle$ and $\langle 0-1-1 \rangle$ in order to have access to these missing directions, Figure 4.3.

At this point, everything is ready to start the measurement, and we decided which paths we have to follow in the reciprocal space. We know that in the expression of the one-phonon structure factor $F(\mathbf{q}, \mathbf{Q})$, Eq. 2.28, there is a scalar product between $\mathbf{e}(\mathbf{q})$, the phonon polarization, and \mathbf{Q} , this allows particular modes to be chosen in the experiment and it is possible to distinguish transverse from longitudinal lattice vibrations. In addition, thank to the crystallographic analysis developed in Section 3.1, we notice that for an even reflection, so when $h, k, l = \text{even}$, the form factors interfere constructively. This is associated to a in-phase motion of the atoms, and so around these reflections, the acoustic modes are excited. For an odd reflection, instead, there is an out of phase interaction and so an out of phase movement of the atoms, which describes an optical mode. This is an important tool in order to select acoustic or optical vibrations.

During all the experiment we have used data from a previous work done on CeSb, so it was possible to predict more or less the dispersion curves of CeBi. Starting in the center of the Brillouin zone Γ , we measure phonons with polarization along $\langle 100 \rangle$, $\langle 110 \rangle$ and $\langle 111 \rangle$: following the path $\Gamma \rightarrow X$ for $\langle 100 \rangle$ polarization, from $\Gamma \rightarrow K$ for $\langle 110 \rangle$ polarization and from $\Gamma \rightarrow L$ for $\langle 111 \rangle$ polarization, see Figure 4.4.

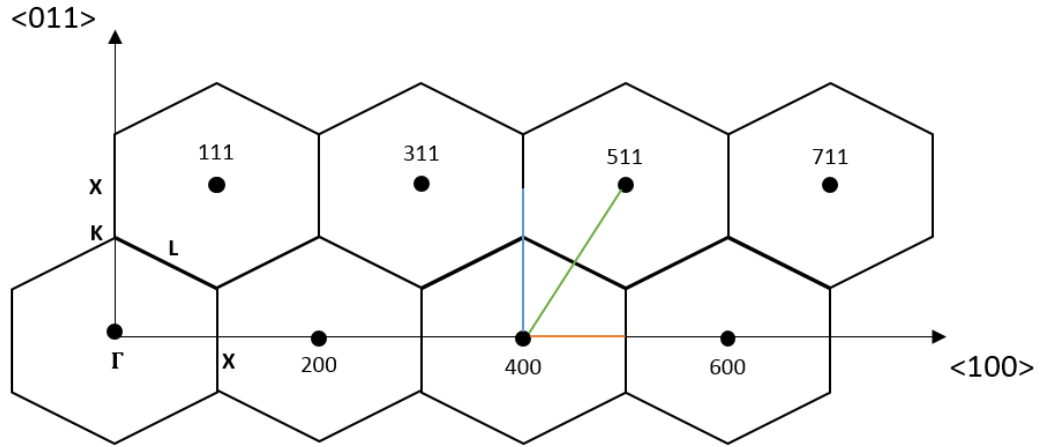


Figure 4.2: Representation of the scattering plane in the IXS experiment. Green, red and blue lines are associated to three different polarization directions, in this case for an acoustic mode

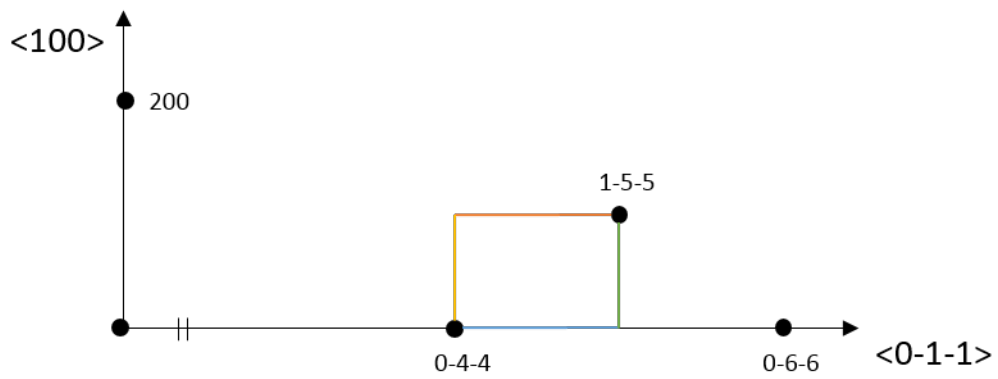


Figure 4.3: Representation of the second crystal orientation. Colored lined are associated to the paths followed in the reciprocal space

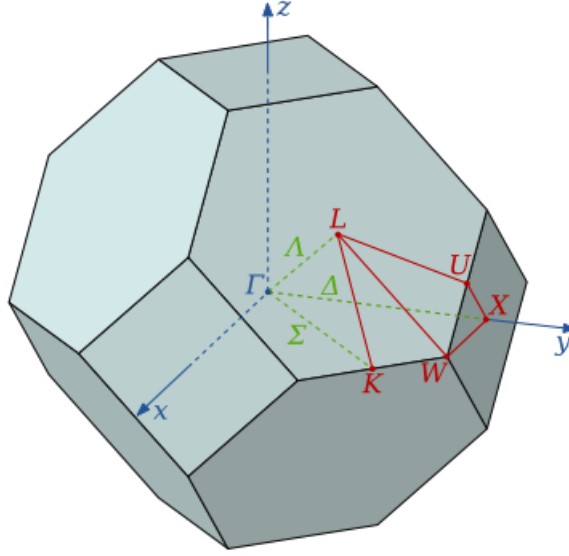


Figure 4.4: First Brillouin zone for the fcc lattice

The measurement proceeds in two steps: first moving the spectrometer 2θ arm (which holds the analyzer array), and the other motors in the specific position, in this way the analyzers will intercept the scattered radiation at the momentum transfer of interest, then scanning the energy of the incident beam while holding the analyzer array energy and position constant. This energy scan is obtained changing the temperature of the main monochromator and so the lattice spacing between atoms. In this way the incoming radiation has different energies while the analyzers continue to select the same wavelength and send it to the detector. The magnitude of the momentum transfer is:

$$|\mathbf{Q}| = (4\pi/\lambda)\sin(2\Theta/2) \quad (4.1)$$

it is determine by the scattering angle, 2Θ , and the incident x-ray wavelength, λ , and there is no coupling between energy transfer and momentum transfer so, in a different way than with a neutron triple axis spectrometer, fixed \mathbf{Q} scans are done without moving the sample or the two-theta arm. The resulting spectrum, intensity vs energy transferred to the sample, $\hbar\omega$, is directly proportional to the dynamic structure factor, $S(\mathbf{Q}, \omega)$.

We expect to have well-defined peaks corresponding to a specific phonon modes at finite energy transfer, no strong peak at zero energy transfer, except for Bragg reflections, and often some diffuse scattering due to sample imperfections. This is not in good agreement with the experimental results, in fact we clearly see that there is always a strong elastic peak at zero energy, this is probably due to the fact that the crystal is not perfect. However the phonon excitation are still visible, see Figure 4.5. Also low-energy phonon modes have higher intensity than high-energy phonon modes, as theory predict, due to both temperature-dependent occupation factors and the fact the high-frequency modes have smaller displacement.

The data analysis mainly consist in two different step:

1. Conversion from a temperature scale, related to che changing in temperature of the main monochromator, to the energy scale. The high quality of the crystal allows to

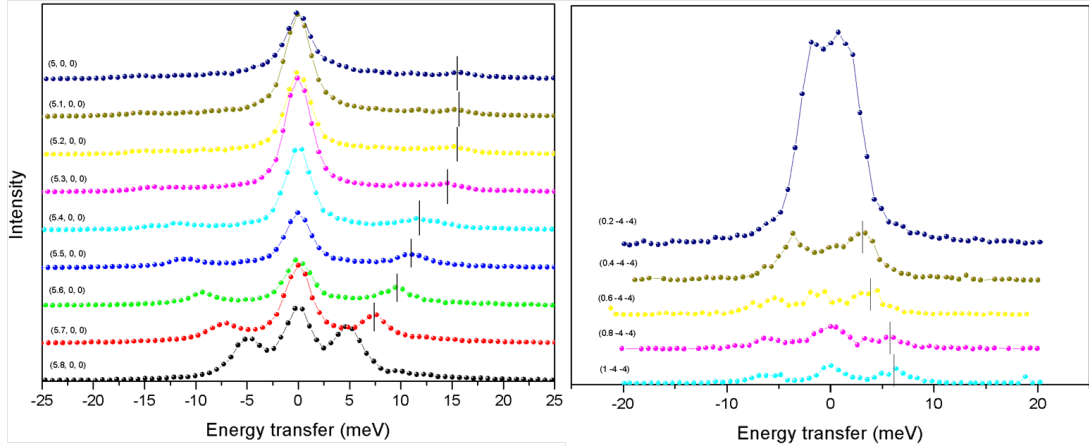


Figure 4.5: Examples of scans acquired for the $\langle 100 \rangle$ direction. In particular it's possible to observe the longitudinal and transverse acoustic phonons for different fixed Q .

connect ΔT to ΔE with an excellent level of confidence, through the expansion coefficient $\alpha(T)$;

2. Fitting of the spectra. Using a specific software developed just for this beamline, fit28, it's possible to obtain the final result. The number of the analyzer, 2 in this case, and its resolution function should be chosen. Another important aspect is to choose with which function we should fit the scan. In this case for the phonons, it is normally used the damper-harmonic oscillator. The result is the values of energy, intensity, width, with their errors of the peak related to every specific excitation.

At the end of the measurement, we are able to construct all the dispersion curves of CeBi, and compare them with the theoretical calculations, provided by Pablo Maldonado from Uppsala University, Sweden. In general we can see a good agreement between experiment and theory, but what is also important is a comparison with the CeSb curves.

It is useful to make this comparison because, the main goal of the all activity, not only of my experience, is to obtain information about dispersion curves of Ce monopnictides, a class of compound including: CeP, CeAs, CeSb, CeBi. So this is only the beginning of the analysis, which also include a study of phonon anomalies at low temperature as we can see in the next chapter.

The phonon dispersion curves of CeBi are represented in Figure 4.6. In this figure, the points indicate the experimental phonon result and the lines are the calculated dispersion curves, with *ab-initio* method. First we can see that the transverse and longitudinal modes branches, TA and LA, in all directions behave normally in the long-wave limit, so near the Γ point. Another important feature is that the LA mode is above the TO mode in $\langle 001 \rangle$ and $\langle 111 \rangle$ directions. In particular this is found to occur between $\mathbf{q} = \frac{2\pi}{a}(0.45, 0.45, 0.45)$ and $\mathbf{q} = \frac{2\pi}{a}(0.5, 0.5, 0.5)$ in $\langle 111 \rangle$ direction and between $\mathbf{q} = \frac{2\pi}{a}(0, 0, 0.7)$ and $\mathbf{q} = \frac{2\pi}{a}(0, 0, 1)$. Interesting features have been found also in the dispersion of the optic branches. In particular, a very common behaviour in the phonon spectrum of CeBi is the inversion of LO and TO in $\langle 001 \rangle$ and $\langle 011 \rangle$ directions. Along these symmetry directions, these branches cross each other one or more times and LO has a clear minimum at $\mathbf{q} = \frac{2\pi}{a}(0, 0, 0.6)$ and at

4.2. Dispersion curves of CeBi

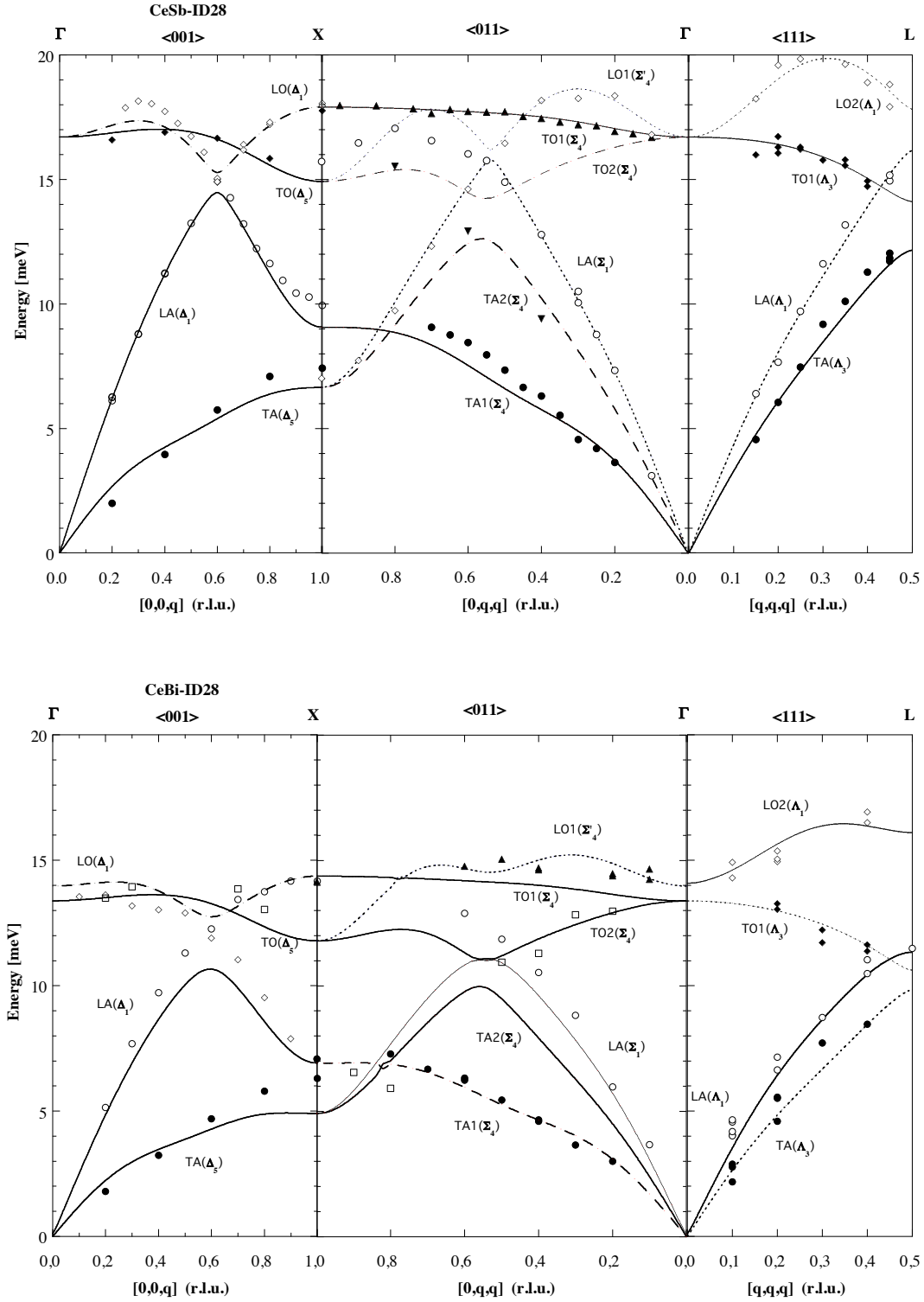


Figure 4.6: Up: *ab initio* results of phonon dispersion curves of CeSb. Different modes are labelled with different types of lines. Dots, filled and empty, are the experimental data. Down: *ab initio* calculations for CeBi also together with the experimental points.

Chapter 4. Phonon measurement on Cerium Bismuth

$$\mathbf{q} = \frac{2\pi}{a}(0, 0.55, 0.55).$$

The phonon dispersion curve of CeSb is very similar to those obtained for CeBi. Acoustic and optic phonon modes have similar patterns. This is because they have the same crystal structure, they belong to the same spatial group and the only difference is in the masses of the atoms. Thus, the frequency differences in the acoustic phonon modes in these materials can be related to the differences in their total masses (M) and lattice constants (a). Also the frequency differences in optical phonon modes can be explained in terms of reduced mass (μ) and lattice constant differences between these materials [27].

Starting from these observations, it is possible to obtain the acoustic and optic frequencies of the CeBi phonon modes, $\nu_{ac}(CeBi)$ and $\nu_{op}(CeBi)$, from the one already calculated for CeSb using the following equations:

$$\nu_{ac}(CeBi) = \sqrt{\frac{M^{CeSb}}{M^{CeBi}} \frac{a^{CeSb}}{a^{CeBi}}} \nu_{ac}(CeSb) \quad (4.2)$$

$$\nu_{op}(CeBi) = \sqrt{\frac{\mu^{CeSb}}{\mu^{CeBi}} \frac{a^{CeSb}}{a^{CeBi}}} \nu_{op}(CeSb) \quad (4.3)$$

The main difference between the dispersion curves is the fact that the ones of CeBi are at low energies with respect to the same of CeSb. This is related to the fact that bismuth, which is just next to lead in the periodic table is an heavier atom than antimony. The result is that in the IXS scans the excitations peaks are very close together and so it is difficult to obtain a good fit. Another problem comes from the scattering geometries. With this configurations it is possible to select transverse and longitudinal modes only for $\langle 100 \rangle$ and $\langle 110 \rangle$ directions. For the $\langle 111 \rangle$ direction we always acquire a mixing between the two modes and so the data analysis is more complex. This is why we have to repeat more than one time scan along some directions.

Finally, the elastic constants for CeBi can also be evaluated from the slopes of the acoustic branches in the phonon dispersion curves [28]. It is well known that a cubic crystal such as the rock-salt structure as only three independent elastic constants: C_{11} , C_{12} and C_{44} .

	C_{11} (GPa)	C_{44} (GPa)	C_{12} (GPa)	Bulk Modulus
Simulations	120.9	16.47	13.63	49.38
Experiment	129.5	15.2	16.7	54.3

Table 4.1: Table with the value of the elastic constants of CeBi evaluated from the simulations and from the calculations.

In Table 4.1 and 4.2 contains the values of the elastic constants evaluated from the simulations and from the experiment. There is more or less a good agreement between the data, the order of magnitude is the same, and the differences maybe a consequence of the approach choose for the calculation. In fact, the value of the sound velocity, which is directly related to the constants, see Appendix A, is obtain simply plotting the value of those experimental points close to the Γ point, and using a linear interpolation in order to obtain the slope of the line. The problem is that it is impossible to have experimental points very close to Γ

4.3. The Force-Constant Matrix

	C_{11} (GPa)	C_{44} (GPa)	C_{12} (GPa)	Bulk Modulus
Simulations	131.6	19.72	14.66	53.64
Experiment	125.7	21.49	16.42	52.84

Table 4.2: Table with the value of the elastic constants of CeSb evaluated from the simulations and from the calculations.

because the elastic peak is too big. This probably change a little the effective value of the sound velocity.

4.3 The Force-Constant Matrix

In order to complete the analysis on the lattice dynamics it is useful to have a brief overview about the theoretical approach to this problem, and how it is possible to simulate the dispersion curves.

Of course there are a lot a references that dealing with this topics, see for example Born and Huang (1954)[29], Maradudin et al. (1971)[30], Willis and Pryor (1975)[9], Ibach and Luth (2009)[31]. Here the approach proposed by Willis and Pryor is used in the following derivation.

Let's suppose to have a cluster of n atoms, and try to evaluate the forces that acts on each atoms in order to construct the equations of motion for the entire system. Then, we will extend this analysis to a crystal lattice.

So now suppose to have this cluster of n atoms, then $3n$ coordinates, expressed in some axial system, are needed to describe the displacements of the atoms from their equilibrium positions. If the symbol κ is used to label an individual atom, we may use a single $3n$ -vector \mathbf{u} , with $3n$ components.

In terms of matrix notation, the \mathbf{u} vector can be seen as a $3n \times 1$ column matrix. Thus

$$\mathbf{u} = \begin{pmatrix} u_1(1) \\ u_2(1) \\ u_3(1) \\ \vdots \\ u_1(n) \\ u_2(n) \\ u_3(n) \end{pmatrix} \quad (4.4)$$

where $u_\alpha(\kappa)$ are the components of $\mathbf{u}(\kappa)$ along the three Cartesian axes α ($\alpha = 1, 2, 3$). Now we can introduce the interatomic forces, which must be function of the atomic displacement. Assuming the validity of the harmonic approximation, the forces are *linear* functions of the displacement. The force on atom κ arising from its interaction with another atom κ' may then be described by

$$\mathbf{F} = -\Phi(\kappa\kappa')\mathbf{u}(\kappa') \quad (4.5)$$

Chapter 4. Phonon measurement on Cerium Bismuth

The equation represents a set of three linear equations expressing the concept that the force exerted on κ in any arbitral direction is proportional to the displacement of κ' in any other arbitrary direction. The quantity $\Phi(\kappa\kappa')$ is 3x3 matrix called *force-constant matrix*

$$\Phi(\kappa\kappa') = \begin{pmatrix} \Phi_{11} & \Phi_{12} & \Phi_{13} \\ \Phi_{21} & \Phi_{22} & \Phi_{23} \\ \Phi_{31} & \Phi_{32} & \Phi_{33} \end{pmatrix} \quad (4.6)$$

where the subscripts refer to axis directions. The element $\Phi_{13}(\kappa\kappa')$, for example, is the force constant acting and atom κ along x -direction when atom κ' is moved in the z -direction.

The force-constant matrix is related to the potential energy of the whole system. If V_0 is the energy of the system *at rest*, so when all the atom are in a fixed position in the space, neglecting all vibrations; it is possible to write the potential energy as a Taylor expansion around V_0 :

$$2V = 2V_0 + \sum_{\kappa\alpha} \left(\frac{\partial V}{\partial u_\alpha(\kappa)} \right)_0 u_\alpha(\kappa) + \sum_{\kappa\alpha} \sum_{\kappa'\alpha'} \left(\frac{\partial^2 V}{\partial u_\alpha(\kappa) \partial u_{\alpha'}(\kappa')} \right)_0 u_\alpha(\kappa) u_{\alpha'}(\kappa') + \dots \quad (4.7)$$

where α, α' refer to the three axes, and the subscript zero indicates that the derivatives are to be evaluated at the equilibrium atomic position. Now, it is possible to simplify this equation, notice that the energy is a minimum when all the atoms are at their equilibrium positions, so all the $3n$ first derivatives are zero:

$$\left(\frac{\partial V}{\partial u_\alpha(\kappa)} \right)_0 = 0 \quad \forall \kappa, \forall \alpha$$

Then, we can introduce two more approximations, that help us in simplifying the problem:

1. we can set the energy for the equilibrium configuration to zero ($V_0 = 0$);
2. from the harmonic approximation, all the terms in the potential energy expansion except those which are quadratic in the displacement, may be ignored.

So the expression can be rewritten as:

$$2V = \sum_{\kappa\alpha} \sum_{\kappa'\alpha'} \left(\frac{\partial^2 V}{\partial u_\alpha(\kappa) \partial u_{\alpha'}(\kappa')} \right)_0 u_\alpha(\kappa) u_{\alpha'}(\kappa') \quad (4.8)$$

Remember that the force acting on atom κ when it is displaced from its equilibrium position is $-\frac{\partial V}{\partial u_\alpha(\kappa)}$, so the interaction of the atom κ with just one of the atoms κ' is:

$$F_\alpha(\kappa) = - \left(\frac{\partial^2 V}{\partial u_\alpha(\kappa) \partial u_{\alpha'}(\kappa')} \right) u_{\alpha'}(\kappa') \quad (4.9)$$

We want to write the equation of motion, so we have to start from the Lagrangian

$$L = E_k - V$$

and then arrive to the Euler-Lagrange equations:

$$\frac{d}{dt} \frac{\partial L}{\partial \dot{u}_\alpha(\kappa)} - \frac{\partial L}{\partial u_\alpha(\kappa)} = 0 \quad (4.10)$$

Replacing the expression for E_k and V , we obtain the equations of motion:

$$m(\kappa) \ddot{\mathbf{u}}(\kappa, t) = - \sum_{\kappa'} \Phi(\kappa\kappa') \mathbf{u}(\kappa', t) \quad (4.11)$$

Which is a set of many second order differential equations. The unknowns are the functions that describes the variations in time of the 3 component $\mathbf{u}_\alpha(\kappa)$.

4.4 Born - von Karman theory

Lattice modes, or collective modes, are modes of vibration of the entire crystalline structure. The classical theory of lattice vibrations is based on the treatment first formulated by Born and von Karman (1912,1913).

There are two important assumptions that are at the base of the theory:

1. the crystal is *finite but unbonded*, an assumption which is also known as the *cyclic boundary condition*. In this way we can neglect entirely the contribution of the surface;
2. in the crystal the vibrations are no stationary modes, but as travelling waves extending through the entire crystal.

So the general expression for the displacement of an atom in the crystal is

$$\mathbf{u}(\kappa l, t) = \mathbf{U}(\kappa|\mathbf{q}) \exp[i(\mathbf{q} \cdot \mathbf{r}(\kappa l) - \omega(\mathbf{q})t + \phi(\kappa|\mathbf{q}))] \quad (4.12)$$

κ labels a particular atom in the unit cell, l labels a unit cell.

What is important now is that the displacement $\mathbf{u}(\kappa l, t)$ of the (κ, l) atom from its equilibrium position $\mathbf{r}(\kappa l)$ depends on the *wave vector* \mathbf{q} . The displacement vector $\mathbf{U}(\kappa|\mathbf{q})$ is related to the maximum amplitude of the atom (κ, l) , due to the travelling wave. $\mathbf{U}(\kappa|\mathbf{q})$ is not dependent on l , this follows from *Bloch's theorem*: for the same atoms in different cells, (κ, l) and (κ, l') , the motions are identical as regard their amplitude and direction and differ only in phase.

In addition, Bloch's theorem introduce an enormous simplification, it allow to restrict the attention to the $3n$ equations of motion of the n atoms in one cell, rather than the $3nN$ equations of motion for all atoms in the crystal. For *longitudinal* waves the atomic displacements are parallel to the propagation direction, i. e. $\mathbf{U}(\kappa|\mathbf{q})$ is along \mathbf{q} , instead for *transverse* waves $\mathbf{U}(\kappa|\mathbf{q})$ is perpendicular to \mathbf{q} .

The frequency ω depends on \mathbf{q} , and this dependence $\omega(\mathbf{q})$ gives the *dispersion relation* for the propagation described by \mathbf{q} . Finally, the phase $\phi(\kappa|\mathbf{q})$ represents the phase of the atom arising from its excitation by the wave of wave vector \mathbf{q} .

4.4.1 Equations of motion

The Born - von Karman theory can now be developed. As we said in the previous section, the equations of motions for the κ th atom in the l th unit cell are:

$$m(\kappa) \ddot{\mathbf{u}}(\kappa, t) = - \sum_{\kappa' l'} \Phi(\kappa l, \kappa' l') \mathbf{u}(\kappa' l', t) \quad (4.13)$$

Chapter 4. Phonon measurement on Cerium Bismuth

and the elements of the force-constant matrix Φ are related to the potential energy V . Substituting equation (4.12) into (4.13), and after the mass-adjustment procedure, leads to the matrix equation:

$$\omega^2 \mathbf{U} = \mathbf{D} \mathbf{U} \quad (4.14)$$

where \mathbf{U} is defined as

$$\mathbf{U} = \mathbf{m}^{-\frac{1}{2}} \mathbf{U}_0 \quad (4.15)$$

and \mathbf{U}_0 is the vector of the displacement vectors $\mathbf{U}(\kappa|\mathbf{q})$:

$$\mathbf{U}_0(\mathbf{q}) = \begin{pmatrix} U_1(1|\mathbf{q}) \\ U_2(1|\mathbf{q}) \\ U_3(1|\mathbf{q}) \\ U_1(2|\mathbf{q}) \\ \vdots \\ U_3(n|\mathbf{q}) \end{pmatrix} \quad (4.16)$$

$\mathbf{D}(\mathbf{q})$ is the $3n \times 3n$ dynamical matrix defined by:

$$\mathbf{D} = \mathbf{m}^{-\frac{1}{2}} \mathbf{D}_0 \mathbf{m}^{-\frac{1}{2}} \quad (4.17)$$

and a general element of this matrix is:

$$D_{\alpha\alpha'}(\kappa\kappa'|\mathbf{q}) = (m(\kappa)m(\kappa'))^{-\frac{1}{2}} \sum_{l'} \Phi_{\alpha\alpha'}(\kappa l, \kappa' l') \exp[i\mathbf{q} \cdot \mathbf{r}(\kappa' l') - \mathbf{r}(\kappa l)] \quad (4.18)$$

This element is obtained by calculating the 3×3 force-constant matrices for the interactions between atom κ in one unit cell, and atom κ' in the same and in all other unit cell l' .

The last exponential term represents the phase factor, which rise from the different positions of the atoms we are considering. Because of the complex factor in the expression, all the elements in the dynamical matrix are complex, unless every atom is a center of symmetry.

But, the \mathbf{D} matrix is *Hermitian* by construction:

$$\mathbf{D} = (\mathbf{D}^*)^T$$

and so, the eigenvalues of Eq. (1.11) are always real, but the eigenvectors can be complex anyway.

The eigenvalues will be labelled with the symbol j ($=1, 2, \dots, 3n$), and each value of j refers to a *branch* of the dispersion relation. So, for each \mathbf{q} -vector fixed in the Brillouin zone, there is a set of $3n$ different frequency of vibration: $\omega_j(\mathbf{q})$, with the corresponding eigenvector $\mathbf{e}(j\mathbf{q})$ giving the pattern of the atomic displacement for the mode ($j\mathbf{q}$). The eigenvector is a column matrix:

$$\mathbf{e}(j\mathbf{q}) = \begin{pmatrix} e_1(1|j\mathbf{q}) \\ e_2(1|j\mathbf{q}) \\ e_3(1|j\mathbf{q}) \\ e_1(2|j\mathbf{q}) \\ \vdots \\ e_3(n|j\mathbf{q}) \end{pmatrix} \quad (4.19)$$

4.5. Lattice vibrations of solids with *fcc* crystal structure

where the general element $e_\alpha(\kappa|j\mathbf{q})$ is the displacement in the α -direction, i.e. the polarization, of the κ atom, which is vibrating in the mode ($j\mathbf{q}$). So, it's possible to rewrite the set of equations of motions as

$$\omega_j^2(\mathbf{q})\mathbf{e}(j\mathbf{q}) = \mathbf{D}(\mathbf{q})\mathbf{e}(j\mathbf{q}) \quad (4.20)$$

and the relation between the polarization and the absolute magnitude of the atomic displacement in the mode ($j\mathbf{q}$) is

$$\mathbf{U}_0 = \mathbf{m}^{-\frac{1}{2}}\mathbf{U}(j\mathbf{q}) = \mathbf{m}^{-\frac{1}{2}}|A(j\mathbf{q})|\mathbf{e}(j\mathbf{q}) \quad (4.21)$$

where the scalar quantity is $|A(j\mathbf{q})|$ is the amplitude of the excitation.

Finally, the general solution for the displacement $\mathbf{u}(\kappa l, t)$ is given by the superposition of the displacement from the travelling waves representing all the possible modes of vibrations.

$$\mathbf{u}(\kappa l, t) = (m(\kappa))^{-\frac{1}{2}} \sum_{j\mathbf{q}} |A(j\mathbf{q})|\mathbf{e}(j\mathbf{q}) \exp[i(\mathbf{q} \cdot \mathbf{r}(\kappa l) - \omega_j(\mathbf{q})t)] \quad (4.22)$$

To end this theoretical introduction, we can very briefly highlight the main results:

- after solving the problem, from the square root of the eigenvalues, we get the vibrational frequency of each mode;
- the eigenvectors associated to each eigenvalue, gives the pattern of the entire atomic motion for each mode;
- the dynamical matrix $\mathbf{D}(\mathbf{q})$ contains all the informations of the lattice dynamics.

4.5 Lattice vibrations of solids with *fcc* crystal structure

The main features of the Born-von Karman treatment is the description of the modes of vibration as travelling. The rest of the analysis simply involves the setting up of the force constant matrices and the dynamical matrix \mathbf{D} ; the solutions of the equations of motion are then presented as the eigenvalues and eigenvectors of \mathbf{D} .

In this section an application of the model to an *fcc* crystal structure is presented, first to a general crystal with only one atom in the primitive cell and then the specific case regarding the materials than are studying on this work: CeSb and CeBi, which crystallize in a rock-salt structure.

The first step is to define the correct form of the force-constant matrices, which are modify by symmetry restrictions. There are two main categories of symmetry restrictions: in the first one are the general restrictions imposed by the periodicity of the crystal, the second one covers the special restrictions imposed by the particular crystal structure, in this case the FCC. As example of a special symmetry restriction, let's consider any orthogonal matrix \mathbf{P} that describe a rotation which moves the crystal into itself. The relation

$$\mathbf{P}^T \Phi \mathbf{P} = \Phi \quad (4.23)$$

describes the invariance of the matrix elements to the rotation \mathbf{P} . In this way it is possible to define the force-constant matrices for the twelve nearest neighbours in the structure, where the first atom is considered in position $\mathbf{0}$, see Table 4.3.

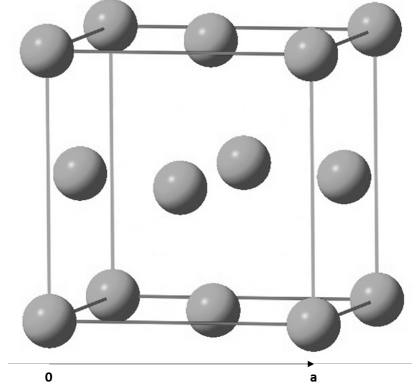


Figure 4.7: fcc structure

Nearest neighbour at	$-\Phi$ matrix
$\pm \frac{a}{2}(1, 1, 0)$	$\begin{pmatrix} \alpha & \gamma & 0 \\ \gamma & \alpha & 0 \\ 0 & 0 & \beta \end{pmatrix}$
$\pm \frac{a}{2}(-1, 1, 0)$	$\begin{pmatrix} \alpha & -\gamma & 0 \\ -\gamma & \alpha & 0 \\ 0 & 0 & \beta \end{pmatrix}$
$\pm \frac{a}{2}(1, 0, 1)$	$\begin{pmatrix} \alpha & 0 & \gamma \\ 0 & \beta & 0 \\ \gamma & 0 & \alpha \end{pmatrix}$
$\pm \frac{a}{2}(-1, 0, 1)$	$\begin{pmatrix} \alpha & 0 & -\gamma \\ 0 & \beta & 0 \\ -\gamma & 0 & \alpha \end{pmatrix}$
$\pm \frac{a}{2}(0, 1, 1)$	$\begin{pmatrix} \beta & 0 & 0 \\ 0 & \alpha & \gamma \\ 0 & \gamma & \alpha \end{pmatrix}$
$\pm \frac{a}{2}(0, -1, 1)$	$\begin{pmatrix} \beta & 0 & 0 \\ 0 & \alpha & -\gamma \\ 0 & -\gamma & \alpha \end{pmatrix}$

Table 4.3: General force-constant matrices for the twelve nearest neighbours in the f.c.c. structure

Now it is possible to write down the elements of the dynamical matrix \mathbf{D}_0 , without the mass adjustment, by summing all the twelve interactions and including the self-term. Each term in the summation is a product between the force-constant matrix for that interaction multiply by the exponential that depends on the positions \mathbf{r} and \mathbf{r}' . For the symmetry of the

4.5. Lattice vibrations of solids with fcc crystal structure

system the force-constant matrix is the same for couples of atoms, for example the pair of nearest neighbours at $\pm a/2(1, 1, 0)$ the contribution is

$$\begin{aligned} & - \begin{pmatrix} \alpha & \gamma & 0 \\ \gamma & \alpha & 0 \\ 0 & 0 & \beta \end{pmatrix} \left(\exp \left[i\mathbf{q} \cdot \frac{a}{2}(1, 1, 0) \right] + \exp \left[-i\mathbf{q} \cdot \frac{a}{2}(1, 1, 0) \right] \right) \\ & = -2\cos \left(\frac{aq_1}{2} + \frac{aq_2}{2} \right) \begin{pmatrix} \alpha & \gamma & 0 \\ \gamma & \alpha & 0 \\ 0 & 0 & \beta \end{pmatrix} \end{aligned}$$

where q_1, q_2, q_3 are the components of the wave vector \mathbf{q} along the cubic crystal axes. Including also the contributions of the remaining pairs the \mathbf{D}_0 matrix becomes

$$\mathbf{D}_0 = \begin{pmatrix} D_{11} & D_{12} & D_{13} \\ D_{21} & D_{22} & D_{23} \\ D_{31} & D_{32} & D_{33} \end{pmatrix}$$

the first term, D_{11} is

$$D_{11} = 4\alpha \left[2 - \cos \frac{aq_1}{2} \left(\cos \frac{aq_2}{2} + \cos \frac{aq_3}{2} \right) \right] + 4\beta \left[1 - \cos \frac{aq_2}{2} \cos \frac{aq_3}{2} \right] \quad (4.24)$$

with similar expressions for D_{22} and D_{33} . The off-diagonal terms are

$$\begin{aligned} D_{12} = D_{21} &= 4\gamma \sin \frac{aq_1}{2} \sin \frac{aq_2}{2} \\ D_{13} = D_{31} &= 4\gamma \sin \frac{aq_1}{2} \sin \frac{aq_3}{2} \\ D_{23} = D_{32} &= 4\gamma \sin \frac{aq_2}{2} \sin \frac{aq_3}{2} \end{aligned} \quad (4.25)$$

Now we have all the knowledge on the dynamical matrix and it is possible to obtain informations on the dispersion relations. Consider the first Brillouin zone of the face-centered cubic lattice and take, as an example, the [100] direction with $\mathbf{q} = \frac{2\pi}{a}(\zeta, 0, 0)$, where ζ goes from zero at the Γ point up to one at X point. Only q_1 is different from zero in this case and the final dynamical matrix, with the mass adjustment, is

$$\mathbf{D} = \frac{4}{m} (1 - \cos \pi \zeta) \begin{pmatrix} 2\alpha & 0 & 0 \\ 0 & \alpha + \beta & 0 \\ 0 & 0 & \alpha + \beta \end{pmatrix} \quad (4.26)$$

It is possible to solve immediately the eigenvalue problem for this matrix, because it's diagonal so the eigenvalues are:

$$\begin{aligned} \omega_1^2 &= \frac{8\alpha}{m} (1 - \cos \pi \zeta) \\ \omega_2^2 = \omega_3^2 &= \frac{4}{m} (\alpha + \beta) (1 - \cos \pi \zeta) \end{aligned}$$

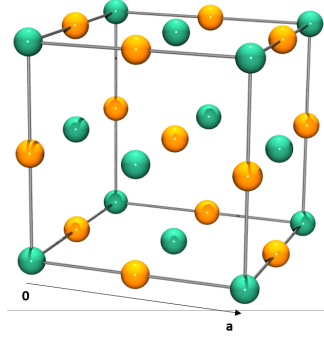


Figure 4.8: Rock-salt structure

and the corresponding eigenvectors are

$$\mathbf{e}(1) = \begin{pmatrix} 1 \\ 0 \\ 0 \end{pmatrix} \quad \mathbf{e}(2) = \begin{pmatrix} 0 \\ 1 \\ 0 \end{pmatrix} \quad \mathbf{e}(3) = \begin{pmatrix} 0 \\ 0 \\ 1 \end{pmatrix}$$

In conclusion, it is clear that for this direction there are two branches that are degenerate, which are associate to the transverse mode, where the atoms oscillate in a direction perpendicular to the propagation of the wave, and one longitudinal branch, with movements in the same direction of the wave. Substituting other values of \mathbf{q} in the dynamical matrix, for example for the [110] and [111] polarization direction, it is possible to obtain a complete scheme of the dispersion curves.

4.5.1 Application on the CeSb and CeBi case

Cerium Antimony and Cerium Bismuth crystallize in a rock-salt structure, which is the same structure of NaCl. This structure can be seen as an *fcc* with two atoms in the primitive cell, and so is characterize to have three acoustic and three optic branches, and the corresponding frequencies are calculated using the same procedure as for the *fcc*. Again, in order to simplify the problem, the assumption is to consider nearest-neighbour interactions only. From Figure 4.8 it is possible to observe that each atom has six nearest-neighbours along the $\langle 100 \rangle$ directions. This is the so called *octahedral geometry*. Also here, in order to evaluate the force-constant matrices it is possible to use the symmetry of the system and obtain the result reported in the Table 4.4.

The dynamical matrix now is a 6x6 Hermitian matrix which may be partitioned in four 3x3 sub-matrices:

$$\mathbf{D}_0 = \begin{pmatrix} \mathbf{D}(11) & \mathbf{D}(12) \\ (\mathbf{D}^*(12))^T & \mathbf{D}(22) \end{pmatrix} \quad (4.27)$$

where 1,2 denotes the two different atoms in this system and $(\mathbf{D}^*(12))^T$ is the complex transpose of $\mathbf{D}(12)$. $\mathbf{D}(11)$ involves forces between atoms of the same type 1, $\mathbf{D}(22)$ forces between atoms of type 2 and $\mathbf{D}(12)$ forces between atom 1 and 2.

The evaluation of these matrices follows the same procedure as before: each term in the sum is the product of the force-constant matrix for the specific interaction multiply by the

4.6. The *ab-initio* approach to phonons

Nearest neighbour at	$-\Phi$ matrix
$\pm \frac{a}{2}(1, 0, 0)$	$\begin{pmatrix} \alpha & 0 & 0 \\ 0 & \beta & 0 \\ 0 & 0 & \beta \end{pmatrix}$
$\pm \frac{a}{2}(0, 1, 0)$	$\begin{pmatrix} \beta & 0 & 0 \\ 0 & \alpha & 0 \\ 0 & 0 & \beta \end{pmatrix}$
$\pm \frac{a}{2}(0, 0, 1)$	$\begin{pmatrix} \beta & 0 & 0 \\ 0 & \beta & 0 \\ 0 & 0 & \alpha \end{pmatrix}$

Table 4.4: General force-constant matrices for the six nearest-neighbours in the rock-salt structure

exponential which depends on the position of the atoms. For example, for the matrix $\mathbf{D}(12)$ the result is

$$\mathbf{D}(12) = -2 \begin{pmatrix} \alpha & 0 & 0 \\ 0 & \beta & 0 \\ 0 & 0 & \beta \end{pmatrix} \cos\left(\frac{aq_1}{2}\right) - 2 \begin{pmatrix} \beta & 0 & 0 \\ 0 & \alpha & 0 \\ 0 & 0 & \beta \end{pmatrix} \cos\left(\frac{aq_2}{2}\right) - 2 \begin{pmatrix} \beta & 0 & 0 \\ 0 & \beta & 0 \\ 0 & 0 & \alpha \end{pmatrix} \cos\left(\frac{aq_3}{2}\right) \quad (4.28)$$

Here is important to note that $\mathbf{D}(12)$ is real and symmetric so $(\mathbf{D}^*(12))^T$ is the same as $\mathbf{D}(12)$. The fact that this matrix has a symmetric form follows from the existence of a centre of symmetry at each atomic site in the rock-salt structure.

Regarding $\mathbf{D}(11)$ and $\mathbf{D}(22)$ the calculation is very simple. From Figure 4.8 it is clear that each atom has as nearest-neighbours only atoms of the other type, and because only nearest-neighbours interaction are considered there are no forces between distinct atoms of the same type. The matrices contain only the self-interaction term

$$\mathbf{D}(11) = \mathbf{D}(22) = 2 \begin{pmatrix} \alpha + 2\beta & 0 & 0 \\ 0 & \alpha + 2\beta & 0 \\ 0 & 0 & \alpha + 2\beta \end{pmatrix} \quad (4.29)$$

So now we have a complete description of the dynamical matrix and it is possible to obtain all the information about the vibrations. The eigenvalues of the matrix give the six frequencies of the modes of vibrations with a particular wave vector \mathbf{q} , and the eigenvectors give the patterns of displacement of the atoms in these modes.

4.6 The *ab-initio* approach to phonons

In the previous section, an application of the Born-von Karman model is presented, which is conceptually a simple "ball and spring" model where you define directly the forces acting

Chapter 4. Phonon measurement on Cerium Bismuth

on different atoms, starting from user-input parameters. A different approach to the calculation of lattice dynamics is the evaluation of the electronic structure of the system, where the forces on the atoms are the result of changes in electronic structure and system energy when atoms are displaced. In order to have a complete overview of the approach, there are a lot of articles that deals with this problem, see for example Baroni et al. (2001) [32], Alfè (2009) [33], Giannozzi et al. (2009) [34], Gonze et al. (2009) [35] and Souvatzis et al. (2009) [36]. The main goal of these type of calculations is to compute the second derivative of the total energy for a given system, and then compute the force constant matrix. The total energy of the system can be obtained by an electronic structure calculation using density functional theory. We start with the *adiabatic approximation* (Born and Oppenheimer, 1927) which allows to decoupling the electronic problem and the nuclear problem. Within this approximation, the lattice dynamical properties of a system are determined by the eigenvalues ξ and the eigenfunction Φ of the Schrödinger equation:

$$\left(- \sum_I \frac{\hbar^2}{2M_I} \frac{\partial^2}{\partial \mathbf{R}_I^2} + E(\mathbf{R}) \right) \Phi(\mathbf{R}) = \xi \Phi(\mathbf{R}) \quad (4.30)$$

where \mathbf{R}_I is the coordinate of the I th nucleus, M_I its mass, \mathbf{R} the set of all nuclear coordinates and $E(\mathbf{R})$ is the ground state energy of a system of interacting electrons moving in the field of fixe nuclei, and can be calculated because it is the eigenvalue of the electronic problem with an Hamiltonian that depends on the electronic variables and parametrically upon \mathbf{R} . Let's go back to the nuclear problem, the equilibrium geometry of the system is given by the condition that the forces acting on individual nuclei vanish:

$$\mathbf{F}_I = - \frac{\partial E(\mathbf{R})}{\partial \mathbf{R}_I} = 0 \quad (4.31)$$

So the calculation of the equilibrium geometry and of the vibrational properties of the system is related to the evaluation of the first and second derivative of the $E(\mathbf{R})$. The basic tool for accomplishing the goal, is the *Hellmann-Feynman theorem* which states that the fist derivative of the eigenvalues of a Hamiltonian, H_λ , that depends on the parameter λ , is given by the expectation value of the derivative of the Hamiltonian:

$$\frac{\partial E_\lambda}{\partial \lambda} = \left\langle \frac{\partial H_\lambda}{\partial \lambda} \right\rangle \Psi_\lambda \quad (4.32)$$

where Ψ_λ is the eigenfunction of H_λ corresponding to the E_λ eigenvalue: $H_\lambda \Psi_\lambda = E_\lambda \Psi_\lambda$. The force acting on the I th nucleus in the electronic ground state is thus:

$$\mathbf{F}_I = - \frac{\partial E(\mathbf{R})}{\partial \mathbf{R}_I} = - \left\langle \Psi(\mathbf{R}) \left| \frac{\partial H(\mathbf{R})}{\partial \mathbf{R}_I} \right| \Psi(\mathbf{R}) \right\rangle \quad (4.33)$$

where $\Psi(\mathbf{R})$ and $H(\mathbf{R})$ are the ground-state wave function and the Hamiltonian of the electronic problem. After the partial derivation only two terms remain in the Hamiltonian, the electron-ion interaction and the ion-ion interaction, so the Hellmann-Feynman theorem states that

$$\mathbf{F}_I = - \int n_{\mathbf{R}}(\mathbf{r}) \frac{\partial V_{\mathbf{R}}(\mathbf{r})}{\partial \mathbf{R}_I} d\mathbf{r} - \frac{\partial E_N(\mathbf{R})}{\partial \mathbf{R}_I} \quad (4.34)$$

4.6. The *ab-initio* approach to phonons

where $V_{\mathbf{R}}(\mathbf{r})$ labels the electron-ion interaction, $E_N(\mathbf{R})$ labels the ion-ion interaction and $n_{\mathbf{R}}(\mathbf{r})$ is the ground-state electron charge density corresponding to the nuclear configuration \mathbf{R} .

The second derivative of the energy, which is equal to the force constant, is obtained by differentiating the Hellmann-Feynman forces with respect to the nuclear coordinates,

$$\frac{\partial^2 E(\mathbf{R})}{\partial \mathbf{R}_I \partial \mathbf{R}_J} = -\frac{\partial \mathbf{F}_I}{\partial \mathbf{R}_J} = \int \frac{\partial n_{\mathbf{R}}(\mathbf{r})}{\partial \mathbf{R}_J} \frac{\partial V_{\mathbf{R}}(\mathbf{r})}{\partial \mathbf{R}_I} d\mathbf{r} + \int n_{\mathbf{R}}(\mathbf{r}) \frac{\partial^2 V_{\mathbf{R}}(\mathbf{r})}{\partial \mathbf{R}_I \partial \mathbf{R}_J} d\mathbf{r} + \frac{\partial^2 E_N(\mathbf{R})}{\partial \mathbf{R}_I \partial \mathbf{R}_J} \quad (4.35)$$

From this equation, we can see that for this calculation we have to know the ground-state electron charge density $n_{\mathbf{R}}(\mathbf{r})$ and also its linear response to a distortion of the nuclear geometry: $\frac{\partial n_{\mathbf{R}}(\mathbf{r})}{\partial \mathbf{R}_I}$.

The final result is that the energy of the electron system is a functional which depends on the electron charge density, and the goal is to find the proper function $n(\mathbf{r})$ in order to minimize the functional. This is the basis of the *density functional theory*, DFT. It allows an enormous conceptual simplification of the quantum mechanical problem of searching for the ground-state properties of a system of interacting electrons, substituting the traditional description based on the wave function, with a much more tractable description in terms of the charge density, which depends on only three variables.

In general, there are two different way in which is possible to study the charge density and its derivative:

- "Direct" methods, rely on calculating changes in the energy, and resulting forces on atoms, when atoms are explicitly displaced from the equilibrium positions. These can be done considering displacements of one atom at a time (small displacement method) or choosing specific phonon displacement patterns as governed by symmetry conditions.
- An alternative to the direct method is density functional perturbation theory (DFPT) originally described using a plane wave approach (Baroni et al., 2001). It builds a perturbation calculation for the phonons into the code, and can be applied at arbitrary momentum transfers.

CHAPTER 5

Phonon anomalies in Cerium Antimony

As already said, this last chapter is dedicated to the low-temperature study of phonon anomalies in the antiferromagnetic phase of Cerium Antimony. This analysis follows two different approaches: the first one is presented in Section 5.1 and deals with a Diffuse Scattering experiment, maybe the best technique for the investigation of anomalies or defects in crystals. The second one, in Section 5.2, is an IXS experiment looking for the same anomalies with the acquisition of elastic and inelastic scans. Later, there is an introduction to the data analysis, with the presentation of a possible model that describes the observed intensity pattern.

5.1 Diffuse Scattering Experiment

TDS is another probe of atomic dynamics: momentum resolved but energy-integrated measurements generally show structure due to the momentum dependence of phonon polarization vectors and energies. With this technique it is possible to obtain classical information about the diffraction pattern together with the diffuse scattering signal, which mainly contain information about the lattice vibrations of the system, in terms of phonon intensities. TDS is probably most useful as a complementary technique to IXS, it can be used to quickly investigate large parts of momentum space. This type of experiment is probably the most useful way in order to obtain information about the anomalies in the CeSb sample.

In this case the side station of the Beamline ID28 was used. The preparation phase of the experiment is much faster with respect to the IXS one, because the principle of this acquisition is different. The IXS scan is an energy scan obtained at a particular and fixed \mathbf{Q} and in order to do this a perfect knowing of the sample orientation is necessary, which is obtained with the \mathbf{UB} matrix. On the other side is different because here using an area detector it is possible to collect all the radiation emitted by the sample, the problem is simply to align the sample

Chapter 5. Phonon anomalies in Cerium Antimony

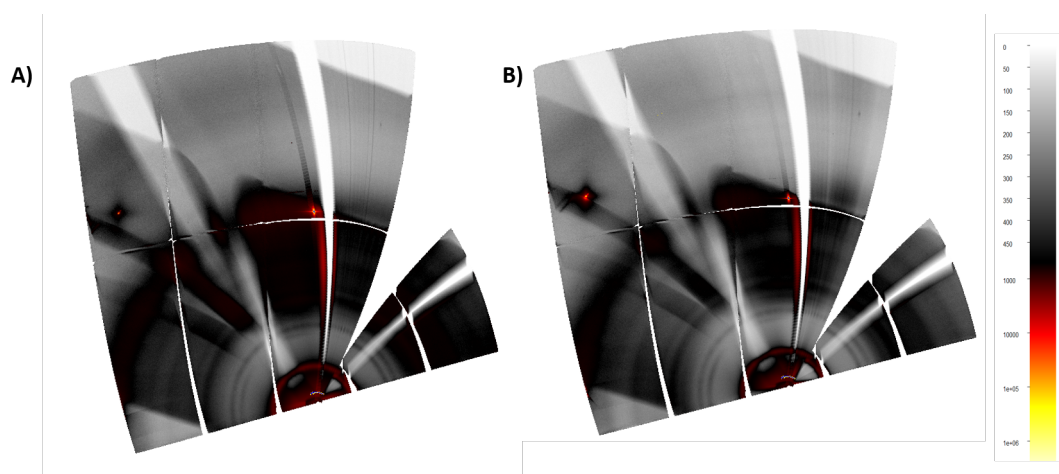


Figure 5.1: Diffuse Scattering acquisition at different temperature: A) 12K B) 13K

with respect to the beam. So the only manual action is to place the sample on the appropriate sample-holder, which is connected to a displex, then it must be centered with respect to the beam. The problem of the center of rotation is quickly solved as the beam is already in the center of rotation of the gonihead, then, once the sample is hit by the beam, it will be also in the center of rotation. Thanks to a diode it is possible to fix the position in the xy plane, the horizontal plane, and the z position using a microscope. Now everything is ready and it is possible to define the acquisition parameters: exposure time, rotation velocity and so on. We choose the step $\Delta\phi = 0.1^\circ$ and the exposure time is 0.5 seconds. The normal rotation is of 360 degree, by the way, we used a cryostat for the low temperature measurement. It affects the visibility and the movement, for this reason we have a range of 170 degree.

We measured the sample at 300K, 100K, 60K, 20K and 12K and each time its position was checked after a temperature stabilization, then the real acquisition starts. This low-temperature displex has a base temperature of 12K so the goal of the experiment is to observe peaks in the range 12-16K, corresponds to different magnetic phases. Each run start with a rotation with respect to the vertical axes of the sample, together with the displex. When it reach the correct position, the acquisition begin and a total number of a 1750 images are acquired. During this process a collimator and a beam stop are fundamental, the first one is useful in order to focus the beam on the sample position and the second is necessary to stop the direct beam that pass through the sample. The result is a series of frame collected by the detector for each angle step where it is possible to observe the different spots corresponding to the Bragg reflections.

After the experiment, data treatment consist in running reconstructions exploiting the data acquired, and the final result are pictures representing the intensity distributions across high symmetry planes in the reciprocal space. The software *CrysAlis^{Pro}* has been used in order to realize these reconstruction. This software is provided by Agilent and has a very simple user interface. If we want to reconstruct the reciprocal space the first thing to do is to find the correct orientation of the sample and its axes, so the **UB** matrix. We have to add all the crystallographic parameters: crystal structure, space group, lattice parameter and the experimental parameters, related to the geometry used, the energy of the x-ray radiation and so on.

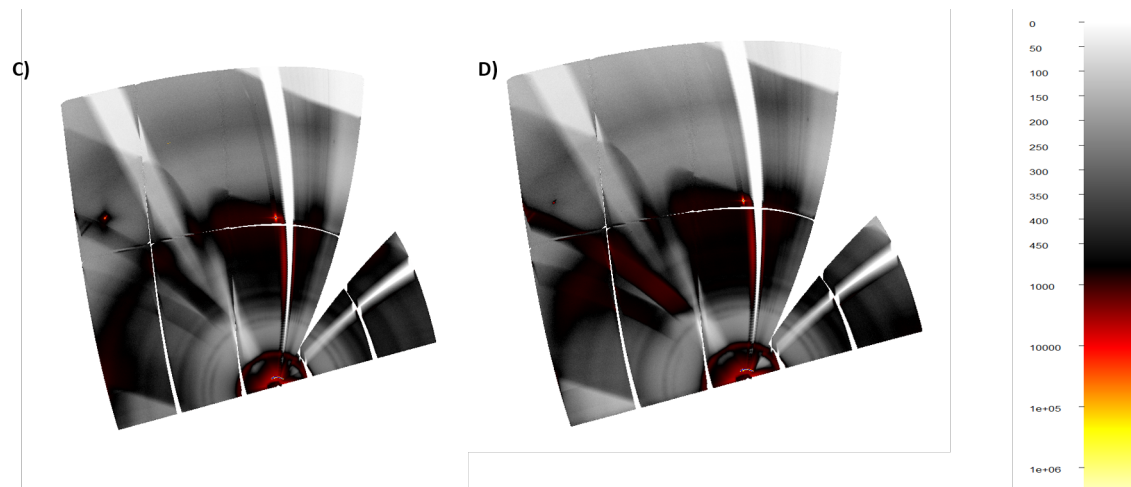


Figure 5.2: Diffuse Scattering acquisition at different temperature: C) 14.5K D) 16K

After this it is possible to start an automatic detection of all the elastic and inelastic spots and the software is able to reconstruct the reciprocal space. After this calculation it is possible to plot different plane of the reciprocal space and observe the final result. The results are in Figure 5.1 and 5.2 where the reconstruction of the $HK0$ plane at different temperatures is represented. There are two spots corresponding to the (200) and (220) reflection in all the images but there is no evidence of satellites. So, in principle, this result are not useful and our decision is to move to an IXS acquisition, in order to have higher resolution.

A problem that must be solved in this experiment if we want to see some anomalies is the accessible region of the reciprocal space. Now it is possible to observe only two reflections, corresponding to a very small value of \mathbf{Q} , and this is due to the fact that in the head of the displax there are small windows that permits the x-rays to pass through the sample. But a lot of the scattered radiation is lost due to this windows. So one solution is to fabricate a new head with bigger windows in order to increase the accessible region observe also higher \mathbf{Q} reflections. It is known that there is a dependence between I and \mathbf{Q} , $I \sim \mathbf{Q}^2$, and so the satellites associated to an higher reflection are more intense and it is easy to see them.

5.2 IXS Experiment

So an IXS experiment is necessary in order to get some results. As already said, below a Néel temperature of approximately 16.5 K, Ce^{3+} moments orders in series of ferromagnetic and paramagnetic sheets and on further cooling, the system passes trough a series of different structural phase transitions.

First of all, as for the dispersion curves acquisition, we have to mount the sample on the spectrometer. In this case, in order to reach these low temperatures, a displax has been used. This device has a base temperature of 12 K, which is perfect for the analysis of the AFP_3 phase, observed around 14 K. Then, the procedure is exactly the same as before: we have to find two diffraction spots for the construction of the \mathbf{UB} matrix, which define the sample alignment and choose the path in the reciprocal space. It is known that CeSb undergoes a tetragonal distortion due to magnetoelastic coupling between different sheets of Ce ions. If

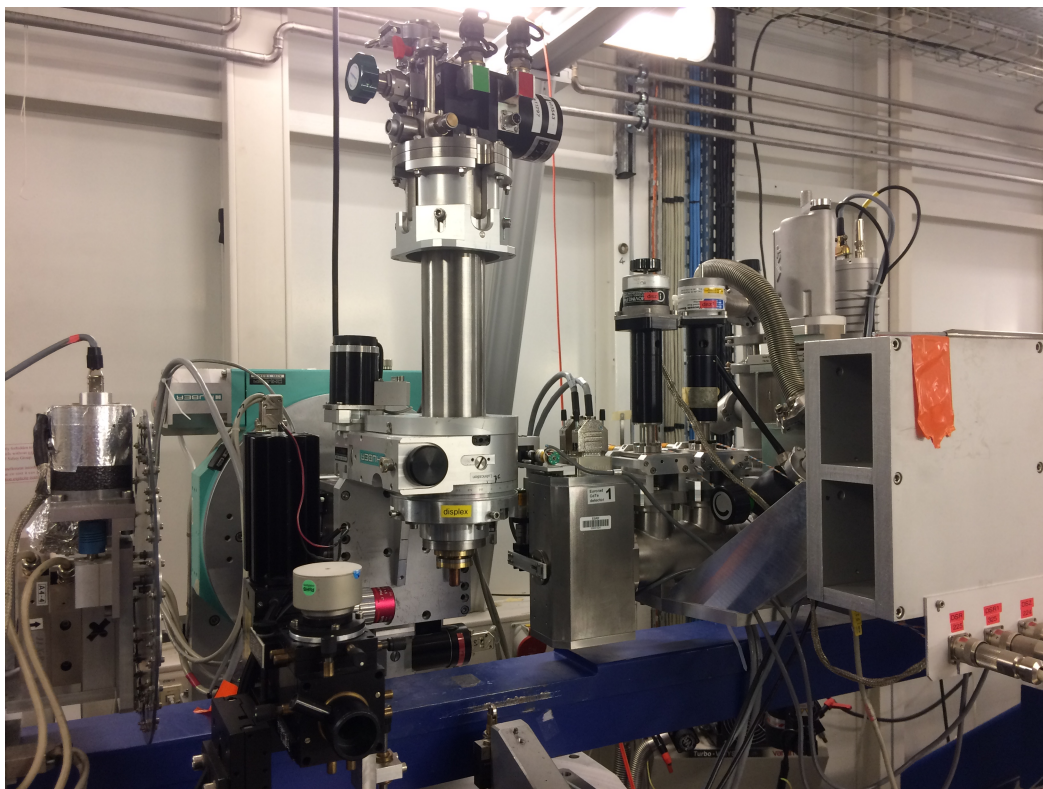


Figure 5.3: Setup for the low temperature measurement of CeSb. The displax is mounted on the adth arm of the spectrometer.

more than one domain is present in the scattering plane, a splitting of the cubic Bragg peaks will be observed below T_N . To avoid this, it should be necessary to put a magnetic field, not too much strong, in the order of 0.5-1 kOe, just to align the magnetic moments in the desired direction, and to be sure a single structural domain in the scattering plane. In our case, we don't apply a magnetic field because we want to maximize the accessible region of the reciprocal space in our experimental geometry, in reflection.

In the past years, specially during the 80's and the 90's, a lot of research has been done in this field, in order to understand this strange and complex behavior, in the beginning with neutrons scattering [37][38][39] and later, using the synchrotron sources, with X-ray diffraction techniques[40]. From these studies, the $\langle 100 \rangle$ or $\langle 110 \rangle$ directions in the reciprocal space result to be the most interesting ones. We start at 300 K with the calculation of the orientation matrix, then move to 40 K and evaluate again the orientation of the crystal. After the temperature stabilization, we perform an HKL scan along the $(4\ 0\ 0)$ direction. This type of scan is an elastic scan along a precise path and it is the first step in order to observe the presence of some anomalies. In fact, what we are looking for here is the presence of the satellite peaks at particular positions, just next to the Bragg reflection. The result of this scan is reported in Figure 5.4 where it is possible to observe clearly the presence of the first, second and third order satellite peaks at the exactly positions of $2/7$, $4/7$, $6/7$. But, what is more surprising is the fact that it is visible also another peak, just next to the first order, at $q \approx 0.240$. This peak has an unknown origin because it is not associated to any high order components of the

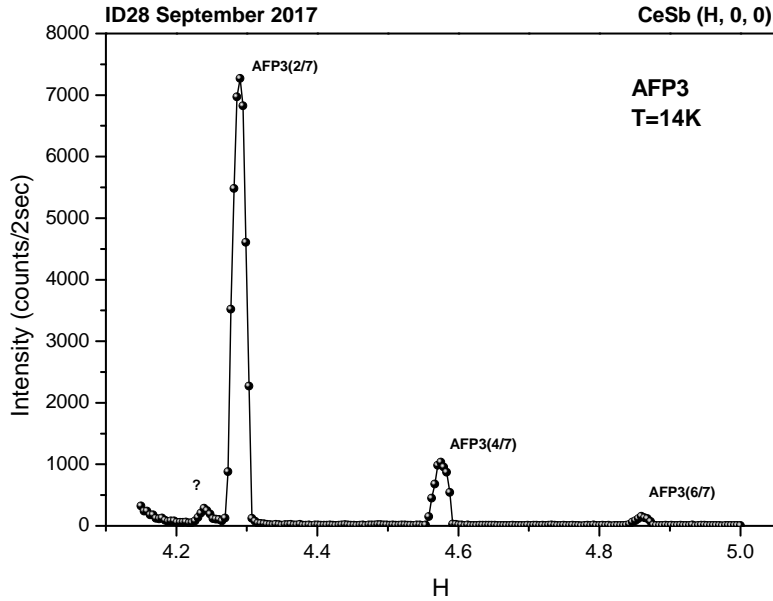


Figure 5.4: Scan of the satellite peaks observed along the $(4+H, 0, 0)$ direction at 14 K.

modulation.

In order to investigate more about the nature of this peak, we perform other HKL scans along a large region of the reciprocal space, from $(3\ 0\ 0)$ up to $(7\ 0\ 0)$. This analysis is useful because it gives informations about the behavior in different Brillouin zones. The result is even more strange, as we can see from the Figure 5.5. It looks like that the peak associated to the third harmonics has some symmetric cancellation only in particular positions, on the left of the Bragg peak. Also the anomalous peak at $q \approx 0.240$ is again extinct in the $-q$ direction.

For the explanation of these data it is useful to remember that what we observe here is the result of the scattering between photons and electrons, or more in general, charge density, which is related to the distribution of the electron cloud around the crystal structure. As already said, there are a lot of papers that deals with this problem, and the general conclusion is that there are more than one cause that give rise to this particular intensity pattern. First there is a lattice modulation that can be explained by the model that the effective thickness of Γ_8 Ce^{3+} layer is smaller than that of Γ_7 Ce^{3+} one[41]. The difference in the ionic size in the Ce ions causes a variation in the form factor and this give rise to the satellite peaks. The model is based on the parameter δ as the lattice-modulation. The distance between neighboring Ce-ions layers of Γ_7 state is defined as d , the distance between neighboring Γ_8 -like Ce-ion layers is assumed to be shorter by a factor of δ , so that is defined as $d(1 - \delta)$. The distance between the layers of Γ_8 and Γ_7 Ce states can be defined as $d(1 - \frac{\delta}{2})$, see Figure 5.6. Starting from here it is possible to evaluate the structure factor and compare it with the experimental one. But the common conclusion is that a complete interpretation of the X-ray data in the wide reciprocal space is not achieved only by the lattice modulation model.

The second important effect that we should take in account is the $4f$ -electron orbit modula-

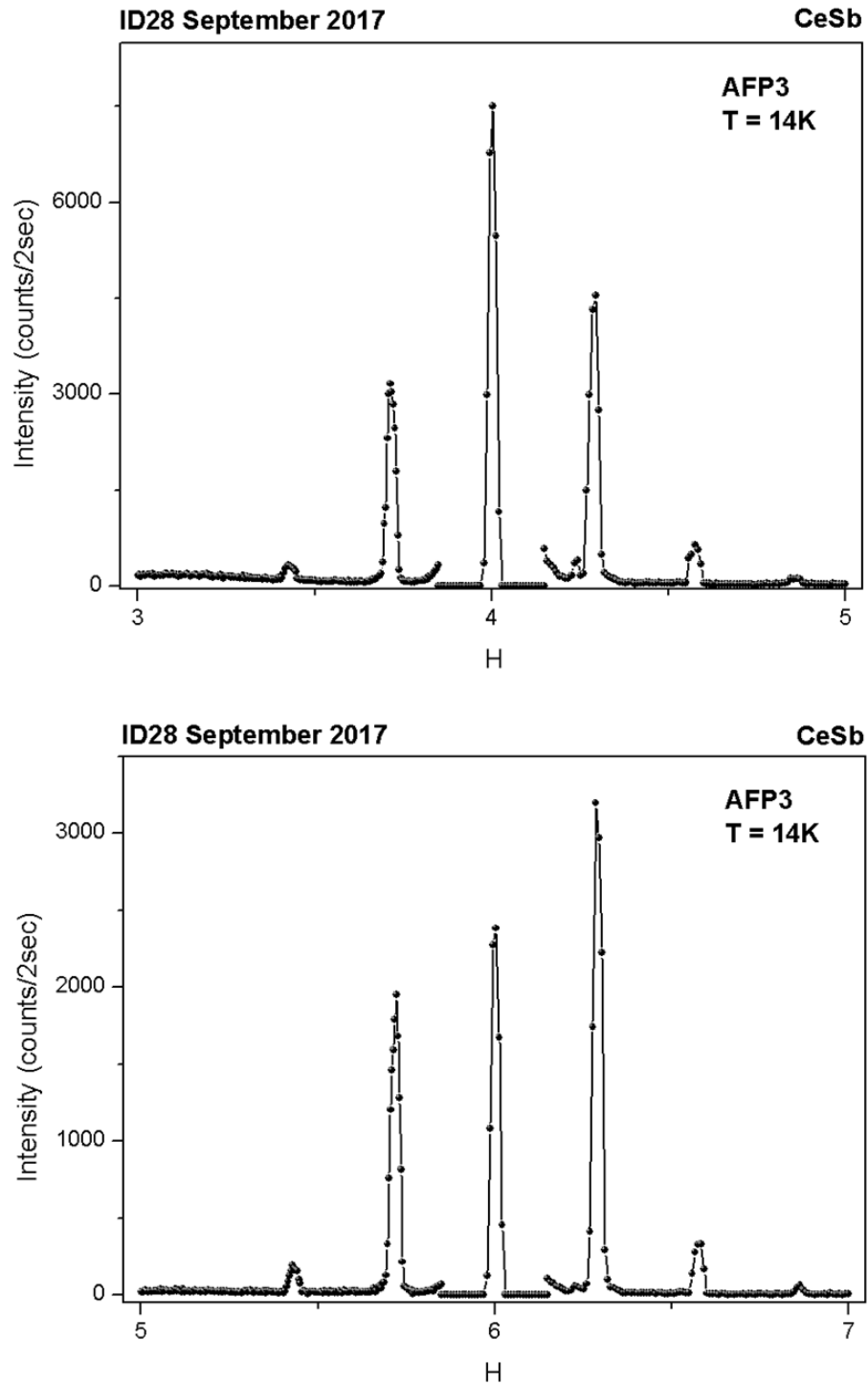


Figure 5.5: HKL scan along the (100) direction from (3, 0, 0) up to (7.15, 0, 0). It is clearly visible the systematic cancellation of the third order satellite.

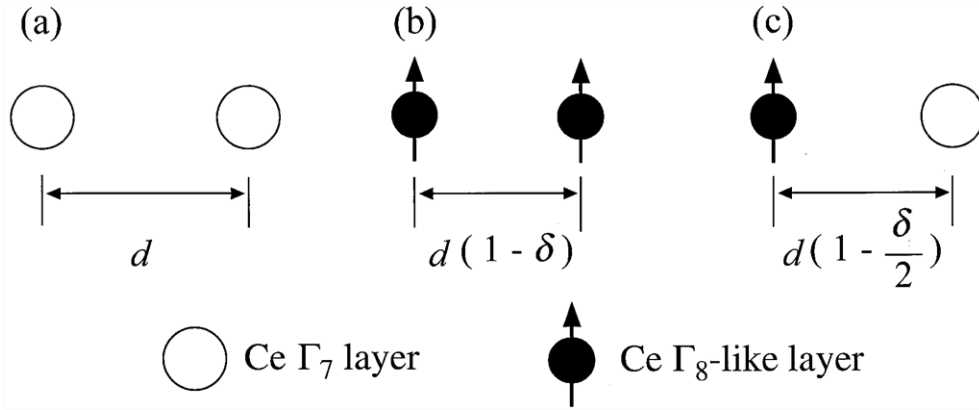


Figure 5.6: Schematic representation and definitions of interlayer distances in the model. Open and filled circles represent Ce-ion layers of the Γ_7 state and those of the Γ_8 -like state, respectively. Picture taken from ref. [41]

tion, which cause an atomic form factor modulation[42] [43]. It is associated to the mixing effect between the Γ_8 state of the Ce ions and the p state of the neighboring element, Antimony in this case, only within the ferromagnetic layers. It results in a difference between the form factor of the two types of cerium ions, in particular the Γ_8 state is expected to give larger form factor than that of the Γ_7 , because the electronic distribution of the Γ_8 state is anisotropically extending in the $[100]$ - $[010]$ plane whereas that of the Γ_7 state is rather isotropic. So the conclusion in that considering the two kinds of modulations is the correct way to explain correctly the experimental data.

Added on the charge-density modulation there is also a magnetic one and it is due to the fact that in this phase, but also in the others, there is an alternative presence of magnetic planes and non magnetic planes. This can be seen as a magnetic moment modulation, clearly visible from Figure 3.7, so this should be also taken into account in order to describe correctly the experimental data.

Anyway, this result open a completely new page in the analysis of this magnetic structure and maybe the model is more complicated with respect to the one that we have supposed until now. The possible explanations are different: maybe the charge modulation coupled with the displacement field results in a two opposite interactions that completely cancels out the third harmonics, and to explain the anomalous peak at $q \approx 0.240$ it is possible to introduce another distance to the three already considered in the model: the distance between two Ce Γ_8 -like layers which are parallel is different from the distance when the two layers are antiparallel, and this is due to the different strength of the magnetostatic coupling. Up to now, this is only an hypothesis and it has to be confirmed by future analysis.

The second part of this analysis on anomalies deals with an IXS scans acquisition in order to understand better the problem. Figure 5.7 shows a spectrum measured at $\mathbf{Q} = (4.4, 0, 0)$ in the AFP₃ phase. It is clearly visible the elastic peak at zero energy transfer, the inelastic one at $\sim 11\text{meV}$ that corresponds to a longitudinal acoustic phonon propagating along $\langle 100 \rangle$ (LA(100)) and another peak, at $\sim 4\text{meV}$. This peak is not observable at room temperature or in general above the Néel temperature, so it should be associated to a new phonon mode characteristic of this phase. One possibility is that the observed anomalous phonon mode

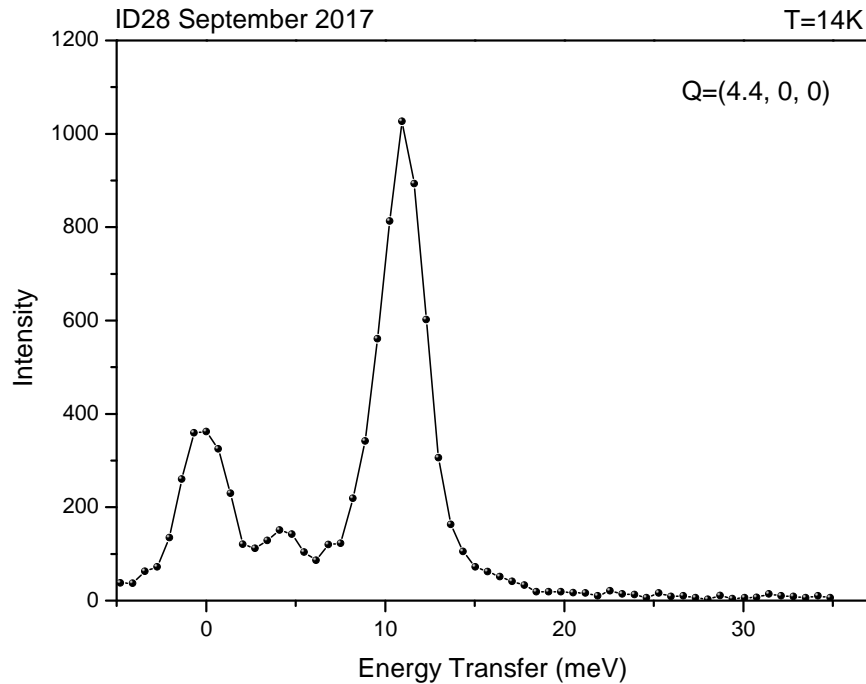


Figure 5.7: Inelastic scan at 14 K. It is clearly visible a peak at $\approx 4\text{meV}$ corresponding to a new phonon mode

can be assigned to a localized stretching mode between Ce and Sb ions in the ferromagnetic layers, where the strong p-f mixing modify also the Ce-Sb distance. One way to confirm this idea is to observe the intensity of the peak at a half \mathbf{Q} ; in fact it is known that the phonon intensity is proportional to $|\mathbf{Q} \cdot \mathbf{e}|^2$ where \mathbf{e} is the direction of the atomic displacement. So if the new intensity is half of those at $\mathbf{Q} = (4.4, 0, 0)$ the new excitation has a localized phonon character.

5.3 A proposed model for the observed anomalies

In order to give an explanation to the elastic scans obtained from the experiment, the last step of this work is to propose a possible model which can predict the satellite position together with the systematic cancellation of the third order harmonics. It is a model based on the fact that these satellite peaks arise from a static displacement of the atomic planes from their average positions, displacement which is due to the magnetic interaction between different planes.

Let's start from the general drawing for the $\frac{4}{7}$ phase of CeSb, which is represent in Figure 5.8. It is possible to see that there is a periodic arrangement in a super-cell structure, where each super-cell is composed by 7 atomic planes. The origin is set on the paramagnetic plane on the left and the equilibrium positions of the other planes are: $a, 2a, 3a, \dots$ where $a=3.213\text{\AA}$ in this model is half of the standard a_0 , side of the conventional unit cell for the *fcc*

5.3. A proposed model for the observed anomalies

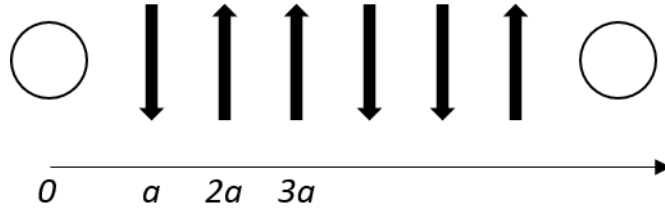


Figure 5.8: Representation of the average position of the 7 different atomic planes in the $\frac{4}{7}$ phase of the CeSb

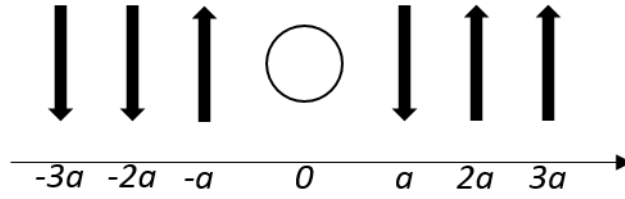


Figure 5.9: Another representation of the $\frac{4}{7}$ phase of CeSb that explains the symmetry properties of the magnetic structure

structure. The static displacement is label as ϵ , and it is assumed to be a small pure number.

So, in general, there are 7 different epsilons, from ϵ_0 up to ϵ_6 , and each one describes the displacement of a proper plane. But the magnetic structure imposes a symmetry plane which is located at 0, corresponding to the paramagnetic plane position, see Figure 5.9.

When exchanging the atoms through that symmetry plane, all the magnetic moments are reversed, which makes all the distances unchanged, since each of them depend on the product of the two atomic moments. From this symmetry follows that the number of epsilons is reduced; in particular $\epsilon_0 = 0$ because is the displacement of the paramagnetic plane, which is the symmetry plane of the super-structure. A general displacement generated from the interaction between the paramagnetic plane and the plane in position a is equal and opposite to the one generated between the paramagnetic plane and the plane in position $-a$, and this is true for every plane, so it is possible to demonstrate that

$$\epsilon_6 = -\epsilon_1; \quad \epsilon_5 = -\epsilon_2; \quad \epsilon_4 = -\epsilon_3 \quad (5.1)$$

and so the total number of different displacements is reduced from 7 up to 3. So it is possible to distinguish three different types of interactions associated to the three different ϵ 's: one between two ferromagnetic plane which are parallel, one for the antiparallel planes and one for the ferromagnetic-paramagnetic interaction.

Now, after this brief introduction, it is possible to evaluate the effect of these displacements on the structure factor, which is written as

$$F = \sum_{n=0}^6 e^{2\pi i(q + \frac{P}{7})(n + \epsilon_n)} \quad (5.2)$$

where, for this first calculation, we set the atomic form factor $f(Ce)$ and $f(Sb)$ to 1, focusing only on the phase contribution. The term $q + \frac{P}{7}$ is a notation for the scattering vector, and

Chapter 5. Phonon anomalies in Cerium Antimony

q and P are half of the usual value. So, for example, $q = 2$, (200), corresponds to the (400) reflection, $q = 3$ to the (600) and so on. P goes from 1 to 7 and labels all the satellite peaks that we observe in the scans; it is equal to 1 for the $\frac{2}{7}$ satellite, equal to 2 for the $\frac{4}{7}$, and so on. So the structure factor become

$$F = \sum_{n=0}^6 e^{2\pi i(q+\frac{P}{7})n} e^{2\pi i(q+\frac{P}{7})\epsilon_n}$$

It is possible to observe that:

- the first exponential

$$e^{2\pi iqn} e^{2\pi i\frac{P}{7}n} = e^{2\pi i\frac{P}{7}n}$$

because q is an integer number

- ϵ_n is small, so it is possible to expand the second exponential as a Taylor expansion

$$e^{2\pi i(q+\frac{P}{7})\epsilon_n} = 1 + 2\pi i \left(q + \frac{P}{7} \right) \epsilon_n - 2\pi^2 \left(q + \frac{P}{7} \right)^2 \epsilon_n^2 + \dots$$

and the expansion is stopped at the second order term.

The result is

$$\begin{aligned} F &= \sum_{n=0}^6 e^{2\pi i\frac{P}{7}n} \left[1 + 2\pi i \left(q + \frac{P}{7} \right) \epsilon_n - 2\pi^2 \left(q + \frac{P}{7} \right)^2 \epsilon_n^2 \right] \\ &= \sum_{n=0}^6 e^{2\pi i\frac{P}{7}n} + \left\{ e^{2\pi i\frac{P}{7}n} \left[2\pi i \left(q + \frac{P}{7} \right) \epsilon_n \right] \right\} - \left\{ e^{2\pi i\frac{P}{7}n} \left[2\pi^2 \left(q + \frac{P}{7} \right)^2 \epsilon_n^2 \right] \right\} \end{aligned}$$

Using the fact that the symmetry reduce the number of displacements, and notice that the first sum is equal to zero, we obtain

$$F = \sum_{n=1}^3 \left[e^{2\pi i\frac{P}{7}n} - e^{-2\pi i\frac{P}{7}n} \right] 2\pi i \left(q + \frac{P}{7} \right) \epsilon_n - \left[e^{2\pi i\frac{P}{7}n} + e^{-2\pi i\frac{P}{7}n} \right] 2\pi^2 \left(q + \frac{P}{7} \right)^2 \epsilon_n^2$$

and using the complex definitions for *sin* and *cos*, we arrive to the final expression

$$F = \sum_{n=1}^3 \left[-2\sin\left(2\pi\frac{P}{7}n\right) 2\pi \left(q + \frac{P}{7} \right) \epsilon_n \right] - \left[2\cos\left(2\pi\frac{P}{7}n\right) 2\pi^2 \left(q + \frac{P}{7} \right)^2 \epsilon_n^2 \right] \quad (5.3)$$

So now we have the expression of the so called *trigonometric* structure factor, the part of the total structure factor which depends only on the geometrical positions of the atoms, leaving out the form factor.

The next step is to evaluate the intensities of the Bragg and satellite peaks due to this particular form of the structure factor, and compare them with the observed intensities. In order to do this we have to add the atomic form factors of the elements, the value of the epsilons and the polarization factor. The value of the form factor can be obtained using the

5.3. A proposed model for the observed anomalies

Q, P	Peak at	I	I_{obs}
1, 4	$3 + \frac{1}{7}$	0.07	0
1, 5	$3 + \frac{3}{7}$	4.3	2.2
1, 6	$3 + \frac{5}{7}$	35	32
2, 1	$4 + \frac{2}{7}$	39	45
2, 2	$4 + \frac{4}{7}$	3.9	6.1
2, 3	$4 + \frac{6}{7}$	1.2	1.3
2, 4	$5 + \frac{1}{7}$	0.04	0
2, 5	$5 + \frac{3}{7}$	6.6	1.8
2, 6	$5 + \frac{5}{7}$	42	19
3, 1	$6 + \frac{2}{7}$	43	31
3, 2	$6 + \frac{4}{7}$	3.3	3.2
3, 3	$6 + \frac{6}{7}$	1.5	0.5
3, 4	$7 + \frac{1}{7}$	0.007	0

Table 5.1: Table with the predicted and observed values of the Bragg and satellite peaks in *CeSb*

procedure presented in the *International Tables For Crystallography, Vol. C, chapter 6*[44], where the atomic form factor can be expressed as

$$f\left(\frac{\sin\theta}{\lambda}\right) = \sum_{i=1}^4 a_i e^{-b_i \frac{\sin^2\theta}{\lambda^2}} + c \quad (5.4)$$

where a_i , b_i and c are coefficients using to obtain the best fit to the atomic scattering curves. The values of the epsilons are the result of a trial and error procedure: starting from an estimated value we look at the resulting intensity, change a little bit the value, look if this improves or degrades the result, and so on. The final values are:

$$\epsilon_1 = -0.0028 \quad \epsilon_2 = -0.0084 \quad \epsilon_3 = -0.0042 \quad (5.5)$$

Remember that this values are pure numbers and express the absolute displacement of the atomic plane in units of a . The predicted intensity I is the square of F^{trig} , which is given by the equation 5.3, times the form factor, calculated using equation 5.4, times the polarization factor. For this first calculation the assumption is that only Cerium atoms in the atomic planes are subject to a displacement, and the Sb atoms are fixed. Of course, the form factor from Equation 5.4 does not include the fact that there are Γ_7 and Γ_8 Ce ions, so a new parameter is added, C_{ez} , which stands for $C_{e_{zero}}$, assuming a slightly different scattering factor for the Ce at the origin, see Figure 5.9, which has a zero momentum. The numeric value of C_{ez} is obtained again using a trial and error approach, find $C_{ez} = 0.00035$. In the end, it is possible to find the predicted intensity.

From Table 5.1 it is clear that the model predicts quite well the periodic cancellations of the peaks, and also the intensities of the others, but not all the peaks are well calculated, for example $5 + \frac{3}{7}$. This is probably due to the fact that here only the displacements of the Cerium atoms are considered, including also the displacements of Sb atoms improves the model,

Chapter 5. Phonon anomalies in Cerium Antimony

but the problem is that there will be six parameters to adjust and not only three. Another improvement can be done about the parameter C_{ez} , because in this model it is considered constant.

It is also possible to determine the variations of the distance between planes, labelled as η . In this way we can see if the interaction is repulsive or attractive. The relations are

$$\begin{aligned}\eta_1 &= (\epsilon_1 - \epsilon_0)a = -0.0028a \\ \eta_2 &= (\epsilon_2 - \epsilon_1)a = -0.0056a \\ \eta_3 &= (\epsilon_3 - \epsilon_2)a = 0.0042a\end{aligned}\tag{5.6}$$

So, calling d_{nm} the distance between the plane in position n and the plane in position m , the result is

$$\begin{aligned}d_{01} &= a + \eta_1 = a - 0.0028a \\ d_{12} &= a + \eta_2 = a - 0.0056a \\ d_{23} &= a + \eta_3 = a + 0.0042a\end{aligned}\tag{5.7}$$

where it is clear that the effect of the magnetic interaction on d_{23} , distance between parallel planes, is increased, there is a repulsion. The other two distances, instead, are reduced, meaning that we have an attraction.

CHAPTER 6

Conclusions

As already said, this measurements on CeBi and CeSb are only a part of a bigger analysis: a complete study on the lattice dynamics of all the cerium compounds, in order to obtain informations on the all physical properties and the differences between them. For the first part of the work, regarding the dispersion curves acquisition, it is possible to observe that there are similar features between the two compounds and this is normal as they have same symmetry and structure, they actually belong to the same spatial group. The main difference is the fact that Bismuth is heavier than Antimony, so the curves are push down in energy and this is a problem in the data acquisition because the inelastic peaks associated to acoustic and optical modes are very close together and it is difficult to distinguish them. Another problem is the fact that the CeBi crystal is not so perfect and this can be seen in the IXS scan where the elastic peak is very intense. This is again a problem because this large peak at zero energy can mask the low energy inelastic peaks, in positions just next to the Γ point.

Also, the most important aspect of this compounds, are their anomalous magnetic properties, associated to a creation of ordered systems and superlattice structures. Up to now the entire analysis is done on CeSb and the next step is to define a low-temperature study of CeBi, as we already have all the information on the dispersion curves. It is possible to say that there is not only one precise modulation that induce this superlattice structures, but this is a superposition of different effects. Of course the last results during the IXS experiment open a completely new chapter on the physics hidden behind these compounds. As already said, information from an X-ray diffraction experiment are related to the interaction between photons and electrons, which gives rise to a specific diffraction patterns, where a constructive interaction is obtained only for particular values of \mathbf{Q} . In conclusion, one of the possible future improvements will be to understand and distinguish the different contributions that play a role in this particular charge modulation. It can be done for example with a polarization

Chapter 6. Conclusions

analysis of the x-ray or using neutrons, that have a magnetic moment, in order to investigate the magnetic structure more in detail.

Another objective for the future is to understand the origin of the anomalous peak and to understand better the systematic extinction of some harmonics. The model, that we proposed in this Thesis work, has a good matching with the results. However, we did not take in account a series of complications: 1) the displacements of the Sb atoms; 2) the constant value of the form factor of the Γ_7 cerium. Another improvement for the future is a commissioning of a new head for the diffractometer in order to be able to reconstruct correctly a big region of the reciprocal space with a Diffuse Scattering (DS) analysis, using the side station in ID28. An head is necessary in both experiments because we have to work at low temperature and without oxygen because the Cerium compounds are extremely subjected to oxidation. The goal is to have an head with bigger windows in order to collect more radiation in the PILATUS detector and to have access to the higher order reflections. This type of experiment has the advantage to perform an integration over a selected area of the intensity incoming on the detector. In this case, after the measurement it will be possible to obtain a larger region of the reciprocal space and the scattering from the windows will be avoided. We think we will be able, then, to see the satellite peaks, also if they have a very weak intensities.

Elastic waves in Cubic crystals

The forces acting on an element of volume in the crystal give rise to an equation of motion, for example in the x direction

$$\rho \frac{\partial^2 u}{\partial t^2} = \frac{\partial X_x}{\partial x} + \frac{\partial X_y}{\partial y} + \frac{\partial X_z}{\partial z} \quad (\text{A.1})$$

where ρ is the density of the material and u is the displacement in the x direction, with similar equations for the y and z directions. From the theory, the relation between the force and the strain for a cubic crystal gives

$$\rho \frac{\partial^2 u}{\partial t^2} = C_{11} \frac{\partial e_{xx}}{\partial x} + C_{12} \left(\frac{\partial e_{yy}}{\partial x} + \frac{\partial e_{zz}}{\partial x} \right) + C_{44} \left(\frac{\partial e_{xy}}{\partial y} + \frac{\partial e_{zx}}{\partial z} \right)$$

with x, y and z directions parallel to the cube edge, and e is the strain vector. Using the definitions of the strain components we have

$$\rho \frac{\partial^2 u}{\partial t^2} = C_{11} \frac{\partial^2 u}{\partial x^2} + C_{44} \left(\frac{\partial^2 u}{\partial y^2} + \frac{\partial^2 u}{\partial z^2} \right) + (C_{12} + C_{44}) \left(\frac{\partial^2 v}{\partial x \partial y} + \frac{\partial^2 w}{\partial x \partial z} \right) \quad (\text{A.2})$$

where u, v and w are the components of the displacement \mathbf{R} . The corresponding equations for the motion in the y and z directions are:

$$\rho \frac{\partial^2 v}{\partial t^2} = C_{11} \frac{\partial^2 v}{\partial y^2} + C_{44} \left(\frac{\partial^2 v}{\partial x^2} + \frac{\partial^2 v}{\partial z^2} \right) + (C_{12} + C_{44}) \left(\frac{\partial^2 u}{\partial x \partial y} + \frac{\partial^2 w}{\partial y \partial z} \right) \quad (\text{A.3})$$

$$\rho \frac{\partial^2 w}{\partial t^2} = C_{11} \frac{\partial^2 w}{\partial z^2} + C_{44} \left(\frac{\partial^2 w}{\partial x^2} + \frac{\partial^2 w}{\partial y^2} \right) + (C_{12} + C_{44}) \left(\frac{\partial^2 u}{\partial x \partial z} + \frac{\partial^2 v}{\partial y \partial z} \right) \quad (\text{A.4})$$

These are the equations for the motion in the three directions, let's study some specific case.

Appendix A. Elastic waves in Cubic crystals

A.1 Wave in the [100] Direction

A wave in the [100] direction is characterized by the fact that the wave vector \mathbf{K} has only one component. Let's suppose that the particle displacement is parallel to the \mathbf{K} vector, so the general solution of the Equation B.2 is

$$u = u_0 e^{i(\mathbf{K}x - \omega t)}$$

Both wave vector and particle displacement are long the x cube edge. We substitute this equation into B.2 we find

$$\omega^2 \rho = C_{11} \mathbf{K}^2$$

the resulted wave velocity, LA[100], is

$$v_s = \sqrt{\frac{C_{11}}{\rho}} \quad (\text{A.5})$$

The opposite situation is the one with the wave vector along the x direction and with the particle displacement, for example, in the y direction

$$v = v_0 e^{i(\mathbf{K}x - \omega t)}$$

and using the equation B.3, the velocity of a transverse wave in the [100] direction, TA[100], is

$$v_s = \sqrt{\frac{C_{44}}{\rho}} \quad (\text{A.6})$$

The identical velocity is obtained if the particle displacement is in the z direction of a cubic crystal. So for this polarization the two independent transverse waves have equal velocities.

A.2 Wave in the [110] Direction

This case involves a wave that propagates in a face diagonal direction of the cubic crystal. Considering a wave propagates in the xy plane with particles displacement along z direction

$$w = w_0 e^{i(K_x x + K_y y - \omega t)}$$

which gives

$$v_s = \sqrt{\frac{C_{44}}{\rho}} \quad (\text{A.7})$$

for the TA1[110]. A more interesting situation is when there is a wave that propagates in the xy plane with particle motion in the same plane. So we have

$$u = u_0 e^{i(K_x x + K_y y - \omega t)} \quad v = v_0 e^{i(K_x x + K_y y - \omega t)}$$

So here we have to solve a system of two equations

$$\begin{aligned} \omega^2 \rho u &= (C_{11} K_x^2 + C_{44} K_y^2) + (C_{12} + C_{44}) K_x K_y v \\ \omega^2 \rho v &= (C_{11} K_y^2 + C_{44} K_x^2) + (C_{12} + C_{44}) K_x K_y u \end{aligned} \quad (\text{A.8})$$

A.2. Wave in the [110] Direction

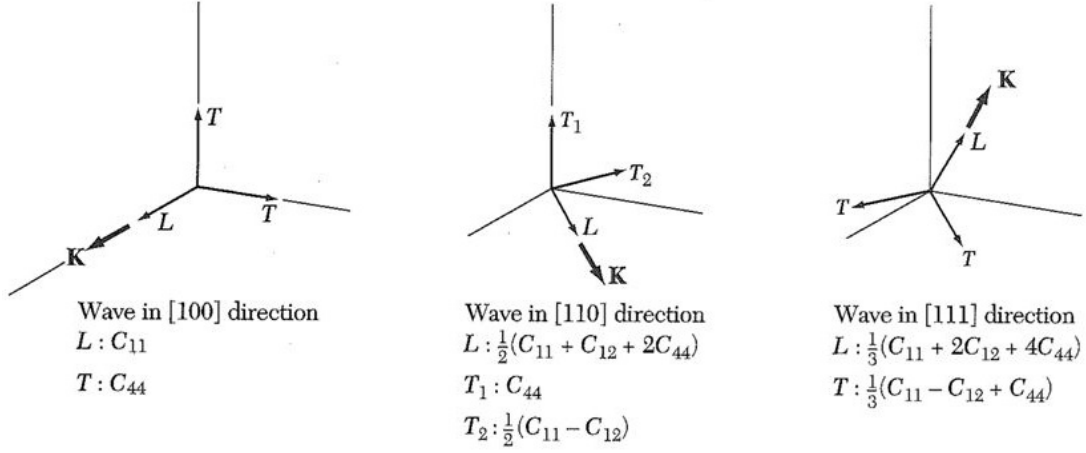


Figure A.1: Effective elastic constants for the three modes of elastic waves in the principal propagation directions in cubic crystals. The two transverse modes are degenerate for propagations in the [100] and [111] directions.

obtaining the roots

$$\omega^2 \rho = \frac{1}{2}(C_{11} + C_{12} + 2C_{44})K^2$$

$$\omega^2 \rho = \frac{1}{2}(C_{11} + C_{12})K^2$$

In order to understand the direction of particle displacement we have to substitute the first and the second root in the Equations B.8 and find that for the first equation $u = v$ so the particle displacement is along [110] and parallel to \mathbf{K} . The second root gives $u = -v$, the particle displacement is along [1-10] and perpendicular to the wave vector \mathbf{K} . The same analysis can be done for the [111] direction obtaining the values of the sound velocities also for this polarization direction.

In the Figure it is possible to observe the effective elastic constants for the three different polarization. These relation are also useful if we want to obtain information on the elastic constant starting from the experimental data about the dispersion curves. In fact, using a linear fitting of the points just next to the Γ point it is possible to evaluate the slope of the curve in zero, which is the sound velocity and from this relation evaluate all the constants.

Acknowledgements

I am intensely grateful to most of the people I met in the past years.

First of all, I would like to extend my gratitude to Prof. Giacomo Ghiringhelli for the great opportunity he gave me to stay at the ESRF and for trusting me.

Special thanks go to my supervisor at the ESRF, Dott. Luigi Paolasini, who kindly hosted me at the beamline ID28. Thanks for all the time he devoted to me and for encouraging me everyday to do my best, I really appreciated it.

Very special thanks also to Arianna and Michal, not only colleagues for me, but special friends. We shared unforgettable moments at the ESRF where they teach me a lot of things but also during weekends and holiday walking around the mountains next to the city.

I would like to thank all staff of the ID28 beamline. Thanks to Michaela, Tra and Adrien for helping me with my problems and for nice discussions after every delicious lunch at the canteen.

Thanks to all the people that I met at the ESRF and in Grenoble, in particular Laura, Chaty and Alessandro, other master students that shared their thesis period with me.

Thanks also to all my travel companions during this six years of study, thanks for every discussion, from sport to physics.

Thanks to Valeria, who softened my comeback. I would like to extend my gratitude also to my parents, without whose support and understanding I would never completed this master degree.

Thanks to everybody, my heartfelt gratitude to all of you.

Bibliography

- [1] S. Mobilio and F. Boscherini C. Meneghini. *Synchrotron Radiation: Basics, Methods and Applications*. Springer-Verlag Berlin Heidelberg, 2015.
- [2] E. Burkel. Phonon spectroscopy by inelastic x-ray scattering. *Rep. Prog. Phys.*, 63(2):171, 2000.
- [3] M. Krish and F. Sette. *Inelastic X-ray Scattering from Phonons. Light Scattering in solids, Novel Materials and Techniques*. Topics in Applied Physics, 2007.
- [4] W. Graeff and G. Materlik. Millielectron volt energy resolution in bragg backscattering. *Nucl. Instrum. Methods Phys. Res.*, 195:97–103, 1982.
- [5] C. Masciovecchio, U. Bergmann, M. Krisch, G. Ruocco, F. Sette, and R. Verbeni. A perfect crystal x-ray analyser with mev energy resolution. *Nucl. Instrum. Methods Phys. Res., Sect. B*, 111:181–186, 1996.
- [6] C. Masciovecchio, U. Bergmann, M. Krisch, G. Ruocco, F. Sette, and R. Verbeni. A perfect crystal x-ray analyser with 1.5 mev energy resolution. *Nucl. Instrum. Methods Phys. Res., Sect. B*, 117:339–340, 1996.
- [7] P. Kraft, A. Bergamaschi, Ch. Broennimann, R. Dinapoli, E. F. Eikenberry, B. Henrich, I. Johnson, A. Mozzanica, C. M. Schleputz, P. R. Willmott, , and B. Schmitta. Performance of single-photon-counting pilatus detector modules. *J. Synchrotron Radiat.*, 16:368–375, 2009.
- [8] J. Als-Nielsen and D. McMorrow. *Elements of Modern X-ray Physics*. Wiley, second edition, 2011.
- [9] B. T. M. Willis and A. W. Pryor. *Thermal vibrations in crystallography*. London ; New York : Cambridge University Press, 1975.
- [10] N. W. Ashcroft and N. D. Mermin. *Solid State Physics*. Saunders College Publishing, 1976.
- [11] T. Hahn, editor. *International Tables for Crystallography Volume A: Space-group symmetry*. Springer Netherlands, 2002.
- [12] H. Heer, A. Furrer, W. Halg, and O. Vogt. Neutron spectroscopy in the cerium mononictides. *J. Phys. C: Solid State Phys.*, 12(23):5207, 1979.

Bibliography

- [13] R. J. Birgeneau, E. Bucher, J. P. Maita, L. Passell, and K. C. Turberfield. Crystal fields and the effective-point-charge model in the rare-earth pnictides. *Phys. Rev. B*, 8:5345, 1973.
- [14] J. Rossat-Mignod, P. Burlet, S. Quezel, J.M. Effantin, D. Delacote, H. Bartholin, O. Vogt, and D. Ravot. Magnetic properties of cerium monopnictides. *J. Magn. Magn. Mater.*, 31(Part 1):398–404, 1983.
- [15] G. H. Lander, M. H. Mueller, and O. Vogt. Magnetic and lattice properties of cebi. *AIP Conf. Proc.*, 24:430–431, 1975.
- [16] F. Hulliger, M. Landolt, H. R. Ott, and R. Schmelczer. Low-temperature magnetic phase transitions of cebi and cesb. *J. Low Temp. Phys.*, 20(3):269–284, Aug 1975.
- [17] H. Takahashi and T. Kasuya. Anisotropic p-f mixing mechanism explaining anomalous magnetic properties in ce monopnictides: I. effective 4f level. *J. Phys. C: Solid State Phys.*, 18(13):2697–2707, 1985.
- [18] J. Rossat-Mignod, P. Burlet, J. Villain, H. Bartholin, Wang Tcheng-Si, D. Florence, and O. Vogt. Phase diagram and magnetic structures of cesb. *Phys. Rev. B*, 16:440–461, Jul 1977.
- [19] G. Busch and O. Vogt. Valency changes in cerium compounds. *Phys. Lett.*, 20:152–154, 1966.
- [20] B. Rainford, K. C. Turberfield, G. Brusch, and O. Vogt. Magnetic properties of ceas and cesb deduced from neutron scattering data. *J. Phys. C*, 1:679–683, 1968.
- [21] G. Busch, W. Stutius, and O. Vogt. Crystal field splitting and spin waves in antiferromagnetic cesb. *J. Appl. Phys.*, 42:1493, 1971.
- [22] H. Bartholin, D. Florence, W. Tcheng-Si, and O. Vogt. Magnetic properties of cebi. *phys. stat. sol. (a)*, 24:631–636, 08 1974.
- [23] T. Tsuchida and Y. Nakamura. Field induced magnetic phases of cerium-bismuth compound with sodium-chloride structure. *J. Phys. Soc. Jpn.*, 22:942–943, 1967.
- [24] T. Tsuchida and W. E. Wallace. Magnetic characteristics of lanthanide-bismuth compounds. *J. Chem. Phys.*, 43:2885, 1965.
- [25] T. Tsuchida, T. Suzawa, and Y. Nakamura. Crystal field and magnetic properties of cebi. *Phys. Stat. Sol.*, 44:K25, 1971.
- [26] W. R. Busing and H. A. Levy. Angle calculations for 3- and 4-circle X-ray and neutron diffractometers. *Acta Crystallogr.*, 22(4):457–464, Apr 1967.
- [27] H. M. Tutuncu, S. Bagci, and G. P. Srivastava. Electronic, elastic and phonon properties of the rock-salt lasb and ysb. *J. Phys.: Condens. Matter*, 19(15):156207, 2007.
- [28] V. Mankad, S. K. Gupta, I. Lukacevic, and P. K. Jha. Pressure-induced structural phase transition and elastic properties in rare earth cebi and labi. *J. Phys. Conf. Ser.*, 377(1):012076, 2012.
- [29] M. Born and K. Huang. *Dynamical Theory of Crystal Lattices*. Oxford: Clarendon press, 1954.
- [30] A. A. Maradudin, E. W. Montroll, G. H. Weiss, and I. P. Ipatova. *Theory of Lattice Dynamics in the Harmonic Approximation*, volume Supplement3 of *Solid State Physics*. Academic Press, New York, second edition, 1971.
- [31] H. Ibach and H. Lüth. *Solid-State Physics: An Introduction to Principles of Materials Science*. Springer-Verlag Berlin Heidelberg, 2009.

- [32] S. Baroni, S. de Gironcoli, A. Dal Corso, and P. Giannozzi. Phonons and related crystal properties from density-functional perturbation theory. *Rev. Mod. Phys.*, 73:515–562, Jul 2001.
- [33] D. Alfe. Phon: A program to calculate phonons using the small displacement method. *Comput. Phys. Commun.*, 180:2622–2633, 2009.
- [34] P. Giannozzi, S. Baroni, N. Bonini, M. Calandra, R. Car, C. Cavazzoni, D. Ceresoli, G. L. Chiarotti, M. Cococcioni, and A. Dal Corso. Quantum espresso: a modular and open-source software project for quantum simulations of materials. *J. Phys.: Cond. Matter*, 21, 2009.
- [35] X. Gonze, B. Amadon, P. M. Anglade, J. M. Beuken, F. Bottin, P. Boulanger, F. Bruneval, D. Caliste, R. Caracas, and et al. Cote, M. Abinit: First-principles approach to material and nanosystem properties. *Comput. Phys. Commun.*, 180(12):2582–2615, 2009.
- [36] P. Souvatzis, O. Eriksson, M. I. Katsnelson, and S. P. Rudin. The self-consistent ab initio lattice dynamical method. *Comput. Mater. Sci.*, 44:888–894, 2009.
- [37] K. Iwasa, M. Kohgi, M. Braden, J. M. Mignot, H. Kitazawa, and T. Suzuki. Anomalous phonon excitations associated with strong p-f mixing effect of cesb and cebi. *J. Magn. Magn. Mater.*, 272(Supplement):E65 – E66, 2004. Proceedings of the International Conference on Magnetism (ICM 2003).
- [38] B. Halg and A. Furrer. Anisotropic exchange and spin dynamics in the type-i (-ia) antiferromagnets ceas, cesb, and usb: A neutron study. *Phys. Rev. B*, 34:6258–6279, Nov 1986.
- [39] B. Halg, A. Furrer, W. Halg, and O. Vogt. Critical neutron scattering in the cerium monopnictides. *J. Appl. Phys.*, 53(3):1927–1928, 1982.
- [40] K. Iwasa, A. Hannan, M. Kohgi, M. Braden, J.-M. Mignot, H. Kitazawa, and T. Suzuki. Crystal-lattice modulation and phonon anomaly associated with strong p-f mixing effect of cesb. *Appl. Phys. A*, 74(1):s1779–s1781, Dec 2002.
- [41] K. Iwasa, Y. Arakaki, M. Kohgi, and T. Suzuki. Evidence for crystal-lattice modulation due to spatially restricted enhancement of mixing effect in the low-carrier system cesb. *J. Phys. Soc. Jpn.*, 68(8):2498–2501, 1999.
- [42] A. Hannan, K. Iwasa, M. Kohgi, T. Osakabe, H. Kitazawa, and T. Suzuki. Exotic properties of cesb studied by x-ray diffraction. *J. Phys. Soc. Jpn.*, 73(7):1881–1887, Jul 2004.
- [43] K. Iwasa, A. Hannan, M. Kohgi, and T. Suzuki. Direct observation of the modulation of the 4f-electron orbital state by strong p-f mixing in cesb. *Phys. Rev. Lett.*, 88(20):207201, May 2002.
- [44] E. Prince, editor. *International Tables for Crystallography, Volume C: Mathematical, physical and chemical tables*. Springer Netherlands, 2004.